REPORT DOCUMENTATION PAGE

AFRL-SR-AR-TR-02-

0380

1. REPORT DATE (DD-MM-YYYY) 31/10/02	2. REPORT TYPE FINAL TECHNICAL	3. DATES COVERED (From - To) 9/96 - 12/31

4. TITLE AND SUBTITLE Prevention of Corrosion in Structural Aluminum Alloys	5a. CONTRACT NUMBER
	5b. GRANT NUMBER F49620-96-1-0475
	5c. PROGRAM ELEMENT NUMBER 61103D
6. AUTHOR(S) K. Sieradzki, R.W. Carpenter, R.C. Newman, N. Dimitrov, T.J.R. Leclere, M. Mukvirovic, N. Vasilovic· J. Erlebacher, M.J. Aziz	5d. PROJECT NUMBER 3484
	5e. TASK NUMBER RS
	5f. WORK UNIT NUMBER

7. PERFORMING ORGANIZATION NAME(S) AND ADDRESS(ES) Arizona State University Dept. of Mechanical and Aerospace Engineering Tempe, Arizona 85287-6106	8. PERFORMING ORGANIZATION REPORT NUMBER XAA 0020/TE

9. SPONSORING / MONITORING AGENCY NAME(S) AND ADDRESS(ES) AFOSR Lt.Col. Paul C. Trulove 4015 Wilson Blvd., Rm 713 Arlington, VA 22203-1954	10. SPONSOR/MONITOR'S ACRONYM(S) AFOSR
	11. SPONSOR/MONITOR'S REPORT NUMBER(S)

12. DISTRIBUTION / AVAILABILITY STATEMENT

Unlimited

13. SUPPLEMENTARY NOTES

14. ABSTRACT

We examined the general phenomenology associated with the corrosion of Al Alloy 2024-T3. Copper redistribution is controlled by S-phase dealloying and matrix dealloying. Matrix dealloying of aluminum occurs owing to the increased pH that develops at the alloy/electrolyte interface owing to oxygen reduction. We summarize results of a detailed investigation aimed at determining the mechanism and magnitude of the oxygen diffusion – limited current density during corrosion of Al Alloy 2024-T3. Our results show that oxygen reduction occurs via the standard 4-electron mechanism and that the oxygen diffusion – limited current density has a value of $\sim 25\ \mu A\ cm^{-2}$.

20021126 035

15. SUBJECT TERMS

16. SECURITY CLASSIFICATION OF:			17. LIMITATION OF ABSTRACT	18. NUMBER OF PAGES	19a. NAME OF RESPONSIBLE PERSON Karl Sieradzki
a. REPORT	b. ABSTRACT	c. THIS PAGE		4 with appendix	19b. TELEPHONE NUMBER (include area code) (480) 965-8990

Standard Form 298 (Rev. 8-98)
Prescribed by ANSI Std. Z39.18

Prevention of Corrosion in Structural Aluminum Alloys

FINAL MURI Report to the AFOSR, October 2002

K. Sieradzki*[1,2,3], R.W. Carpenter[1,2], R.C. Newman [4], N. Dimitrov[1], T.J.R. Leclere[4], M. Mukvirovic[3], N. Vasilovic[3], J. Erlebacher[5], M.J. Aziz[5]

[1]Dept. of Mechanical and Aerospace Engineering, [2]Center for Solid State Sciences, [3]Dept. of Materials Science and Engineering, Arizona State University, Tempe,AZ
[4]University of Manchester Institute of Science and Technology (UMIST)/Corrosion and Protection Centre,[5]Division of Applied Sciences, Harvard University

Principle Investigator and Information for correspondence
K. Sieradzki, Dept. of Mechanical and Aerospace Engineering, Arizona State University,
Tempe, AZ 85287-6106
Tel: 480-965-8990, Fax: 480-965-1384, email: Karl.Sieradzki@.asu.edu

1. Executive Summary

Herein we summarize the major results of the five-year MURI, "Prevention of Corrosion in Structural Aluminum Alloys." This program focused on examining mechanisms of copper redistribution during corrosion and protection of structural aluminum alloys such as 2024. Our major accomplishments are summarized in the bullets below.

- The development of a new electrochemical technique based on Pb underpotential deposition for the quantitative determination of copper redistribution during corrosion and coating pretreatments of copper containing aluminum alloys.

- The development of synthetic (model) 2024-T3 Al alloys that can be used to simulate the corrosion behavior of the real 2024-T3 alloy. Synthetic 2024-T3 is made using conventional lithography.

- The determination that our "synthetic Al 2024-T3" behaves as efficiently as a planar copper electrode for oxygen. Therefore, the synthetic alloy serves as an excellent model system for the cathodic reactions during corrosion of real 2024-TS.

- Characterization of the dealloying and corrosion behavior of the Al_2CuMg intermetallic S-phase which is the dominant second phase particle present in Al Alloy 2024-T3.

- The development of a new technique which uses the tip of a scanning tunneling microscope (STM) as a local pH probe at nanometer length scales. The purpose of this study was to determine the relative activity of the various particles on the surface of Al alloy 2024 for oxygen reduction. Our results indicated that the S-phase is

dominant with respect to controlling oxygen reduction on the surface of corroding Al 2024-T3.

- The development of a kinetic Monte Carlo code that simulates dealloying current-voltage behavior and morphology in any single-phase alloy system. This code was used to examine dealloying of copper in aluminum solid solution and dealloying of S-phase.

- Identification that during corrosion of Al Alloy 2024-T3, the S-phase is first anodic (i.e., it undergoes dealloying) and then turns in to an active cathode for oxygen reduction that supports corrosion.

- Determination of the diffusion - limited cathodic current density from oxygen reduction on the surface of Al alloy 2024 T-3 (20 μAcm^{-2}).

- Determination that our "synthetic Al 2024-T3" behaves as efficiently as a planar copper electrode for oxygen. Therefore, the synthetic alloy serves as an excellent model system for the cathodic reactions during corrosion of real 2024-TS.

- Results of Rotation Ring-Disk electrode experiments demonstrated the operation of a dissolution/back-plating copper redistribution mechanism during corrosion of Al 2024-T3. This process is triggered by very small copper particles of order tens of nanometers in size that become mechanically disconnected from de-alloyed S-phase intermetallic particles. As long as the remnant de-alloyed copper sponge stays mechanically and electrically connected to the substrate no copper dissolution can take place. In this case, we can disregard particle size effects on dissolution since the corrosion potential is almost 1 V less than the reversible potential of copper.

- Results of RRDE experiments demonstrated that the most significant source of redistributed copper during corrosion and pretreatment of Al alloy 2024 comes from *matrix dealloying*. This is in agreement with results of atomic – scale Kinetic Monte Carlo simulations. The other source of redistributed copper is mechanical disconnection of copper (from dealloyed S-phase) that dissolves under open circuit in the electrolyte and subsequently electrochemically deposits on the surface of Al alloy 2024.

- Realization that the low limiting net cathodic current density (~ 0.5 μAcm^{-2}) delivered by Al-Cu solid solutions is due to the superimposition of alkaline anodic dissolution on the cathodic oxygen reduction reaction, a subtle example of so-called "cathodic corrosion". The system is self-regulating in that the net current is just enough to poise the surface pH at the value where the open-circuit potential of the alloy is equal to the applied or naturally prevailing potential.

- Finally, the differences in behavior for the surface coverage of Cu between 2024-T3 and the synthetic 2024 alloy is attributed to the operation of a dissolution/back-plating mechanism triggered by mechanical disconnection of Cu particles from de-alloyed

porous S-phase. Comparisons of the behavior of these two alloys allow us to conclude that the matrix de-alloying and dissolution/back-plating contribute about equally to the copper redistribution process during corrosion of Aluminum Alloy 2024-T3 in 0.5 M NaCl.

2. Postdoctoral fellows and graduate students supported by this MURI

Dr. Nikolay Dimitrov, (post doc.)ASU
Natasia Vasilovic, Ph.D student, ASU
Misha B. Vukmirovic, Ph.D student, ASU
Ryan Paul Nunez , Masters Student ASU
Thomas J.R. Leclère, Ph.D student UMIST
Rodrick G. Ford (Masters Student)
Jake Mann (undergraduate student)

Two students obtained a Doctoral degree (Misha B. Vukmirovic, ASU, Thomas J.R. Leclère, Ph.D UMIST) and two students obtained a Masters degree (Rodrick G. Ford, Ryan Paul Nunez) based on work for this program

3. Publications (included as Appendix to this document)

[1] R.G. Ford, R.W. Carpenter, and K. Sieradzki, *Cu Nanoparticle Formation: Copper Redistribution During NaCl Solution Corrosion of Al-Cu-Mg Alloys*, Microscopy and Microanalysis, Vol. 4, Suppl. 2, 754 (1998).

[2] N. Dimitrov, J.A. Mann, and K. Sieradzki, *Copper Redistribution During Corrosion of Aluminum Alloys*, J. Electrochem. Soc., Vol. 146, pp. 98-102, (1999).

[3] N. Dimitrov, J.A. Mann, M. Vukmirovic, and K. Sieradzki, *Dealloying of Al₂CuMg in Alkaline Media*, Journal of the Electrochemical Society, Vol. 147, pp. 3283-3285 (2000).

[4] J. Erlebacher, M.J. Aziz, A. Karma, N. Dimitrov, and K. Sieradzki, *Evolution of Nanpoporosity in Dealloying*, Nature, Vol. 410, pp. 450-453 (2001).

[5] M.B. Vukmirovic, N. Dimitrov and K. Sieradzki, *De-alloying and Corrosion of Al Alloy 2024-T3*, J. Electrochemical Society, Vol. 149, pp. B428-B439 (2002).

[6] M.B. .Vukmirovic, N. Vasiljevic, N. Dimitrov and K. Sieradzki, *The Diffusion Limited Current Density of Oxygen Reduction on Copper*, J. Electrochemical Society in press, (August 2002).

[7] M.B. .Vukmirovic, *Dealloying and Corrosion of Al Alloy 2024-T3*, Ph.D Dissertation, October 2002, ASU available upon request.

[8] Thomas Leclère,*Redistribution and Self Regulation of the Cathodic Reaction Kinetics During Corrosion of AlCu Alloys.* May 2002 UMIST, ASU available upon request.

4. Invited Presentations

[1] K. Sieradzki, N. Dimitrov, J.A. Mann, and S.R. Brankovic, *Copper Redistribution During Corrosion of Al Alloys*, NACE'98, Research in Progress Symposium, San Diego, CA.

[2] K. Sieradzki, S.R. Brankovic, N. Dimitrov, and M. Vukmirovic, *Passivation of Elemental FCC Metal Surfaces*, 194th Meeting of The Electrochemical Society, A Symposium in Honor of the 70th Birthday of Jerome Kruger, 1998 Boston, MA

[3] K. Sieradzki, *Cu Redistribution During Corrosion of Al Alloy 2024*, NACE'99, Research in Progress Symposium, San Antonio, TX.

[4] K. Sieradzki, *Alloy Corrosion*, MRS Spring Meeting, San Francisco 2000.

[5] K. Sieradzki, *Alloy Corrosion*, MRS Spring Meeting, San Francisco 2000.

[6] K. Sieradzki, *Length Scales in Alloy Dissolution*, Spring Meeting of the Materials Research Society, San Francisco, CA, 2003.

5. Major Accomplishments

- Nature publication related to fundamental aspects of de-alloying.

- The result of this MURI investigation has been the identification of a new corrosion mechanism, i.e., matrix *de-alloying*. This type of process allows for renewal of cathodic sites during corrosion of not just Al alloys, but for all materials. We believe that this is the significant accomplishment of this 5-year study.

6. Honors, Awards, Patents

There have been no honors, awards or patents to date resulting from this work.

Microscopy AND
Microanalysis

PROCEEDINGS

MICROSCOPY AND MICROANALYSIS 1998

Microscopy Society of America
56th Annual Meeting

Microbeam Analysis Society
32nd Annual Meeting

ATLANTA, GEORGIA

July 12–16, 1998

Edited by
G.W. Bailey
K.B. Alexander
W.G. Jerome
M.G. Bond
J.J. McCarthy

Springer

1998

Cu NANOPARTICLE FORMATION: COPPER REDISTRIBUTION DURING NaCl SOLUTION CORROSION OF Al-Cu-Mg ALLOYS

R. G. Ford, R. W. Carpenter, & K. Sieradzki[†]

Science & Engineering of Materials Program, Center for Solid State Science, & [†]Mechanical & Aerospace Engineering Department, Arizona State University, Tempe, AZ 85287-1704

Aluminum-copper-magnesium alloys also containing manganese and iron (commercial designation 2024) are susceptible to marine corrosion and stress corrosion cracking. Susceptibility depends on heat treatment, and is thought to involve redistribution of copper from within the microstructure onto the surface of the corroding alloy, but few direct observations of the mechanism have been made. Copper can be distributed in several ways throughout the microstructure, which complicates mechanism studies. The primary age-hardening phase[1] is Al_2CuMg (orthorhombic; a=4.01, b=9.25, c=7.15 Å) which appears as more or less large equiaxed S particles at equilibrium, and as metastable S' plates[2] after aging for shorter times at lower temperature (~190°C). In addition, ubiquitous so-called "dispersoids" containing copper and manganese (prolate spheroid morphology) or iron (irregular "blocky" morphology) do not go into solution when the alloy is solid state homogenized (~495°C) and are always present in the microstructure. All of these phases are copper-rich sources for surface redistribution relative to the matrix during corrosion.

Marked Cu redistribution on the alloy surfaces did occur when it was exposed to simulated seawater at room temperature for short times. The redistribution was microstructure dependent. We used TEM & AEM methods to examine the surface of specimens (ion milled) after reaction with aqueous 0.5 M NaCl solution (simulated seawater). Fig. 1a shows part of a reaction zone formed in 5 sec in the solution at room temperature. The zone nucleated on the foil edge and moved to the left. The zone boundary is vertical in the figure. A similar zone in related material is shown in figure 2. The reaction front moved inward from the foil edge at ~2000Å/sec in both materials, at room temperature. The redistributed Cu in the aged material (Fig. 1) is a bimodal distribution of Cu-rich nanospheres on the specimen surface. The average diameter of the large nanospheres, attached to the edges of dispersoids and along the foil edge are 30 and 23 nm, respectively. The small nanosphere distribution is visible in Fig. 1b, and follows the morphology of the prior S' precipitate plates along <112> in the FCC matrix. The average size of the small component of the distribution is 17 nm. Fig. 2 shows one small reaction zone and part of a larger one at the edge of a large S phase grain in a special ingot[3] whose average composition was close to Al_2CuMg. In this case, the reaction zone itself is Cu rich nanospheres, with an additional distribution of nanospheres at the edge of the reaction zone. In both of these materials the nanospheres were crystalline. AEM methods showed the spheres to be Cu rich. Fig. 3 shows a homogenized (495°C for 24 hrs) and quenched 2024 alloy specimen after 30 second reaction with the salt solution at room temperature. This specimen contained Mn and Fe containing dispersoids but no S or S' phases. A much lower density of nanospheres is evident, and no reaction zones nucleated at the foil edge. The nanospheres are along the edges of the foil and near a Mn-containing dispersoid.

This data shows that both the reaction zones and the nanospheres are heterogeneously nucleated on the specimen surfaces. The formation reaction is remarkably fast for a room temperature reaction. It is apparent that the intermetallics containing Mg are more effective reaction participants than those containing Mn and/or Fe. There is not a strong relationship between the original sites of the Cu and the nanosphere distribution, thus the Cu has high mobility between reactant and product sites. Two possible paths for movement of the Cu are (1) surface diffusion on the specimen, and (2) solution into and re-precipitation from the salt solution. We will report on high resolution experiments to distinguish between these alternatives, and to elucidate the role of other chemical elements in this corrosion reaction.[4]

References

1. D.L. Robinson and M.S. Hunter, *Met. Trans.*, 3 (1972) 1147-1155.
2. L.K. Ives, et al., *Nat. Inst. Sci. Tech. report NBSIR* (1983) 83-2669.
3. Special alloy courtesy of Dr. R. Bucheit, Sandia Laboratories, Albuquerque.
4. This research is supported by the U.S. Air Force Office of Scientific Research, under contract F49620-96-1-0475.
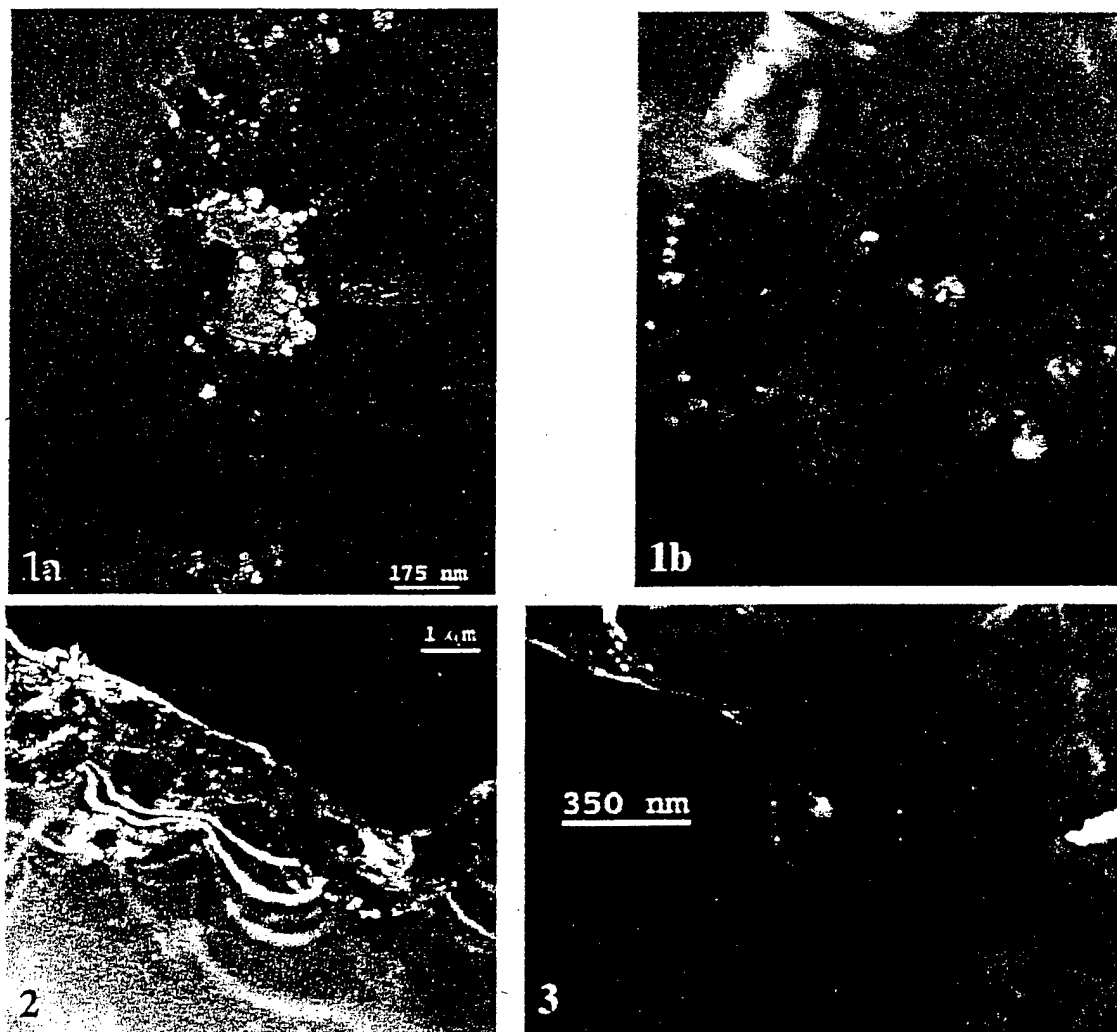
Fig 1. A reaction zone formed on homogenized and aged (20 hrs @ 190°C) for S' in 2024 alloy. (a) Reaction zone and edge of foil to the right. Fe-containing dispersoid marked A and Mn-containing dispersoid marked B, both inside the reaction zone. (b) Higher magnification image of the boxed area showing smaller nanospheres following <112> matrix orientation of original S' morphology, at 100 keV.

Fig 2. Reaction zone at edge of S crystal foil after 5 seconds in 0.5 M NaCl aqueous solution, at 100 keV.

Fig 3. Cu-rich nanosphere distribution on the surface of a homogenized and quenched (24 hrs @ 495°C) 2024 alloy specimen after 30 sec in 0.5 M NaCl$_{(aq)}$ solution, imaged at 200 keV.

Copper Redistribution during Corrosion of Aluminum Alloys

N. Dimitrov, J. A. Mann, and K. Sieradzki*

Department of Mechanical and Aerospace Engineering and Science of Engineering Materials Program, Arizona State University, Tempe, Arizona 85287-6106, USA

We describe a new quantitative electrochemical technique for measuring the copper redistribution that occurs during corrosion and pretreatment of high-strength copper-containing aluminum alloys. Underpotential deposition (upd) of Pb on Cu was used to assay the surface coverage of Cu. Model experiments using samples of known Al-Cu ratios were used to evaluate the accuracy of the technique and develop a calibration curve. The results demonstrated the accuracy of the method to within 2%. The elemental copper remaining on the surface of Al 2024-T3 samples after various pretreatment/corrosion procedures was determined using the upd technique. A simple treatment involving open-circuit etching of the alloy surface in 3 M HNO_3 was found to be most efficient for the removal of Cu from the Al alloy surface. In accord with a recent observation of Bucheit et al.,[1] convection was found to enhance copper redistribution on an Al 2024-T3 sample in 0.5 M NaCl solution.

© 1999 The Electrochemical Society. S0013-4651(98)04-027-0. All rights reserved.

High strength is achieved in aluminum aircraft alloys by the presence of Cu as an alloying element. However, copper is particularly deleterious to the corrosion behavior of Al alloys owing to galvanic couples set up between copper-rich intermetallic inclusions and the adjacent copper-depleted matrix. This makes copper-containing Al alloys the most difficult to protect with conversion coatings. Owing primarily to these arguments, it has proven particularly difficult to identify a suitable environmentally acceptable replacement for chromium-containing conversion coatings for the aluminum alloy 2024-T3. The corrosion of this alloy is thought to be enhanced by the cathodic activity of intermetallic particles.[2-5] These particles serve as preferential sites for the reduction of oxygen, since the conductivity of the mixed oxide film covering them is higher than that of the passive film on elemental aluminum. A key issue in the coating and corrosion protection of Al-Cu-Mg alloys is the redistribution of copper that occurs during pretreatment and subsequent corrosion. A significant accumulation of copper on the alloy surface was already shown after mechanical polishing of Al 2024-T3 in aqueous diamond suspension[6] and after chemical polishing in a mixture of concentrated sulfuric, phosphoric, and nitric acids.[7]

Enrichment of copper on the alloy surface is believed to result from dealloying of intermetallic particles, in particular S-phase particles (Al_2CuMg) which account for ~60% of the particle population on the alloy surface. The dealloying process results in nanoporous Cu-rich remnants that induce pitting around their periphery.

The most common approach for examining copper redistribution on the surface of a high strength Al-Cu-Mg alloys would be to use ultrahigh vacuum surface techniques such as Rutherford backscattering[7,8] or Auger electron spectroscopy (AES).[9,10] However, the copper which redistributes assumes several morphologies which are not particularly suited to conventional surface analysis approaches. Dealloying produces nanoporous Cu structures and most of this area is inaccessible to standard surface analysis. AES would sense the projected area of the porous Cu but would give no hint regarding the true physical area comprising the pore structure. It is the physical area taken up by the elemental Cu that we would like to measure, since this determines the cathode area available for oxygen reduction. Additionally, redistributed monolayer (ML) levels of Cu will likely oxidize during transport to a vacuum system unless heroic measures are employed. These arguments suggest that an electrochemical technique, sensitive to the same physical area of elemental Cu that dissolved oxygen would see, would be the preferred method of assaying the Cu surface coverage. Such a technique could be based upon an electrochemical reaction which is sensitive to copper but not to the aluminum or other constituents of the alloy.

An appropriate reaction for this purpose is Pb underpotential deposition on copper resulting in the formation of one monolayer of Pb adatoms on the Cu surface. Pb upd on Cu was investigated on Cu polycrystalline electrodes[11] and on monocrystalline Cu (111)[12-16] and Cu (001)[17] faces. It has been shown that Pb forms one epitaxial monolayer on the copper surface[16,17] regardless of the substrate crystallographic orientation. Twin-electrode thin layer voltammetry suggests an ideal charge stoichiometry, i.e., $Z = 2$ for the system Pb^{2+}/Cu (111), ClO_4^-.[13] Charge densities in the range of 300-335 $\mu C\ cm^{-2}$ were reported for the Pb upd ML formed on the Cu (111) electrode[13,16,18] and a charge density of 260 $\mu C\ cm^{-2}$ for the one formed on the Cu (001) electrode.[17] The kinetics of the Pb underpotential deposition on Cu (111) were found to depend strongly on the presence of a removable oxygen species on the substrate surface.[13,15] A pronounced irreversibility of the process in a solution containing ClO_4^- was reported.[16] The difference in the potentials of the adsorption and stripping peak, ~150 mV, was attributed to adsorption/desorption of oxygen-containing species.[16] Even traces of Cl^-, CH_3COO^-, and other specifically adsorbed ions were found to reduce the peak potential difference and to enhance the voltammetric peak shape.[12,15,16] The significant influence of the specifically adsorbed ions on the upd process kinetics is related mainly to a competition between those anions and the oxygen species originally existing on the copper surface. A nucleation-like behavior in terms of a "negative 2D nucleation and growth process" within a preformed surface layer consisting of specifically adsorbed ions or oxygen-containing species was suggested for the electrochemical system considered.[15]

Experimental

We used a model Al-Cu system to access the quality of a quantitative assay of Cu based on the charge associated with the Pb upd process. Strips of commercially pure polycrystalline Al were used along with strips of commercially pure polycrystalline Cu as a working electrode in the experiment. Two samples were prepared, each with 1 cm^2 Al and 1 cm^2 Cu exposed. The area exposed was polished with Buehler Carbimet paper to 15 μm. On the first sample the exposed Al was gradually masked, 0.25 cm^2 at a time, with nail polish so that results could be obtained for percentages of Cu between 50 and 100%. On the other sample the exposed Cu was masked in the same way, giving results between 50 and 0% Cu. The nail polish was stable and showed no signs of decomposition in the electrolytes used over the time spans relevant to these experiments. The samples were treated for 15 min in H_2O_2 and dipped for 10 s in 1 M HNO_3. A lead wire etched prior to the experiment in dilute nitric acid was used as a reference electrode. A platinum wire coil (area of 3 cm^2), hydrogen flame annealed prior the experiment, served as a counter electrode. The solution used for this electrochemical work consisted of 10^{-1} M $NaClO_4$ + 10^{-3} M $Pb(ClO_4)_2$ + 10^{-4} M $HClO_4$ + 10^{-3}

M CH₃COONa. All the solutions were made with high purity grade chemicals and >18 MΩ Nanopure water. A BAS CV-27 model potentiostat was used for the experiment and a Nicolet 310 digital oscilloscope was used to store data. In each experiment, the potential was swept from -20 to 300 mV (Pb/Pb^{2+}) at a sweep rate of 20mV s^{-1}. All potentials are reported vs. the Pb/Pb^{2+} pseudo-reference electrode unless otherwise specified.

The applicability of our electrochemical technique for measuring copper redistribution was examined in three different experiments. The first of these involved a cleaning and pretreatment procedure for Al 2024-T3. The Cu coverage was determined after each step of this procedure which included treatments in 0.1 M NaOH, 0.5 M HNO₃ + 0.65 M NaNO₃, 3 M HNO₃, and 0.1 M (NH₄)₂SO₄ + 0.03 M NH₄OH. After each treatment the sample was washed with 18 MΩ Nanopure water and transferred to the three-electrode cell for elemental Cu coverage determination. In the second experiment, we examined the change in the amount of copper on the surface of an Al 2024-T3 sample as a function of time during immersion in 0.1 M NaOH solution. In the third experiment, we examined the change in the amount of copper on the surface of an Al 2024-T3 sample as a function of time during immersion in stagnant and stirred 0.5 M NaCl solutions.

Results and Discussion

Model experiment.—The model experiment described above was designed to determine the dependence of the associated Pb upd charge on the area of Cu in an Al-Cu sample. A relatively high electrolyte pH (pH 4) was chosen in order to suppress the hydrogen evolution reaction, that might be expected to occur in a high strength alloy, with a negligible overpotential. The millimolar amount of CH₃COO⁻ present in the solution was expected to reduce the irreversibility of the upd process and enhance the current peaks associated with the Pb upd process.[15,16]

Figure 1 shows the current-voltage behavior of a polycrystalline copper electrode in solutions with (solid line) and without (dashed line) lead ions. The peak position (100 mV vs. Pb/Pb^{2+}) of the adsorption wave was close to that (105 mV) obtained by Schmidt et al.[11] for the system Cu (polycrystalline)/ Pb^{2+} in the presence of 0.5 M KCl. The charge associated with the Pb upd layer was found to be 280 ± 10 μC cm^{-2}, about 65% of the one determined by Schmidt and Gygax.[11] This difference may be related to the coulombic contribution of Cl⁻ ion adsorption on the copper surface, estimated to be 20-25% of the overall charge in the systems Cu (111)/

Pb^{2+}, 10^{-4} Cl⁻ [16] and Cu (001)/Pb^{2+}, 10^{-4} Cl⁻.[17] These papers reported net charges of 300 and 262 μC cm^{-2} for this system.

Figure 2 shows the current-voltage behavior of Al-Cu samples containing different area fractions of Cu exposed in a solution containing Pb ions. These voltammograms were obtained using the following background subtraction procedure. A polynomial form was fit to the dashed line (blank run containing no Pb ions) in Fig. 1 and this was subtracted from the solid curve of Fig. 1 yielding the Cu-100% wave shown in Fig. 2. The other curves shown in Fig. 2 were obtained by numerically fitting the coefficients of the polynomial such that a separate "dotted line "or "blank run" for each sample was generated that smoothly interpolated across the upd wave. These numerically generated blank runs have the advantage that a background subtraction can be accomplished without an a priori knowledge of the area fraction of the composite sample covered by copper. The results shown in Fig. 2 demonstrate that the peak height and area of the upd wave depend strongly on the area fraction of Cu exposed; the larger the area of Cu exposed the higher the amount of underpotentially deposited lead.

Figure 3 is a normalized data collapse of the upd waves in Fig. 2 showing that the wave shape and position is only very weakly dependent on the Cu content of the model Al-Cu sample. These composite electrodes were polycrystalline in nature. For the samples in the range of 50-100% area fraction Cu, the upd lead sampled the identical area of polycrystalline Cu, and within this composition range there was no shift in the upd peak position. For samples in the range of 0-50% Cu, the Cu portion of the composite surface was masked. Even so, we observed no significant (< ~3 mV) shift in the peak position up to the sample containing 33% Cu. There was a shift, ~10 mV, for the samples containing 20 and 11% area fraction Cu. The polycrystalline Cu used in the background subtraction calibration procedure had a grain size of order 200 μm, so the 11% Cu sample (that had an absolute Cu area of 0.11 cm²) contained only about 100 grains. The shift in the adsorption peak resulted from the upd process sampling a smaller number of grains for the samples containing less than ~30% area fraction Cu.

The final result extracted from the model experiment is presented in Fig. 4 which shows the normalized charges corresponding to the Pb underpotential wave as a function of the fractional area of Cu exposed. The best fit to the data (correlation coefficient = 0.998) is a straight line with a slope of 1. Comparison of the area fraction of Cu predicted by the linear fit to the actual values of the known standards, showed that the amount of Cu exposed on the surface could be determined to an accuracy of ca. 2%.
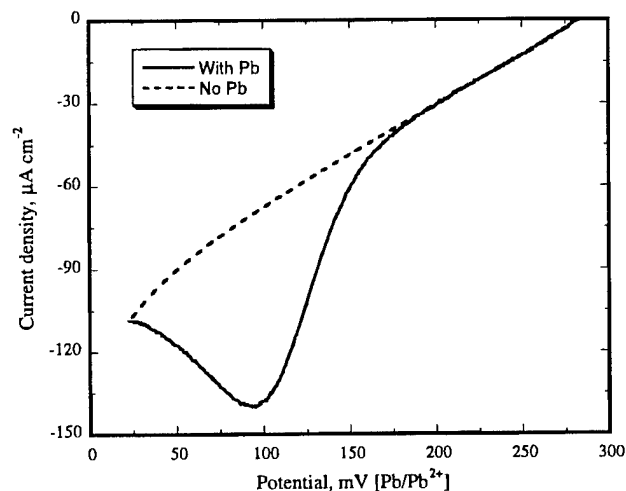

Figure 1. Current-voltage behavior (cathodic sweep) of a Cu polycrystalline electrode in 10^{-1} M NaClO₄ + 10^{-3} M Pb(ClO₄)₂ + 10^{-4} M HClO₄ + 10^{-3} M CH₃COONa solutions with and without 10^{-3} M Pb(ClO₄)₂. Sweep rate 20 mV s^{-1}.

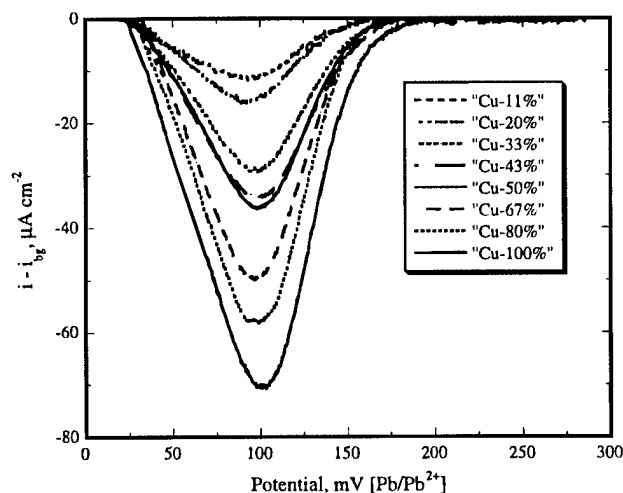**Figure 2.** Current-voltage behavior of Al-Cu samples containing different area fractions of Cu exposed in 10^{-1} M NaClO₄ + 10^{-3} M Pb(ClO₄)₂ + 10^{-4} M HClO₄ + 10^{-3} M CH₃COONa. Sweep rate -20 mV s^{-1}.
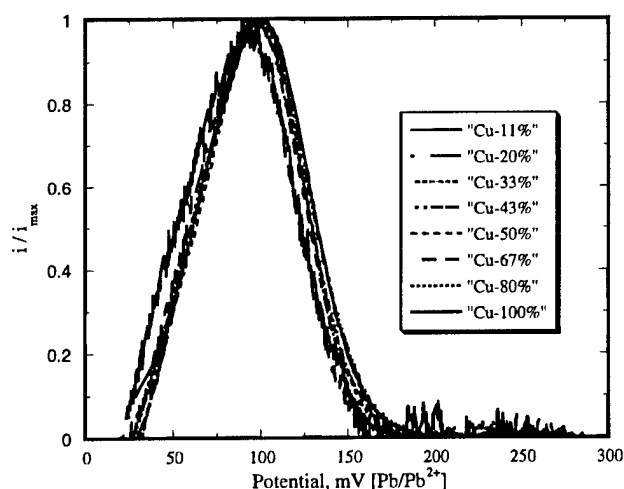
Figure 3. Normalized voltammetric curves for samples with different Al-Cu ratio in a solution containing 10^{-1} M $NaClO_4$ + 10^{-3} M $Pb(ClO_4)_2$ + 10^{-4} M $HClO_4$ + 10^{-3} CH_3COONa. Sweep rate -20 mV s^{-1}.

Figure 5. Corrected voltammetric curves obtained on Al 2024-T3 samples after treatment in different solutions (see text). Sweep rate -20 mV s^{-1}.

Pretreatment procedure for Al 2024-T3.—We examined the amount of copper remaining on the surface after each of four pretreatment steps. The initial step was treatment of an aluminum alloy 2024-T3 sample in 0.1 M NaOH solution at open-circuit potential for 1 min. This was expected to dissolve the gross oxides that may have formed on the alloy sheet surface during processing. Additionally this treatment should selectively leach Al from S-phase particles on the alloy surface. The polarizing step of the "copper removal" procedure proposed in Ref. 19 was used. The sample was treated accordingly in 0.5 M HNO_3 + 0.65 M $NaNO_3$ at a potential of -50 mV (SCE) for 40 min. The third step was a simple etching in 3 M HNO_3 for 2 min at open-circuit potential, designed for the removal of any residual copper remaining on the surface. Finally, a procedure found to significantly reduce the cathodic activity of the alloy surface[20] was applied. The sample was treated in a solution containing 0.1 M $(NH_4)_2SO_4$ + 0.03 M NH_3 (pH 8) at potentials -600 mV (SCE) and 150 mV (SCE) in order to clean the surface from all components that are expected to increase the surface cathodic activity, i.e., Cu, Fe, Mn. The results of this procedure are summarized in Fig. 5 where corrected voltammograms for all samples examined are presented. The first curve presented is for lead upd on an untreated Al 2024 sample. After a treatment in a NaOH solution, a significant amount of Al had been selectively dissolved
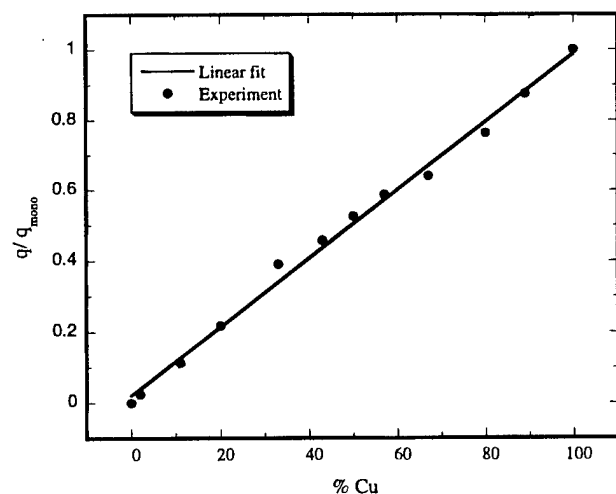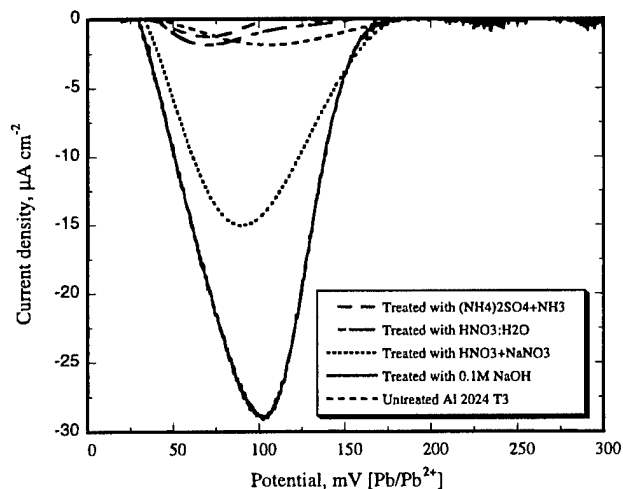
from the surface, resulting in a dramatic enrichment of elemental Cu on the alloy surface. The Pb upd result suggested that even after performing the copper removal procedure described in Ref. 19, there was still a significant amount of Cu remaining on the surface (Treated with HNO_3 + $NaNO_3$). The most efficient treatment for copper removal appeared to be etching in 3 M HNO_3 for 2 min at open-circuit potential. As a result of this treatment the residual copper on the surface (treated with HNO_3:H_2O) dropped below the originally existing level (Untreated Al 2024 T3). The final treatment did not show a significant decrease in the current signal coming from Pb upd [$(NH_4)_2SO_4$ + NH_3].

Dealloying in NaOH solution.—Another illustration of the lead upd technique was performed examining the elemental copper content of an Al 2024 T3 surface after treatment in 0.1 M NaOH at open-circuit potential for various times. The charge associated with the underpotentially deposited Pb layer after each treatment is plotted in Fig. 6. The results demonstrate that there is a dramatic increase of the elemental Cu on the alloy surface with increasing time. This is simply a result of progressive dealloying of Cu-containing intermetallics on the alloy surface. After the fifth minute of the experiment the charge exceeded a full monolayer level, implying that a significant "roughening" of a portion of the alloy surface

Figure 4. Normalized charges corresponding to the Pb underpotential wave as a function of the fractional area of Cu exposed.
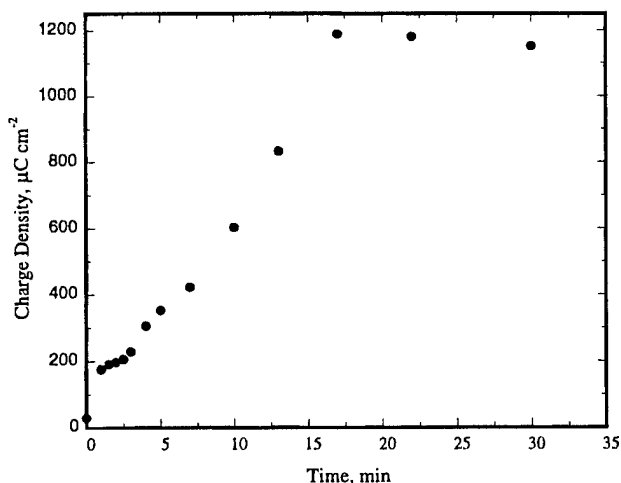

Figure 6. Charge density of Pb upd layer formed on an Al 2024-T3 sample after treatment in 0.1 M NaOH solution for different times.
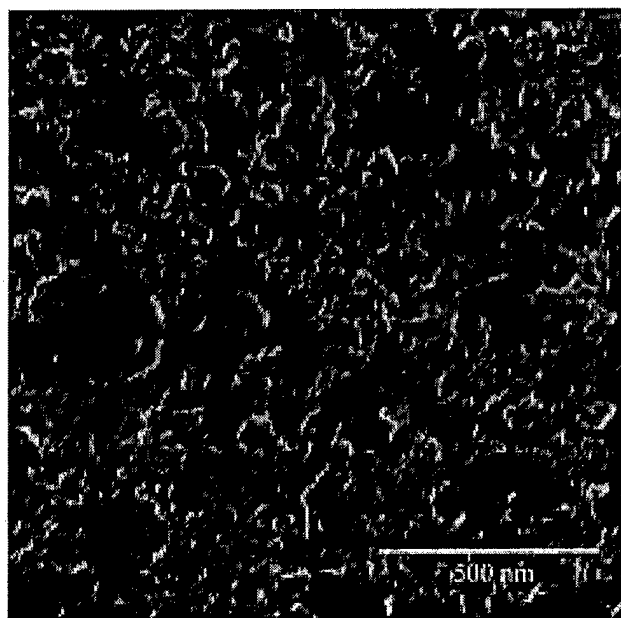
Figure 7. High-resolution scanning electron micrograph showing the morphology of the S-phase sample after polarization at 50 mV (SCE) in 0.1 M NaOH + AlO_2^- solution.

occurred simultaneously with the copper enrichment process. This type of roughening is known to occur in alloy systems undergoing a dealloying process. During dealloying, the less noble component(s) of the alloy is selectively dissolved while the more noble element develops a bicontinuous solid-void morphology with a very large surface to volume ratio.[21-23] We have recently shown that S-phase (Al_2MgCu) intermetallic undergoes selective dissolution in NaOH and neutral chlorides resulting in a bicontinuous copper-void morphology.[24] A representative example for such a morpholgy is shown in Fig. 7. This high surface to volume area structure results in an elemental Cu surface coverage which can significantly exceed that of a single equivalent monolayer. Figure 6 shows that after 15 min of exposure there is a decrease in the charge of the Pb upd layer. We believe that this behavior is a result of ambient temperature coarsening of the dealloyed morphology.[22]

Pitting in NaCl solution.—Using a procedure similar to that described above for NaOH, we examined Cu redistribution on the surface of Al 2024-T3 exposed to 0.5 M NaCl solution at open-circuit potential for different times. It is well known that Al 2024-T3 samples undergo pitting and intergranular corrosion[25,26] in a neutral chloride solution, and it was recently shown that that corrosion of this alloy in acid chloride results in a fourfold increase of the copper content on the surface of this alloy.[27] We believe that this enrichment in copper probably results from the selective dissolution of S-phase intermetallics. Additionally, if some of the nanometer-sized ligaments of copper become mechanically disconnected from the bicontinuous dealloyed structure, these copper ligaments will dissolve at open circuit in the neutral chloride solution. The resulting copper cations will then plate back onto the alloy surface. Another explanation of the copper redistribution process associated with of Al 2024-T3 in a neutral NaCl solution was presented by Buchheit et al.[1] They suggested that small copper or copper-enriched remnants from the dealloying process mechanically detach from the surface and are mechanically dispersed and deposited onto the alloy surface by a non-Faradaic process, possibly involving convection. In our experiment, we sought to determine the effect of convection on the copper redistribution process. Figure 8 shows results for copper redistribution obtained after treatments in stagnant and stirred (500 rpm) solutions. These results demonstrate that in these experiments convection in the electrolyte increased the quantity of elemental copper on
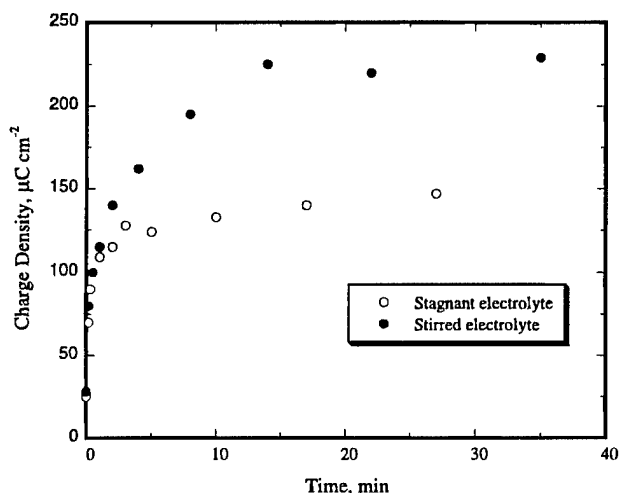

Figure 8. Charge density of Pb upd layer formed on an Al 2024-T3 sample after treament in 0.5 M NaCl solution for different times.

the surface of the alloy by a factor of about 1.8. The results discussed herein undoubtedly confirm the conjecture[1] that convection enhances the copper redistribution process. However, at present the precise mechanism of the enhanced redistribution associated with convection is unclear.

Summary

A new surface-sensitive technique for determining the elemental copper coverage on the surface of Al alloys based on a upd process has been described. Model experiments on Al-Cu samples of known composition demonstrated a linear dependence between the charge density associated with an underpotentially deposited Pb layer and the area fraction of Cu in the model system. An examination of different steps of a pretreatment procedures performed on Al 2024-T3 samples using this technique demonstrated that simple open-circuit etching of this alloy in 3 M HNO_3 to be most effective with respect to copper removal from the surface. Very significant enrichment of elemental Cu occurred when Al 2024 T-3 surfaces were exposed to 0.1 M NaOH solution or 0.5 M NaCl solution. Convection in the electrolyte was found to significantly enhance the Cu redistribution process.

Acknowledgments

References

1. R. G. Buchheit, R. P. Grant, P. F. Hlava, B. Mckenzie, and G. L. Zander, *J. Electrochem. Soc.*, **144**, 2621 (1997).
2. *Air Force Blue Ribbon Advisory Panel on Aircraft Coatings*, Part 1, *Basic Research*, Prepared for Materials Directorate, Wright Laboratory, Aeronautical Systems Center, Air Force Materials Command, Wright-Patterson AFB, OH (1995).
3. D. R. Baer and J. Janata, *Science and Technology Master Plan for Chromate Replacement*, Prepared for materials Directorate, Wrigth Laboratory, Aeronautical systems Center, Air Force Material Command, Wright-Patterson AFB, OH (1995).
4. R. Buchheit, in *Air Force Blue Ribbon Advisory Panel on Aircraft Coatings*, Part 1, *Basic Research*, Prepared for Materials Directorate, Wright Laboratory, Aeronautical Systems Center, Air Force Materials Command, Wright-Patterson AFB, OH (1995).
5. R. G. Buchheit, *J. Electrochem. Soc.*, **142**, 3994 (1995).
6. P. L. Hagans and C. M. Haas, *Surf. Interface Anal.*, **21**, 65 (1994).
7. H. Habazaki, K. Shimizu, M. A. Paez, P. Skeldon, G. E. Thompson, G. C. Wood, and X. Xhou, *Surf. Interface Anal.*, **23**, 892 (1995).
8. H. H. Strehblow, C. M. Melliar-Smith, and W. M. Augustyniak, *J. Electrochem. Soc.*, **125**, 915 (1978).
9. D. Y. Jung, I. Dumler, and M. Metzger, *J. Electrochem. Soc.*, **132**, 2308 (1985).
10. *A Guide to Materials Characterization and Chemical Analysis*, John P. Sibilia, Editor, p. 235, VCH Publishers, Inc., New York (1996).
11. E. Schmidt and H. R. Gygax, *J. Electroanal. Chem.*, **12**, 300 (1966).
12. A. Bewick, J. Jovicevic, and B. Thomas, *Faraday Symp. Chem. Soc.*, **12**, 24 (1978).
13. H. Siegenthaler and K. Juttner, *J Electroanal. Chem.*, **163**, 327 (1984).

14. J. C. Farmer and R. H. Muller, *J. Electrochem. Soc.,* **132**, 39 (1985).
15. J. R. Vilche and K. Juttner, *Electrochim. Acta,* **32**, 1567 (1987).
16. G. M. Brisard, E. Zenati, H. A. Gasteiger, N. M. Markovic, and P. N. Ross, Jr., *Langmuir,* **11**, 2221 (1995).
17. G. M. Brisard, E. Zenati, H. A. Gasteiger, N. M. Markovic, and P. N. Ross, Jr., *Langmuir,* **13**, 2390 (1997).
18. G. L. Borges, M. G. Samant, and K. Ashley, *J Electrochem. Soc.,* **139**, 1565 (1992).
19. F. Mansfeld and Y. Wang, in *Oxide Films on Metals and Alloys,* K. R. Hebert and G. E. Thompson, Editors, PV 94-25, p. 200, The Electrochemical Society Proceedings Series, Pennington, NJ (1995).
20. A. J. Davenport and R. C. Newman, Unpublished results.

21. K. Sieradzki and R. C. Newman, *J. Phys. Chem. Solids,* **48**, 1101 (1987).
22. R. Li and K. Sieradzki, *Phys. Rev. Lett.,* **68**, 1168 (1992).
23. K. Sieradzki, R. R. Corderman, K. Shukla, and R. C. Newman, *Philos. Mag.,* **59**, 713 (1989).
24. N. Dimitrov, J. A. Mann, M. Vukmirovic, and K. Sieradzki, To be published.
25. T. J. Warner, M. P. Schmidt, F. Sommer, and D. Bellot, *Z. Metallkd.,* **86**, 494 (1995).
26. G. L. Scheider, N. N. Cherkasov, V. I. Smolentzev, B. E. Popov, and A. P. Kovtun, *Mater. Sci. Heat. Treat.,* **26**, 632 (1985).
27. K. Koval, J. DeLuccia, J. Y. Josefowicz, C. Larid, and G. C. Farrington, *J. Electrochem. Soc.,* **143**, 2471 (1996).

Dealloying of Al₂CuMg in Alkaline Media

N. Dimitrov, J. A. Mann, M. Vukmirovic, and K. Sieradzki*,z

Department of Mechanical and Aerospace Engineering and Science of Engineering Materials Program, Arizona State University, Tempe, Arizona 85287-6106, USA

The anodic behavior of Al₂CuMg (S-phase) samples in 0.1 M NaOH solution was investigated. Critical potential behavior typical of dealloying was observed while sweeping the potential from open circuit in the anodic direction. Theoretical estimates based on curvature effects in alloy dissolution suggested the development of a porous structure with 2 nm average ligament size during the initial stages of the dealloying process. A delicate balance between metal dissolution, ion solubility, and mass transport in the electrolyte appears to govern the kinetics of the "pit" growth process. A bicontinuous dealloyed microstructure containing flatter regions showing "Swiss cheese"-like morphology was observed as a result of long-term dealloying.
© 2000 The Electrochemical Society. S0013-4651(99)02-076-5. All rights reserved.

The understanding of the corrosion of high-strength aluminum alloy 2024 is strongly connected with the cathodic activity of intermetallic particles.[1-3] These sites on the alloy surface are preferential to the Al matrix for oxygen reduction. It is well known that the majority of the intermetallic particles in this alloy is composed of S phase (Al₂CuMg) accounting for 60% of the particle population on the alloy surface.[4] A thorough understanding of S-phase anodic behavior is crucial to developing a detailed understanding of corrosion in this important class of Al alloys.

In the initial stage of Al alloy 2024 corrosion in a neutral chloride solution, the S-phase particles are attacked preferentially with respect to the matrix. Mg and Al are selectively dissolved from the S phase leaving a Cu-rich surface remnant. At this stage, the S-phase particle behaves as a cathode for oxygen reduction, and the matrix surrounding the particle serves as an anode. Oxygen reduction at the particle results in a local pH increase allowing the surrounding Al matrix to dissolve as the soluble AlO₂⁻ anion. The increased pH also serves to allow for continued dissolution and dealloying of the Al₂CuMg phase below the Cu-rich surface layer.

A simple way to think about the S-phase corrosion process is to compare it to the selective dissolution of a binary alloy of composition AₚB₁₋ₚ, where A is the less noble (more electroactive) component and p is greater than the dealloying threshold.[5-7] A characteristic parameter for such a system is its critical potential E_c. Bulk dealloying leading to a bicontinuous solid-void corrosion morphology, is expected to be visible at potentials above E_c.[6,7] The binary alloy is relatively inert with respect to the dealloying process at potentials below E_c, where processes such as surface diffusion of the more-noble component limit the current density. For binary noble metal alloys the current density at potentials below E_c was found to be ~1 μA/cm².[7]

The S phase is known to contain 50 atom % Al, 25 atom % Mg, and 25 atom % Cu. A quick check of the equilibrium metal/metal ion reversible potentials shows that the reversible potentials of Mg and Al, while relatively close to each other, are ~2 V more negative than that of copper. Nevertheless since Mg is not soluble in a pH ≅ 13 electrolyte, we consider Al as constituent A and Cu + Mg as constituent B. Since p = 0.5 one would expect to see critical potential behavior of the S phase examined under properly chosen experimental conditions.

The aim of the present work is to investigate the anodic behavior of the S phase in a NaOH solution at pH 13 and to examine the morphology of the surface after corrosion at potentials above and below the critical potential.

Experimental

The S-phase samples used were 2 mm thick disks cut from an Al-Cu-Mg ingot prepared at Sandia National Laboratories. The slices were mechanically polished with Fibrmet® pads down to 0.3 μm. For electrochemical work, millimeter-sized S phase particles (Al₂CuMg)

were isolated and masked off with nail polish. The slices used for scanning electron microscopy (SEM) examination were left unmasked to prevent charging of the sample.

Nominally pure aluminum samples were cut from a 99.99% sheet. For electrochemical work, millimeter-sized spots were masked off so that comparison to similarly treated S-phase samples would be possible. A pure copper wire was mechanically polished, etched in nitric acid, and masked (leaving 1 mm² unmasked) for electrochemical examination.

All glassware used for experimentation and the preparation of electrolytes was cleaned with concentrated HNO₃ and H₂SO₄ at 70°C, then rinsed using doubly distilled and Barnstead Nanopure (18.3 MΩ) water. The electrolyte used for electrochemical work consisted of 10⁻¹ M NaOH (Alfa ÆSAR 99.996%) + 10⁻³ M Al₂(SO₄)₃, and was prepared with Nanopure (18.3 MΩ) water. This electrolyte was chosen since it is widely used in many cleaning and pretreatment procedures for high strength aluminum alloys.

Potentiodynamic polarization tests were performed using a Bioanalytical Systems CV-27 potentiostat, starting at open-circuit potential (OCP) and sweeping in the positive direction at a scan rate of 2 mV/s. All experiments were conducted in an open cell at ambient conditions. An oxidized silver wire (270 + 40 mV *vs.* normal hydrogen electrode) was used as a pseudo-reference electrode (PRE), along with a platinum wire as a counter electrode. All potentials reported are with respect to the oxidized silver wire.

The same electrolyte and cell were used to prepare dealloyed S-phase samples for SEM examination. Samples were subjected to potentials of −800 and −200 mV for 20 h. These potentials were chosen based upon our voltammetry results as discussed below. High-magnification SEM examination was performed with a Hitachi S-4500 field emission scanning electron microscope at an accelerating voltage of 15 keV.

Results and Discussion

Electrochemistry.—Figure 1 shows representative polarization curves for pure aluminum, masked S phase, and pure copper samples in 10⁻¹ M NaOH + 10⁻¹ [M Al₂(SO₄)₃] electrolyte. The curve for pure aluminum shows a sharp increase in current during a positive sweep from the OCP of ~ −1.4 V. The shape of the curve at high overvoltages is indicative of a diffusion-limited dissolution process. This behavior results from exceeding the solubility limit of the AlO₂⁻ anion at the solid/electrolyte interface. We analyzed the current-voltage data by fitting it according to, $\eta = const \cdot log(I - i/i_d)$, where η is the overvoltage and i_d is the diffusion-limited current density, defined by $(DnF\Delta C)/\delta$. Here D is the diffusivity of the AlO₂⁻ anion, n is the number of electrons transferred, F is the Faraday constant, and δ is the diffusion boundary layer thickness. The result of the analysis is shown as Fig. 2. The fitting procedure yielded a value of i_d = 8 mA cm⁻². The concentration difference $\Delta C = C_0 - C_\infty$ (where C_0 is the concentration at the electrode surface and C_∞ is the concentration in

* Electrochemical Society Active Member.
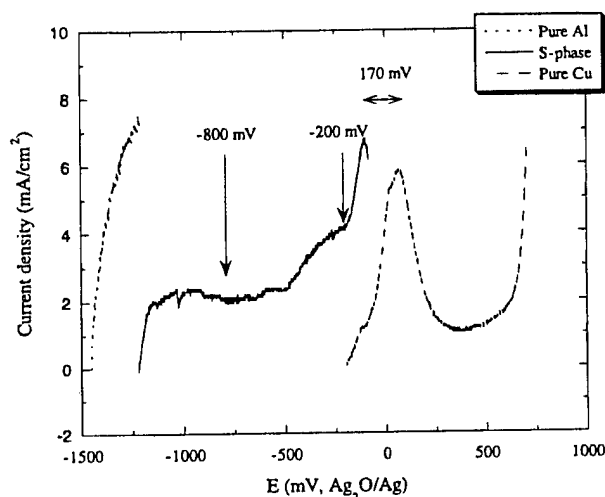z E-mail: karl@icarus.eas.asu.edu

Figure 1. Current-voltage behavior of Al, S phase, and Cu in 0.1 M NaOH + 10^{-3} M AlO_2^- solution. Sweep rate -2 mV/s.

the bulk of electrolyte) was estimated assuming $D \sim 10^{-5}$ cm^2/s^{-1},[8] $\delta \sim 5 \times 10^{-2}$ cm,[9] $n = 3$, and $F = 96,500$ C mol^{-1}, to be 0.13 M dm^{-3}. This value is in agreement with ancillary work that showed the solubility of $NaAlO_2$ in a 0.1 M NaOH + 10^{-3} M $Al_2(SO_4)_3$ electrolyte does not exceed 0.2 M dm^{-3}.

The polarization behavior of pure copper (Fig. 1) also shows an increase from a corrosion potential of ~-200 to ~100 mV. At a potential of ~100 mV we observed passivation-like behavior, followed by another increasing current region. The current voltage behavior is in general agreement with previously reported work of Strehblow and co-workers.[10] For our experimental conditions (pH 13) this current wave can be attributed to CuO formation according to the reaction[10,11]

$$\frac{1}{2}Cu_2O + \frac{1}{2}H_2O = CuO + H^+ + e^- \qquad [1]$$
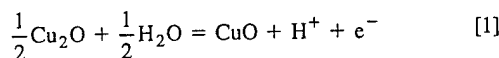
The S-phase sample yields a dissolution curve with intermediate features of elemental Al and Cu. The open-circuit potential, ~ -1.2 V, lies between that of aluminum and copper. From potentials of ~ -1 to -0.5 V, the current is almost potential independent. In this precritical region, the alloy behaves as if it were "passive," albeit with a relatively high current density. Figure 1 shows the critical potential
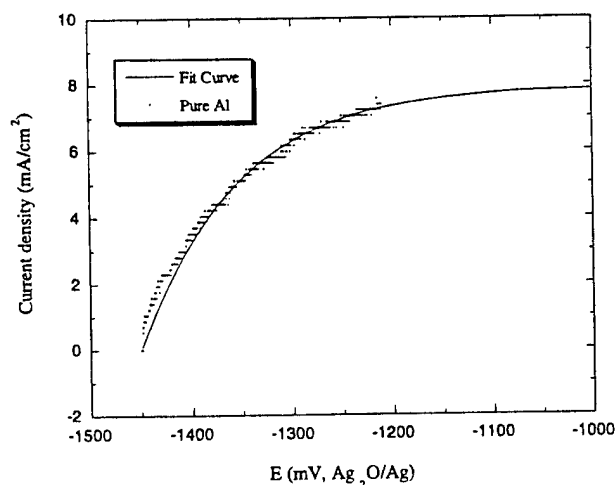
behavior of the S phase, with the critical potential at ~ -450 mV. There is an additional current wave at ~ -100 mV, which corresponds to the wave observed on the copper electrode at $+70$ mV.

Additional insight into the dealloying process can be obtained by analyzing the location of the peak in the current waves in the potentiodynamic curves for the S-phase sample and the pure copper. It is known that the electrochemical reactivity of the more reactive element in alloys is set by clusters of average size, ξ, which intersect the surface of the electrode.[12] The reactivity is expressed as the oxidation potential defined by

$$\Delta E = E(p) - \overline{E} = \frac{\gamma\Omega}{nq}\frac{1}{\xi} \qquad [2]$$

where γ is the liquid/solid interfacial energy, Ω is the atomic volume, n is the number of electrons transferred in the dissolution process, and q is the elementary charge of an electron. E is the reversible potential of flat elemental A defined by Nernst equation. Using the relation above, we can estimate the average initial size of the copper ligaments resulting from S-phase dealloying. For $\gamma \sim 1$ J/m^2, $\Omega = 5 \times 10^{-29}$ m^3, $q = 1.6 \times 10^{-19}$ C, $n = 1$ (Eq. 1) and measuring the potential shift $[E(p) - \overline{E}] = 0.170$ V from Fig. 1, the average initial (prior to coarsening) metal ligament diameter is of order 2 nm.

The curve in Fig. 3 shows the current-time behavior of the S phase sample at a potential of -200 mV where Al is being selectively dissolved. The current shows oscillatory behavior, which has been observed in other systems and is related to a complex interaction between metal dissolution and mass transport effects in the electrolyte.[13] As aluminum dissolves from the S phase above the critical potential, a porous structure develops with pits of order 2 nm in diameter. Metal dissolution within these pits is inhibited by mass transport. The oscillations are related to the stability of a film (possibly a salt film, $NaAlO_2$, or a hydrated oxide) at the bottom of the pits. Film stability is determined by a delicate balance between metal dissolution, ion solubility, and diffusion transport in the electrolyte. As dissolution proceeds, the electrolyte becomes saturated in the aluminate anion, which results in a precipitation event causing the drop in the current owing to film resistance. Mass transport in the electrolyte results in a decrease in the concentration of AlO_2^- to below saturation at the salt film/electrolyte interface. This allows for the chemical dissolution of the film. At this stage the metal starts to dissolve again until the electrolyte near the surface of the metal within the pits is once again saturated in the metal anion and precipitation occurs again. This process occurs in parallel for every pit in the porous structure. Since the transport fields of the pits are coupled, complex nonlinearities develop. Such systems are known to display chaotic behavior.[13]

Figure 2. Curve fit of the potentiodynamic curve for the system Al/0.1 M NaOH + 10^{-3} M AlO_2^- with the function $\eta = $ const $(1 - i/i_d)$. Correlation coefficient, 0.99. $i_d = 7.92$ mA/cm^2.
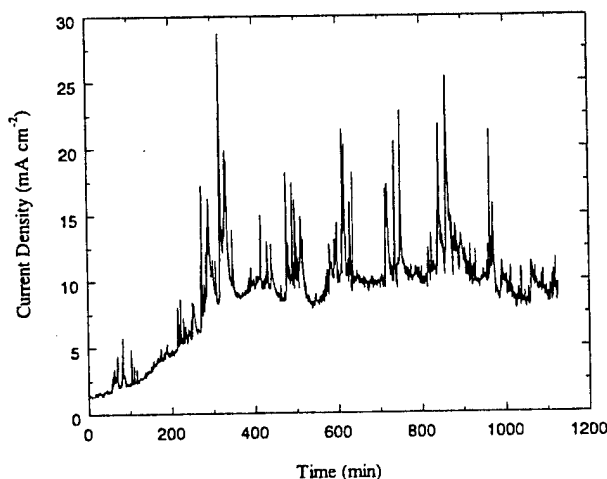

Figure 3. Current-time curve during long-time corrosion of an S-phase sample at a potential of -200 mV.
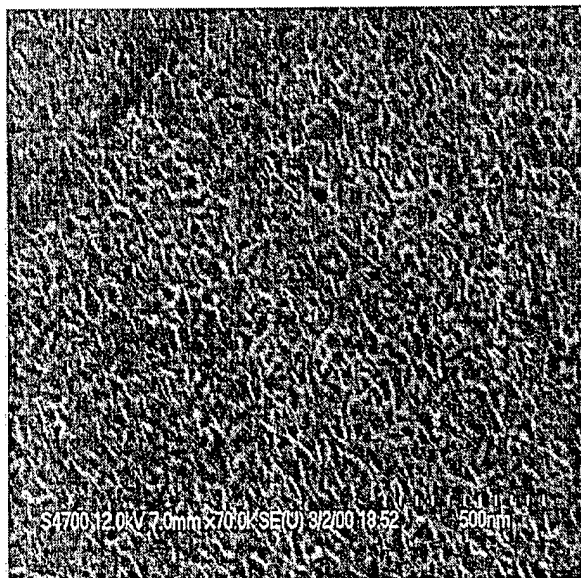
Figure 4. SEM showing the structure of an S-phase sample after 20 h of immersion in 0.1 M NaOH + 10^{-3} M AlO_2^- solution at a potential of -800 mV, which is below the critical potential.

High resolution scanning electron microscopy (SEM).—Following dealloying of the S phase samples we used high resolution SEM to examine the morphology of the surface. Figure 4 shows the morphology of the surface obtained after 20 h of immersion in 0.1 M NaOH + 10^{-3} M AlO_2^- solution at a potential of -800 mV (below the critical potential). The micrograph reveals some morphology evolution related to corrosion, but the bicontinuous microstructure characteristic of a bulk dealloying process[7] does not evolve. Figures 5 and 6 show a bicontinuous dealloying morphology, that resulted from the selective dissolution of S phase after 20 h of immersion in 0.1 NaOH + 10^{-3} M AlO_2^- solution at a potential of -200 mV (above the critical potential). The flatter regions showing "Swiss cheese"-like morphology are typical of room temperature coarsening and sintering processes in dealloying microstructures.[7] Sintering
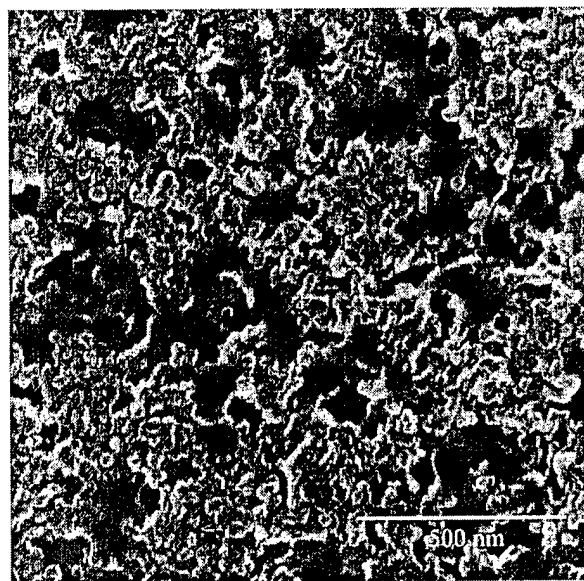

Figure 5. SEM showing the structure of an S phase sample after 20 h of immersion in 0.1 M NaOH + 10^{-3} M AlO_2^- solution at a potential of -200 mV which is above the critical potential.
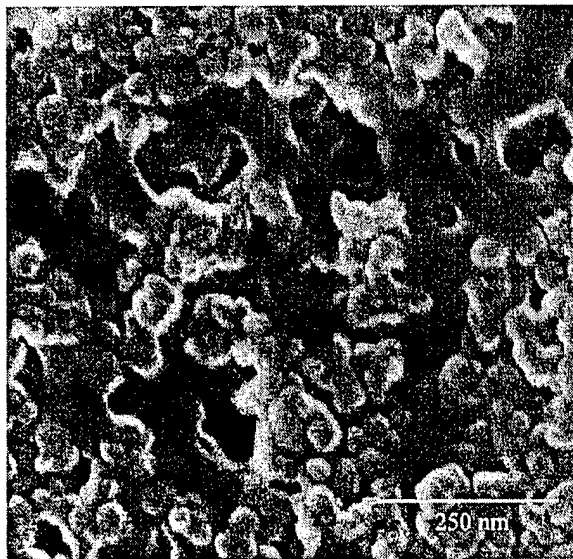

Figure 6. High-magnification SEM showing the structure of S-phase sample after 20 h of immersion in 0.1 M NaOH + 10^{-3} M AlO_2^- solution at a potential of -200 mV.

results from mass-induced collapse of the nanoscale copper-rich ligaments in the near surface region of the porous structure. Beneath this surface layer there is a bicontinuous solid-void microstructure with length scale of order 20-50 nm. This microstructure is reminiscent of the appearance of Cu-Au and Ag-Au surfaces, which have undergone dealloying under appropriate conditions.[7]

Conclusions

We present electrochemical and SEM evidence of S-phase dealloying in an alkaline solution. The current-voltage curve obtained demonstrates critical potential behavior and selective dissolution under the experimental conditions examined. The current-time curve obtained after long-term dealloying suggested a complex interaction between metal dissolution and mass-transport effects in the electrolyte, which resulted in what is probably chaotic behavior of the system investigated. S-phase corrosion above the critical potential resulted in the formation of bicontinuous microstructures, typical of dealloying processes.

Acknowledgments

References

1. Report by the AF Blue Ribbon Advisory Panel on Aircraft Coatings, Part 1-Basic Research, AFOSR (Nov 1995).
2. D. R. Baer and J. Janata, *Science and Technology Master Plan for Chromate Replacement*, AFOSR (Dec 1995).
3. R. G. Buchheit, *J. Electrochem. Soc.*, **142**, 3994 (1995).
4. R. G. Buchheit, R. P. Grant, P. F. Hlava, B. Mckenzie, and G. L. Zander, *J. Electrochem. Soc.*, **144**, 2621 (1997).
5. H. W. Pickering, *Corros. Sci.*, **23**, 1107 (1983).
6. K. Sierdzki, R. R. Corderman, K. Shukla, and R. C. Newman, *Philos. Mag.*, **59**, 713 (1989).
7. K. Sieradzki and R. C. Newman, *J. Phys. Chem. Solids*, **48**, 1101 (1987).
8. *CRC Handbook of Chemistry and Physics*, 78 ed., D. R. Lide, Editor, pp. 5-93, CRC Press, Inc., Boca Raton, FL (1997-1998).
9. J. O'M. Bockris and A. K. N. Reddy, in *Modern Electrochemistry*, Vol. 2, p. 1058, Plenum Press, New York (1977).
10. D. Heeht, P. Borthen, and H. H. Strehblow, *J. Electroanal. Chem.*, **381**, 113 (1995).
11. M. Pourbaix, *Atlas of Electrochemical Equilibria in Aqueous Solutions*, p. 386, NACE, Houston, TX (1974).
12. K. Wagner, S. R. Brankovic, N. Dimitrov, and K. Sieradzki, *J. Electrochem. Soc.*, **144**, 3545 (1997).
13. S. G. Corcoran and K. Sieradzki, *J. Electrochem. Soc.*, **139**, 6 (1992).

14. Schüring, H., Stannarius, R., Tolksdorf, C. & Zentel, R. Liquid crystal elastomer balloons. *Macro-molecules* (submitted).

15. Mach, P., Huang, C. C. & Nguyen, H. T. Dramatic effect of single-atom replacement on the surface tension of liquid-crystal compounds. *Phys. Rev. Lett.* **80**, 732–735 (1998).

16. Johnson, P. M., Pankratz, S., Mach, P., Nguyen, H. T. & Huang, C. C. Optical reflectivity and ellipsometry studies of the Sm-C$_n$* phase. *Phys. Rev. Lett.* **83**, 4073–4076 (1999).

17. Zhao, J., Zhang, Q. M., Kim, N. & Shrout, T. Electromechanical properties of relaxor ferroelectric lead magnesium niobate-lead magnesium titanate ceramics. *Jpn J. Appl. Phys* **34**, 5658–5663 (1995).

18. Poths, H., Anderson, G., Skarp, K. & Zentel, R. Fast electroclinic switching in a ferroelectric LC Polysiloxane. *Adv. Mater.* **4**, 792–794 (1992).

19. Kremer, F. Electromechanical and/or mechanoelectrical converter. German Patent No. 196 36 909 (1998).

20. Semmler, K. & Finkelmann, H. Mechanical field orientation of chiral smectic C-polymer networks. *Macromol. Chem. Phys.* **196**, 3197–3205 (1995).

21. Lehmann, W. *et al.* The electromechanical effect in mechanically oriented S$_C$*-elastomers examined by means of an ultra-stable Michelson interferometer. *Ferroelectrics* **208–209**, 373–383 (1998).

22. Lehmann, W. *et al.* Direct and inverse electromechanical effect in ferroelectric liquid crystalline elastomers. *J. Appl. Phys.* **86**, 1647–1652 (1999).

23. Kremer, F. *et al.* Piezoelectricity in ferroelectric liquid crystalline elastomers. *Polym. Adv. Technol.* **9**, 672–677 (1998).

Supplementary information is available on *Nature*'s World-Wide Web site (http://www.nature.com) or as paper copy from the London editorial office of *Nature*.

···

Evolution of nanoporosity in dealloying

Jonah Erlebacher*†, Michael J. Aziz*, Alain Karma‡, Nikolay Dimitrov§ & Karl Sieradzki§

* *Division of Engineering and Applied Sciences, Harvard University, 9 Oxford Street, Cambridge, Massachusetts 02138, USA*
‡ *Department of Physics and Center for Interdisciplinary Research on Complex Systems, Northeastern University, 360 Huntington Avenue, Boston, Massachusetts 02115, USA*
§ *Department of Mechanical and Aerospace Engineering and Center for Solid State Sciences, Arizona State University, Tempe, Arizona 85287-6106, USA*

···

Dealloying is a common corrosion process during which an alloy is 'parted' by the selective dissolution of the most electro-chemically active of its elements. This process results in the formation of a nanoporous sponge composed almost entirely of the more noble alloy constituents[1]. Although considerable attention has been devoted to the morphological aspects of the dealloying process, its underlying physical mechanism has remained unclear[2]. Here we propose a continuum model that is fully consistent with experiments and theoretical simulations of alloy dissolution, and demonstrate that nanoporosity in metals is due to an intrinsic dynamical pattern formation process. That is, pores form because the more noble atoms are chemically driven to aggregate into two-dimensional clusters by a phase separation process (spinodal decomposition) at the solid–electrolyte interface, and the surface area continuously increases owing to etching. Together, these processes evolve porosity with a characteristic length scale predicted by our continuum model. We expect that chemically tailored nanoporous gold made by dealloying Ag–Au

should be suitable for sensor applications, particularly in a biomaterials context.

Selective dissolution has a long history[3]. For example, the chemical treatment known as depletion gilding selectively dissolves a non-gold element near the surface of a less-expensive alloy such as Au–Cu, leaving behind a surface of pure gold. Early Andean gold-smiths used this technique to enhance the surfaces of their artefacts[4]. In this century, selective dissolution has been primarily examined in the context of corrosion. It is observed in technologically important alloy systems, notably brasses, stainless steels, and Cu–Al alloys[1,5,6]. The mechanical properties of a porous overlayer are very different from the bulk alloy on which it sits, leading to brittle crack propagation, stress corrosion cracking, and other undesirable materials failure[7]. Figure 1 shows the prototypical dealloyed micro-structure, that of nanoporous gold. Early notions considered porosity as a hidden microstructure revealed by etching, but diffraction experiments showed that no pre-existing length scale exists before acid attack on single-phase alloys[8,9]. Later ideas considered the influence of percolating clusters within the solid solution of the alloy, but models failed to yield behaviour consistent with experiment[10,11].

The following argument illustrates the fundamental obstacle to understanding porosity formation during dealloying: consider a silver-gold alloy in an electrolyte under conditions where silver dissolves and gold is inert. Initially, silver will be dissolved from surface sites such as terraces or steps. Gold atoms should accumu-late on the surface and locally block further dissolution. For an alloy containing 10% gold, it might be expected that dissolution would stop or be significantly retarded after about 10 monolayers of the alloy have been dissolved.

A complete model of selective dissolution needs to be multi-scale, involving the kinetics of dissolution, surface diffusion, and mass transport through the bulk of both alloy and electrolyte. Because
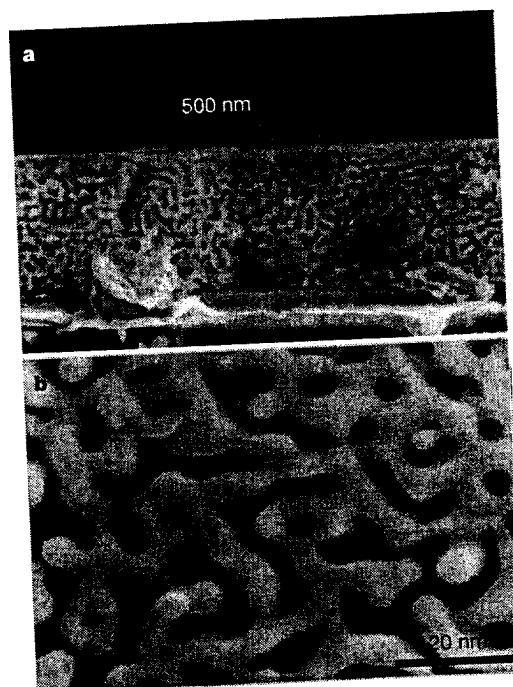
Figure 1 Scanning electron micrographs of nanoporous gold made by selective dissolution of silver from Ag-Au alloys immersed in nitric acid under free corrosion conditions. **a**, Cross-section of dealloyed Au$_{32\%}$Ag$_{68\%}$ (atom%) thin film. **b**, Plan view of dealloyed Au$_{26\%}$Ag$_{74\%}$ (atom%). The porosity is open, and the ligament spacings shown in **b** are of the order of 10 nm; spacings as small as 5 nm have been observed. Measurements of the surface area of nanoporous gold are of the order of order 2 m^2 g^{-1} (refs 24, 25), comparable to commercial supported catalysts.

† Present address: Department of Materials Science and Engineering, Johns Hopkins University, Baltimore, Maryland 21218, USA.

mass transport through the bulk of the growing phase (the electrolyte) is always a stabilizing influence[12], and because mass transport through the bulk of the dissolving phase appears too slow to be significant, we hypothesized that the morphology-determining physical process is confined to the interface region between the alloy and the electrolyte. To test this, we developed a kinetic Monte Carlo model to simulate Ag-Au dealloying, including only diffusion of silver and gold and dissolution of silver[13]. We found that this model was able to reproduce all relevant experimental trends characteristic of dealloying, both morphological and kinetic.

Figure 2 shows a simulated porous structure with ligament widths of 2–5 nm. Our simulations were successful in modelling the nanoporous morphology, and also in modelling the dynamic behaviour of the dissolution current versus overpotential. It is a well characterized feature of alloy dissolution that as the overpotential is increased (usually at rates of the order of a few millivolts per second), the dissolution current of ions from the alloy stays at a low level until a bulk-composition-dependent critical potential (V_C) is reached, at which point this current rises rapidly[14]. Figure 3 shows simulated and experimental polarization curves for different alloy compositions. There is clear observation of a composition-dependent V_C. To our knowledge, this is the first simulation model to produce such behaviour, suggesting that we have found a minimum set of physical processes to include in any model for

alloy dissolution.

The simulations reveal the following qualitative picture of porosity formation. The process starts with the dissolution of a single silver atom on a flat alloy surface of close-packed (111) orientation, leaving behind a terrace vacancy. The atoms coordinating this vacancy have fewer lateral near-neighbours than other silver atoms in the terrace, and are thus more susceptible to dissolution. As a result, the entire terrace is 'stripped', leaving behind gold atoms with no lateral coordination ('adatoms'). Before the next layer is attacked, these gold adatoms diffuse about and start to agglomerate into islands. As a result, rather than a uniform diffuse layer of gold spread over the surface, the surface is comprised of two distinct kinds of regions—pure gold clusters that locally passivate the surface, and patches of un-dealloyed material exposed to electrolyte. When silver atoms in these patches dissolve, more gold adatoms are released onto the surface. These adatoms diffuse to the gold clusters left over from dissolution of previous layers, continuing to leave un-dealloyed material exposed to electrolyte. In the early stages, these gold clusters are mounds that are gold-rich at their peaks and that have alloy composition at their bases. These mounds get undercut, increasing the surface area that gold must cover to bring about passivation. Ultimately, this leads to pit formation and porosity.

Central to this description is the the coalescence of gold adatoms into stable clusters. The spacing between these 'islands' in the initial stages of dissolution is close to the spacing between ligaments in the final porous structure. The physical reason for this coalescence can be understood by considering the gold adatoms to be one component of a two-component solution of gold and 'electrolyte' confined to the monolayer-thick interfacial layer sitting on top of un-dealloyed material. We modelled the thermodynamics of the interfacial layer as a regular solution[15], and found the solubility of gold in electrolyte within the interfacial layer to be of the order of 10^{-7} per site (see Methods). This solubility may be interpreted as the 'equilibrium concentration of gold adatoms' on the surface of the alloy—in the absence of etching, it represents a dynamic equilibrium of adatoms resulting from their two-dimensional evaporation from step edges onto terraces and their subsequent recondensation.

In contrast to the equilibrium condition, rapidly stripping a terrace of silver atoms leaves gold adatoms with a local site occupancy fraction equal to that in the bulk, typically 10–40%— far above their equilibrated concentration of 10^{-7} per site. Thus, there is an extremely strong driving force for gold adatoms to condense onto nearby gold-rich clusters. In fact, regions of surface with high enough supersaturation of gold adatoms sit 'within the spinodal', a special segment of the curve representing free energy f of a spatially uniform layer versus gold concentration C for which $\partial^2 f / \partial C^2 < 0$. Within the spinodal, composition fluctuations of infinitesimal amplitude lead to a lower overall free energy for the

Figure 2 Simulated nanoporous gold. The simulation model was as follows: a bond-breaking model was used for diffusion; atoms with N near neighbours diffused with rate $k_N = \nu_D \exp(-N\epsilon/k_B T)$, where ϵ is a bond energy and $\nu_D = 10^{13}$ s^{-1}. Dissolution rates were consistent with the Butler–Volmer (BV) equation in the high-driving-force Tafel regime; the dissolution rate $k_{E,N}$ for a silver atom with N near neighbours was written as $k_{E,N} = \nu_E \exp[-(N\epsilon - \phi)/k_B T]$, where $\nu_E = 10^4$ s^{-1} is an attempt frequency determined by the exchange-current density in the BV equation and ϕ is the overpotential. For the figure, $\phi = 1.75$ eV, $\epsilon/k_B T = 5.51$.
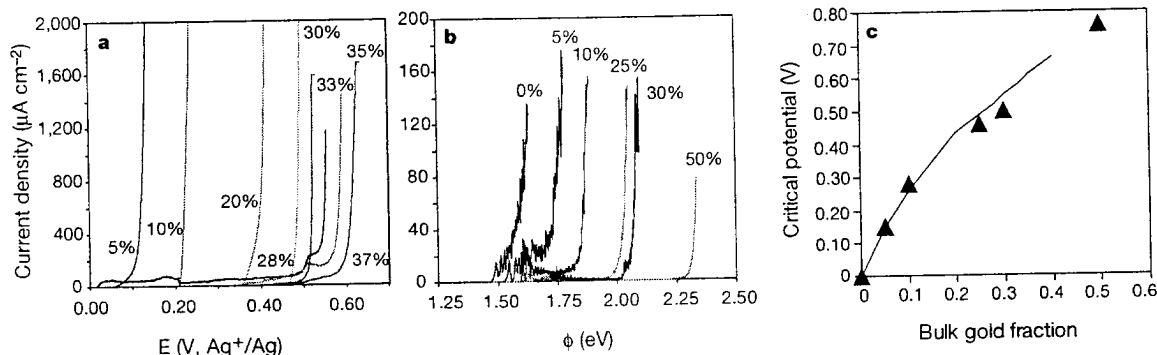

Figure 3 Comparison of experimental and simulated current–potential behaviour. **a**, Current–potential behaviour for varying Ag-Au alloy compositions (atom% Au) dealloyed in 0.1 M HClO$_4$ + 0.1 M Ag$^+$(reference electrode 0.1 M Ag$^+$/Ag). **b**, Simulated current–potential behaviour of Ag-Au alloys. **c**, Comparison of experimental (line) and simulated (triangles) critical potentials; the zero of overpotential has been set equal to the onset of dissolution of pure silver both in simulation and in experiment.

system, and involve atomic diffusion against concentration gradients (the 'uphill diffusion' process through which gold condenses onto nearby clusters), that is, the system is inherently unstable and will spontaneously phase-separate. But fluctuations of long length scale grow slowly due to the required diffusion times, and short-length-scale fluctuations create much energetically unfavourable incipient interface between the phases, inhibiting their growth. Hence, phase separation is manifested most rapidly at an intermediate length scale that roughly corresponds to the spacing between the observed gold-rich clusters. This effect is known as spinodal decomposition[16,17]. As porosity forms, the decomposition is occurring on a non-flat, non-uniform surface with continuously increasing surface area.

In our model, the motion of the alloy–electrolyte interface is fully described mathematically by the flux of diffusing adatoms J_S, the velocity of the interface normal to itself v_n, and the concentration accumulation rate $\partial C/\partial t$, all of which are interrelated and vary with position along the curve of the interface (for detailed derivations, see Methods). For J_S, we used a model for diffusion during spinodal decomposition known as the Cahn–Hilliard equation[17]. The normal velocity depends on C and also on the local curvature κ through capillary effects[11]. The time evolution of C is uniquely determined by the local mass-conservation condition

$$\partial C/\partial t = v_n C_0 - v_n \kappa C - \nabla \cdot J_S \qquad (1)$$

where C_0 is the bulk gold concentration. This condition is analogous to the local conservation of heat or solute appearing in boundary-layer models of solidification[18], with two important differences: (1) the interfacial layer thickness is constant along the interface, and is microscopic, rather than being a spatially varying macroscopic diffusion length, and (2) the surface aggregation process inherent in the Cahn–Hilliard form for J_S is essential for porosity formation. Simple ('downhill') surface diffusion ($J_S = -D_S \nabla C$) yields an

Figure 4 Simulated evolution of an artificial pit in $Au_{10\%}Ag_{90\%}$ (atom%), $\phi = 1.8$ eV. Cross-sections along the $(1\bar{1}1)$ plane defined by the yellow line in **a** are shown below each plan view. **a**, The initial condition is a surface fully passivated with gold except within a circular region (the 'artificial pit'). **b**, After 1 s, the pit has penetrated a few monolayers into the bulk. We note how there are fewer gold clusters near the side wall than at the centre of the pit. **c**, After 10 s, a gold cluster has nucleated in the centre of the pit. **d**, At 100 s, the pit has split into multiple pits; each will continue to propagate into the bulk to form a porous structure like that in Fig. 2.

initially unstable interface that passivates quickly, before well-formed pores have a chance to develop. Cahn–Hilliard diffusion also dominates capillarity-driven surface diffusion—the effect usually incorporated into interface evolution equations[19].

We performed numerical integration of equation (1) using a relative arc-length parametrization scheme[20,21], and parameters that matched those used in the kinetic Monte Carlo simulations. We observed, as expected, the evolution of gold clusters separated by a characteristic spacing λ. An analytic expression for λ can be found by a time-dependent linear stability analysis of equation (1) that takes into account the slow increase of gold concentration into the interfacial layer as the instability develops. This effect needs to be included because the spatial period with the largest amplification rate depends sensitively on the gold concentration. Specifically, this spatial period decreases sharply as the concentration increases past a threshold concentration for instability that corresponds to the spinodal point $\partial^2 f/\partial C^2 = 0$, and the interface is stable for concentrations below this threshold. We find a maximally unstable spatial period that scales as $\lambda \propto (D_S/V_0)^{1/6}$, where V_0 is the velocity of a flat alloy surface with no gold accumulated upon it. This prediction is in qualitative agreement with both kinetic Monte Carlo simulations and experiments, both of which show that the characteristic length scale of porosity decreases with increasing driving force. A more elaborate analysis incorporating nonlinear effects, however, remains needed for a detailed quantitative comparison.

There is an analogy between this result, applicable to etching, and two-dimensional island nucleation during submonolayer vapour phase deposition. Namely, in the early stages of etching, the dissolution process is analogous to deposition of gold; in both processes, adatoms are added to the surface where they are free to agglomerate into islands. The case of vapour phase deposition has been studied using rate equations that describe an aggregation process where adatoms stick together irreversibly. In these studies it is a well-known result that the island spacing scales as $(D_S/F)^\mu$, where the deposition rate F is the direct analogue of the surface velocity in etching, and the exponent μ depends on details of the aggregation process (see ref. 22 and references therein). That these results are limited to irreversible aggregation during deposition and our analysis is for reversible aggregation during etching suggests the existence of universal scaling laws for aggregation that do not depend on reversibility or the lack thereof in these two opposite processes.

Our kinetic Monte Carlo simulation elucidates the later stages of morphological evolution, and the mechanism by which three-dimensional porosity evolves. We highlight the features of this process by showing in Fig. 4 a simulation of an artificial pit in an otherwise fully passivated surface. When the pit reaches sufficient depth, its surface area has increased sufficiently that a new gold cluster nucleates. When this happens, the pore splits into multiple new pits, each with a smaller surface area than its parent. These 'child' pits continue to penetrate into the bulk, increasing their surface area, nucleating new clusters, spawning new pits, and so on, until a full, three-dimensional porous structure evolves, such as those illustrated in Figs 1 and 2. □

Methods

In a regular solution, the enthalpy of mixing depends on the bond energies and the entropy of mixing is ideal. The free energy of a regular solution $f(C,T)$ is written $f = \alpha c(1 - c) + k_B T[c \ln c + (1 - c)\ln(1 - c)]$, where c is the mole fraction of gold ($c = C\Omega^{2/3}$, where Ω is atomic volume), $\alpha = 6[E_{Au-electrolyte} - (1/2)(E_{Au-Au} + E_{electrolyte-electrolyte})]$, where E_{x-x} are the respective interaction energies between Au and electrolyte, the prefactor 6 is the lateral coordination in the two-dimensional hexagonal lattice of the interfacial layer, k_B is Boltzmann's constant and T is absolute temperature. For our simulation conditions, realistic timescales and length scales were obtained from the parameters $E_{Au-Au} = -0.285$ eV ($= -\epsilon$, the simulation bond energy as described in Fig. 2), $T = 600$ K, $E_{Au-electrolyte} = E_{electrolyte-electrolyte} = 0.0$ eV. With these parameters, $\alpha = 0.855$ eV. The free energy has the familiar double-well form[23] and a minimum at $c \approx 10^{-7}$ per site, representing the solubility of gold in electrolyte (and vice versa).

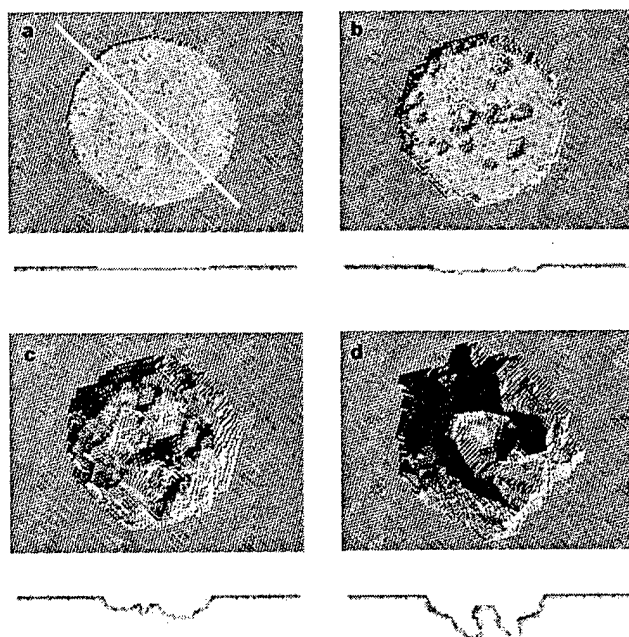The Cahn–Hilliard diffusion equation is $J_S = -M(C)(\partial^2 f/\partial c^2)\nabla C + 2M(C)w\nabla^3 C$.

Here, 453$M(C)$ is a mobility, w is the so-called gradient energy coefficient, and the gradients are taken with respect to arc length. The first term on the right-hand side describes the chemical effect leading to phase separation within the spinodal; the second term describes the effect that damps short-wavelength fluctuations. The mobility is proportional to the surface diffusivity D_S and is given by $M(C) = (D_S/k_B T)c(1-c)$. The mobility is peaked for $c = 0.5$, and is zero for $c = 0$ and $c = 1$ (atoms do not diffuse in pure phases because there are no vacancies in our model). The normal velocity is given by $v_n(C) = V(C)[1 - (\gamma\Omega/k_B T)\kappa]$, where γ is the surface free energy and $V(C)$ is called the interface response function, equal to the velocity of a flat surface covered with a concentration C of gold. We find in both simulation and experiment that the interface response is fitted well by the functional form $V(C) = V_0(\phi)\exp(-C/C^*)$, where ϕ is the overpotential and C^* is a constant. Experimentally, the gold accumulation can be inferred by integrating the dissolution current versus time at fixed overpotential; it is necessary to use an overpotential that is low enough to ensure that the surface remains planar (that is, porosity does not form) and also to catch the short initial transient rise in current as silver atoms are pulled from the first few monolayers. This particular form for the interface response function is quite curious. Naively, one might expect that the local interface velocity would be proportional to the local concentration of silver exposed to the electrolyte, that is, $V(C) \propto (1 - c)$. However, the decaying exponential form suggests that there is an evolving distribution of holes opening and closing within the interfacial region, controlling the accumulation rate.

Physically, the mass conservation condition (equation (1)) is the statement that the total number $Cb\Delta s$ of gold atoms in a length Δs of interface with lateral width b can change as a result of three distinct effects that correspond to the three terms on the right-hand-side of equation (1): the accumulation of gold atoms into the interfacial layer from the solid being dissolved; the local stretching of the interface ($\partial \Delta s/\partial t = v_n \kappa \Delta s$), which can either increase or decrease C depending on whether the solid is concave ($\kappa > 0$) or convex ($\kappa < 0$); and the motion of atoms along the interface driven by the surface diffusion flux J_S.

1. Pickering, H. W. Characteristic features of alloy polarization curves. *Corros. Sci.* 23, 1107–1120 (1983).
2. Forty, A. J. Corrosion micromorphology of noble metal alloys and depletion gilding. *Nature* 282, 597–598 (1979).
3. Masing, G. Zur Theorie der Resistenzgrenzen in Mischkristallen. *Z. Anorg. Allg. Chem.* 118, 293–308 (1921).
4. Lechtman, H. Pre-Columbian surface metallurgy. *Sci. Am.* 250, 56–63 (1984).
5. Williams, D. E., Newman, R. C., Song, Q. & Kelly, R. G. Passivity breakdown and pitting corrosion of binary alloys. *Nature* 350, 216–219 (1991).
6. Newman, R. C. & Sieradzki, K. Metallic Corrosion. *Science* 263, 1708–1709 (1994).
7. Li, R. & Sieradzki, K. Ductile-brittle transition in random porous Au. *Phys. Rev. Lett.* 68, 1168–1171 (1992).
8. Corcoran, S. in *Critical Factors in Localized Corrosion III* (eds Kelly, R. G., Frankel, G. S., Natishan, P. M. & Newman, R. C.) 500–507 (Electrochemical Society, Pennington, New Jersey, 2000).
9. Pickering, H. W. & Wagner, C. Electrolytic dissolution of binary alloys containing a noble metal. *J. Electrochem. Soc.* 114, 698–706 (1967).
10. Sieradzki, K., Corderman, R. R., Shukla, K. & Newman, R. C. Computer simulations of corrosion: selective dissolution of binary alloys. *Phil. Mag. A* 59, 713–746 (1989).
11. Sieradzki, K. Curvature effects in alloy dissolution. *J. Electrochem. Soc.* 140, 2868–2872 (1993).
12. Wagner, C. Contribution to the theory of electropolishing. *J. Electrochem. Soc.* 101, 225–228 (1953).
13. Erlebacher, J. in *Dynamics of Crystal Surfaces and Interfaces* (eds Duxbury, P. & Pence, T.) 24–28 (Plenum, New York, 1997).
14. Wagner, K., Brankovic, S. R., Dmitrov, N. & Sieradzki, K. Dealloying below the critical potential. *J. Electrochem. Soc.* 144, 3545–3555 (1997).
15. Cahn, J. W. & Hilliard, J. E. Free energy of a nonuniform system. I. Interfacial free energy. *J. Chem. Phys.* 28, 258–267 (1958).
16. Cahn, J. W. & Hilliard, J. E. Free energy of a nonuniform system. III. Nucleation in a two-component incompressible fluid. *J. Chem. Phys.* 31, 688–699 (1958).
17. Hilliard, J. E. in *Solidification* 497–560 (American Society for Metals, Metals Park, Ohio, 1971).
18. Ben-Jacob, E., Goldenfeld, N., Langer, J. S. & Schon, G. Dynamics of interfacial pattern formation. *Phys. Rev. Lett.* 51, 1930–1932 (1983).
19. Mullins, W. W. Theory of thermal grooving. *J. Appl. Phys.* 28, 333–339 (1957).
20. Kessler, D. A., Koplik, J. & Levine, H. Geometrical models of interface evolution. II. Numerical simulation *Phys. Rev. A* 30, 3161–3174 (1984).
21. Hou, T. Y., Lowengrub, J. S. & Shelley, M. J. Removing the stiffness from interfacial flow with surface tension. *J. Comp. Phys.* 114, 312–338 (1994).
22. Barabasi, A. -L. & Stanley, H. E. *Fractal Concepts in Surface Growth* (Cambridge Univ. Press, 1995).
23. Haasen, P. *Physical Metallurgy*, (Cambridge Univ. Press, 1986).
24. Forty, A. J. in *Sir Charles Frank: An 80th Birthday Tribute* (ed. Chamber, R .G.) 164–187 (Adam Hilger, Bristol, 1991).
25. Tulimieri, D. J., Yoon, J. & Chan, M. H. W. Ordering of helium mixtures in porous gold. *Phys. Rev. Lett.* 82, 121–124 (1999).

Correspondence and requests for materials should be addressed to J.E (e-mail: Jonah.Erlebacher@jhu.edu).

Ice shelves in the Pleistocene Arctic Ocean inferred from glaciogenic deep-sea bedforms

Leonid Polyak*, Margo H. Edwards†, Bernard J. Coakley‡ & Martin Jakobsson§||

* Byrd Polar Research Center, Ohio State University, Columbus, Ohio 43210, USA
† Hawaii Mapping Research Group, Hawaii Institute of Geophysics and Planetology, University of Hawaii, Honolulu, Hawaii 96822, USA
‡ Department of Geology, Tulane University, New Orleans, Louisiana 70118, USA
§ Department of Geology and Geochemistry, Stockholm University, 106 91 Stockholm, Sweden

It has been proposed that during Pleistocene glaciations, an ice cap of 1 kilometre or greater thickness covered the Arctic Ocean[1-3]. This notion contrasts with the prevailing view that the Arctic Ocean was covered only by perennial sea ice with scattered icebergs[4-6]. Detailed mapping of the ocean floor is the best means to resolve this issue. Although sea-floor imagery has been used to reconstruct the glacial history of the Antarctic shelf[7-9], little data have been collected in the Arctic Ocean because of operational constraints[10,11]. The use of a geophysical mapping system during the submarine SCICEX expedition in 1999[12] provided the opportunity to perform such an investigation over a large portion of the Arctic Ocean. Here we analyse backscatter images and sub-bottom profiler records obtained during this expedition from depths as great as 1 kilometre. These records show multiple bedforms indicative of glacial scouring and moulding of sea floor, combined with large-scale erosion of submarine ridge crests. These distinct glaciogenic features demonstrate that immense, Antarctic-type ice shelves up to 1 kilometre thick and hundreds of kilometres long existed in the Arctic Ocean during Pleistocene glaciations.

The central Arctic Ocean contains relatively shallow areas (water depths <1,000 m; see Fig. 1) on Yermak plateau, Lomonosov ridge and Chukchi borderland—which includes Chukchi plateau, Chukchi rise and Northwind ridge. During the SCICEX-99 expedition, conducted on the nuclear-powered submarine USS *Hawkbill*, shallow sea-floor areas were targeted for mapping to detect glaciogenic bedforms. Sea-floor images (collected using a submarine-mounted 12-kHz swath bathymetry and sidescan sonar[12]) from the Chukchi borderland and the Lomonosov ridge show a variety of bedforms, including random or subparallel scours, parallel lineations, and transverse ridges. On the records from the chirp sub-bottom profiler, these bedforms are associated with planed ridge crests with rough microrelief and obvious angular unconformities cut into the stratified sediments.

Randomly oriented furrows, typically <100-m wide and up to 30-m deep, densely cover the shallowest, <400-m-deep portions of sea floor on the Chukchi borderland and adjacent continental margin (Fig. 2a). Isolated larger scours up to 700-m wide and over 10-km long occur as deep as 500 m. Even greater depths, exceeding 900 m, are attained by closely spaced, subparallel scours on the Lomonosov ridge. Sea-floor scours are known to be formed by the drift of icebergs and pack-ice ridges[13]. At present, icebergs in the Arctic Ocean have at most 50-m draughts[14], whereas icebergs off Antarctica and Greenland reach depths of 500–550 m (refs 15, 16). The largest depths of gouged sea floor, extending to 850 m, have been reported from the Yermak plateau[10], matching the depth of sours on the Lomonosov ridge.

Below the depth range of dense scouring, the sea floor exhibits

|| Present address: Center for Coastal Mapping, University of New Hampshire, Durham, New Hampshire 03824, USA.

Dealloying and Corrosion of Al Alloy 2024-T3

M. B. Vukmirovic,[a,*] N. Dimitrov,[b,**] and K. Sieradzki[a,b,c,**,z]

[a]Program in The Science and Engineering of Materials, [b]Department of Mechanical and Aerospace Engineering, and [c]Department of Chemical Engineering and Materials Science, Arizona State University, Tempe, Arizona 85287-6106, USA

We present results of a comprehensive electrochemical study aimed at determining the factors that control the corrosion evolution of the important structural alloy Al 2024-T3. An important aspect of corrosion in this alloy is copper redistribution. The redistributed copper serves to enhance the kinetics of the corrosion process and presents some major difficulties with respect to development of new families of conversion coatings. Two major sources of "mobile" copper are discussed, the Al_2CuMg S-phase and copper in solid solution. In each case, a dealloying mechanism is responsible for liberating copper that becomes available to redistribution by solid state and/or liquid phase transport mechanisms. This work is concerned with identifying the relative importance of these sources of copper and the active transport mechanisms. In order to decouple the sources of copper, we designed "synthetic" 2024 alloys that emulate the oxygen reduction kinetics of the real alloy. Our results indicate that, in principal, both sources of copper are operative during redistribution and, for the particular alloy that we examined, both contribute about equally to the amount of redistributed copper.
© 2002 The Electrochemical Society. [DOI: 10.1149/1.1498258] All rights reserved.

Copper redistribution occurs on the surface of copper containing aluminum alloys such as 2024-T3 as a result of dealloying. There are two principal sources of copper in the alloy: intermetallic copper containing precipitate particles such as the orthorhombic S-phase (Al_2CuMg) in 2024-T3, and copper in solid solution.[1-4] Henceforth, we refer to dealloying of matrix aluminum and the buildup of copper from solid solution as matrix dealloying. The surface coverage of S-phase particles on 2024-T3 is of order 0.03 area fraction,[1] and there is ~0.2 to 0.5 wt % Cu in solid solution.[5] Assuming a mean S-phase particle diam of 1 μm, the mean interparticle separation is ~5 μm.

Figure 1 is a schematic illustration of S-phase dealloying which occurs in corrosive environments containing, for example, chlorides, or a commercial deoxidizing pretreatment solution. Various researchers have also noted similar effects during polishing of these alloys in nominally pure water.[6-9] The oxide on the surface of the S-phase is not very protective and a fluctuation (transient breakdown event) or heterogeneity in the oxide exposes bare metal to the electrolyte. Once this event occurs, Mg dissolves into the electrolyte as the soluble Mg^{2+} cation. The dynamics of this process transiently inhibits repassivation and this allows for aluminum dissolution from the S-phase. The remaining Cu forms a very high surface area porous sponge structure as shown in Fig. 2, which is typical of bicontinuous dealloyed microstructures.[10] Thus the S-phase is initially anodic, but after dealloying, turns into a high surface area cathode for oxygen reduction. As long as the remnant Cu sponge remains mechanically and electrically connected to the Al matrix the corrosion potential is too low to allow for Cu dissolution by electrochemical means. However, if the particles of the Cu sponge are mechanically disconnected (Fig. 1b-d), the copper particle will dissolve at its corrosion potential in, for example, a Cl⁻ electrolyte, and electrochemically plate back onto the aluminum alloy surface. We have performed separate tests which confirm this scenario. The electrodeposition of dissolved copper onto the oxide covered alloy surface may at first seem surprising, but there are regions of this surface that are at least transiently bare. Additionally, the oxide on the alloy surface is undoubtedly highly defective and a semiconductor.[11]

In a neutral chloride solution, oxygen reduction occurs according to $2H_2O + O_2 + 4e^- = 4(OH)^-$, which results in an increase in the pH of the electrolyte in the neighborhood of local cathodes. The Cu-rich remnant S-phase sponge serves as cathode for this reaction. As the pH increases to about the range 9-9.5,[8,12,13] the passive oxide on the surface of the alloy matrix will chemically dissolve and the bare aluminum will begin to selectively dissolve via the soluble AlO_2^- anion. This scenario is illustrated in Fig. 3. As hydroxide is produced at a local cathode, it diffuses radially outward activating an ever increasing surface area surrounding the cathode to alkaline dissolution of aluminum. This matrix dealloying process results in the agglomeration of solid solution Cu into Cu particles that also serve as cathodic sites available to support yet more oxygen reduction. Additionally, dissolution of aluminum will bring new precipitate particles to the surface, which can activate anodically and subsequently turn in to reduction sites. This situation is complicated further, since the cathodes have finite lifetimes. A copper particle can stop functioning as a cathode either because it eventually is undercut by alkaline dissolution of aluminum and becomes disconnected, or from buildup of a gel-like aluminum hydroxide which blocks the cathode from access to oxygen.

Figure 4 is a schematic illustration of the growth of the zone of increased pH in the vicinity of a dealloyed S-phase particle. In the long-term limit, the growth of the zone will be dictated by the geometry of overall mass transport in the electrolyte, either radial diffusion of O_2 toward the cathode or $(OH)^-$ diffusion radially away from the cathode. Each dealloyed particle behaves as a microelectrode, since the particle diameter is considerably smaller than the width of the diffusion boundary layer. Thus, the zone of increased pH is initially planar (when the zone size is of the order of the cathode diameter) with Cottrellian current but eventually adopts the hemispherical growth front that characterizes the diffusive field. The zone grows in this geometry until its radius is of the order of the diffusion boundary layer thickness (10-100 μm) at which point the growth of the zone is cut off. Thus the diffusion boundary layer thickness sets an upper limit on the radius of the increased pH zone that can be developed by a single particle.

If the mean S-phase particle diameter is 1 μm, then the average separation between particles will be ~5 μm corresponding to an ~0.03 area fraction surface coverage of copper. Figure 5 illustrates the growth and overlap of these zones of increased pH emanating from an array of these cathode microelectrodes. If the mean particle spacing is less than the diffusion boundary layer thickness, the hemispheres of increased pH overlap. As this occurs, the diffusion field switches from radial to a one-dimensional (1-D) field in the direction of the surface normal and the current becomes Cottrellian. In this case, the entire surface is activated to matrix dealloying and a significant increase in the surface copper concentration develops. This situation is physically similar to that of a nucleation and growth
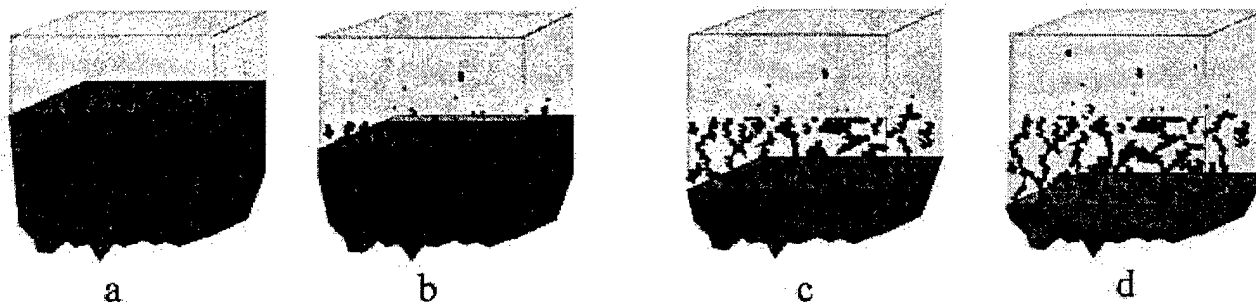
Figure 1. Schematic illustration showing dealloying of an S-phase particle. (a) The quenched-in atomic structure of an S-phase particle prior to dealloying. Only the atomic-scale copper in this structure is shown. (b) As the aggressive fluid phase removes Mg and Al, the remnant Cu forms a nanometer-scale porous sponge structure part of which is mechanically disconnected from the solid surface in the electrolyte. (c) As the porous Cu structure evolves more Cu particles, on the order of tens of nanometers in diameter, are liberated and (d) is a continuation of this process. Box size length scale, 1 μm.

process with overlapping growth fronts. It is known that such a process is described by Avrami growth kinetics; thus the partial current of either oxygen reduction or aluminum dissolution should be given by an equation of the form $I = 1 - \exp(-\alpha t^n)$. Here, I is the normalized current density (normalized to the value characteristic of a fully activated surface), α is a constant related to the geometry of the extending zone of increased pH, and n corresponds to 1 + the dimension of the growth assuming a continuous nucleation process. This situation is, however, complicated by the fact that cathodes are dying out, and the "nucleation time" of the cathode is controlled by fluctuations. Thus a proper formulation of this problem must include terms that correspond to both cathode nucleation processes and cathode extinction processes.

This paper is aimed at addressing the relative contributions of each of the mechanisms described above to copper redistribution on the surface of Al alloy 2024-T3. The manuscript is organized as follows. In the next section we describe the general experimental methods used in this study. Then we present results from rotating disk electrode (RDE) and rotating ring-disk electrode (RRDE) studies for copper redistribution on the surface of Al alloy 2024-T3 (real

2024) and synthetic 2024-T3 (synthetic 2024) alloys. Finally, we present results for oxygen diffusion-limited current densities on RDEs and in the conclusions, we knit together all the results in a model that presents a coherent qualitative picture of corrosion and copper redistribution on the surface of Al alloy 2024-T3.

Experimental

Sample preparation.—We used five different kinds of samples in our study, Al 2024-T3 alloy, Al-1 wt % Cu solid solution alloys, synthetic 2024 (see the section on Synthetic 2024-T3 and Cu microelectrode samples), arrays of Cu microelectrodes embedded in an insulator (CEI), and pure Cu. Unless otherwise noted, all electrodes were in the shape of a disk cut from sheets with diam 6.15 mm and area of 0.3 cm². The chemical composition (weight percent) of the 2024-T3 material was as follows: 3.8-4.9 Cu, 1.2-1.8 Mg, 0.3-0.9 Mn, 0.5 Si and Fe, 0.25 Zn, 0.1 Cr, and 0.05 Ti. The chemical composition (weight percent) of the solid solution alloys was as follows: Al-1% Cu-0.98 Cu, 0.001 Si, 0.002 Ti, 0.001 Zn; Al-4% Cu-3.96 Cu, 0.001 Si, 0.002 Ti, and 0.001 Zn.

All sample disks were mechanically polished down to 3 μm with successively finer Buehler Carbimet grinding paper that was lubricated with ethylene glycol. Further polishing was performed using a nonaqueous alumina slurry (suspension of Buehler Micropolish II deagglomerated alumina polishing powder in ethylene glycol) down to 0.05 μm. Following polishing, the sample disks were rinsed with ethanol. Water was not used during the polishing procedure owing to previous literature that reported accumulation of Cu on the surface and grooving around intermetallic particles during polishing of Al 2024-T3 that used water in the slurry.[6-9]

Synthetic 2024-T3 and Cu microelectrode samples.—After polishing, some of the Al-1 wt % Cu disks were transferred to a cleanroom where standard photolithographic techniques were used to make prescribed arrays of copper dots on the surface of the Al-Cu solid solution alloy disks and copper dots embedded in an insulator
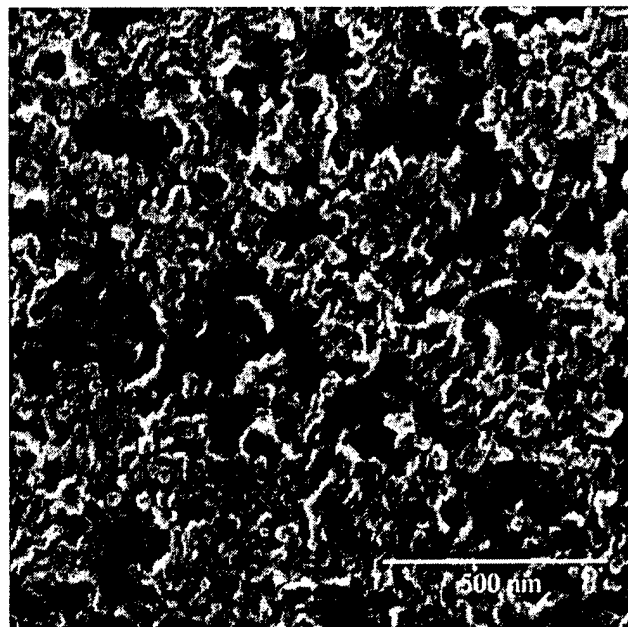

Figure 2. SEM showing the structure of a dealloyed S-phase sample after 20 h of immersion in 0.1 M NaOH + 10^{-3} M AlO_2^- solution.
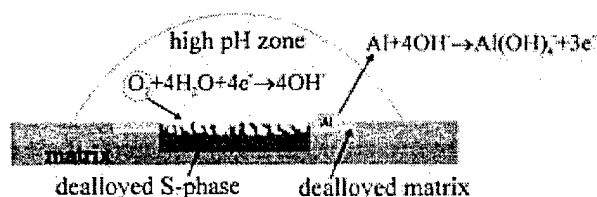

Figure 3. Schematic illustration of matrix dealloying in the vicinity of an S-phase particle on the surface of Al 2024-T3. The dealloyed S-phase serves as cathode active to oxygen reduction and the surrounding matrix undergoes Al dealloying causing a local enrichment of copper.
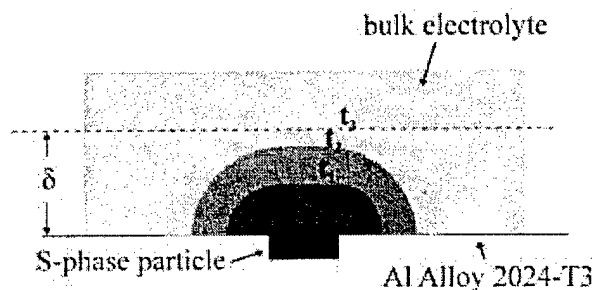
Figure 4. A schematic illustration of the growth zone of elevated pH around the dealloyed S-phase particle illustrating the planar diffusion front at times, t_0, and the hemispherical shape of the zone at later times, t_3. δ is the thickness of the diffusion boundary layer. The shaded colors correspond to the shape and extent of the pH 9.5 zone as time evolves.

(CEI).[14] Three different types of square lattice arrays of 100 nm thick copper dots were produced with dot diam of 1.8, 80, and 1000 μm. Samples with 80 and 1000 μm diam Cu particles were made with square shaped matrix samples, 3 cm on a side. Since the dots covered an ~0.03 area fraction of the Al-1 wt % Cu alloy surface, the lattice sizes (interdot spacing) were 9.5, 400, and 5000 μm, respectively.

Figure 6 ($t = 0$ h) shows a synthetic 2024 alloy made using an Al-1 wt % Cu solid-solution alloy with 1.8 μm diam Cu dots in a square array with nearest-neighbor spacing of 9.5 μm.

RDE studies.—RDE studies were performed on the synthetic and real 2024 alloy samples in order to ascertain the amount of accumulated Cu on the surface as a function of rotation rate and time, and to measure oxygen diffusion-limited current densities as a function of rotation rate. Oxygen diffusion-limited current densities were also measured on planar Cu disks and CEI samples as a function of rotation rate. All of the experiments designed to measure oxygen diffusion-limited current densities were done in a 0.1 M Na_2SO_4 electrolyte under a prescribed rotation rate by performing an anodic
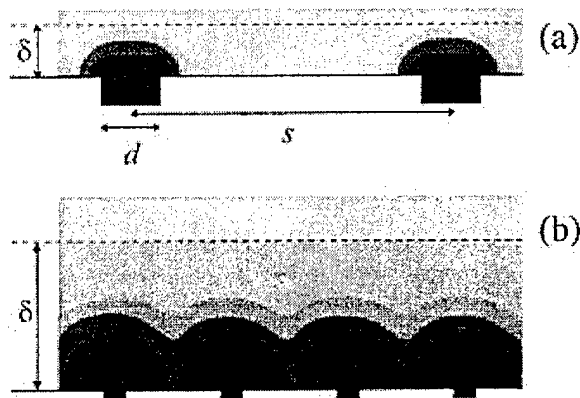

Figure 5. Schematic illustration of the growth and overlap of zones of elevated pH as a function of the cathode particle size, d and spacing s. δ is the thickness of the diffusion boundary layer. The shaded colors correspond to the shape and extent of the pH 9.5 zone as time evolves. (a) $d \sim \delta$, $s \gg \delta$, Particle separation is larger than the diffusion boundary layer thickness and zones of increasing pH are cut off by convection. Only the matrix immediately adjacent to the particles is exposed to a high enough pH for alkaline dissolution of Al. (b) $d \ll \delta$, $s \ll \delta$, Particle size and separation are smaller than the diffusion boundary layer thickness, the system behaves as a microelectrode array, causing the entire surface to activate to matrix dealloying.
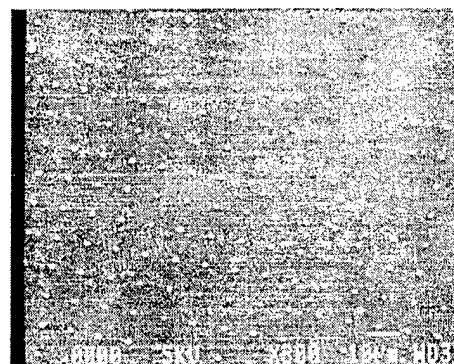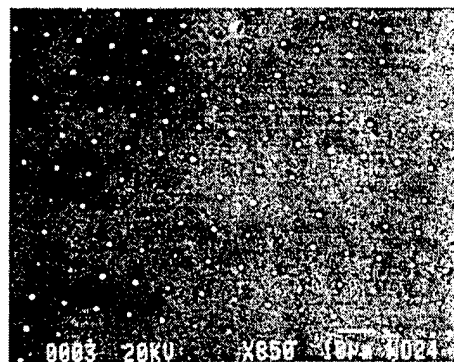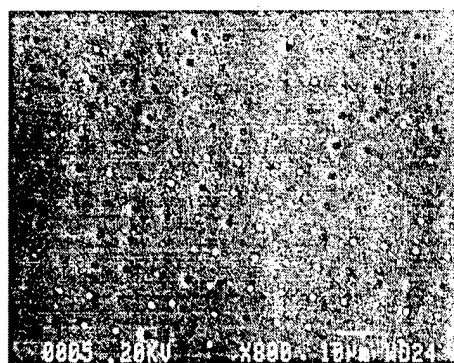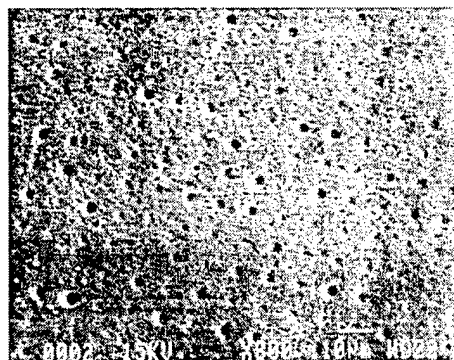

Figure 6. A time sequence of SEMs showing the morphology of a synthetic Al 2024 sample (1.8 μm Cu particles) after exposure to a 0.5 M NaCl solution.

sweep of the potential from the onset of hydrogen evolution at a sweep rate of 2 mV s^{-1}. A saturated calomel electrode (SCE) was used as reference electrode and Pt wire as a counter electrode. A standard RDE device (Pine Instruments) together with a Pine Instruments bipotentiostat (model AFRDE5) was used. Corrosion treatments (Al alloy 2024, Al-1 wt % Cu, synthetic 2024) at prescribed rotation rates and times were performed under free corrosion conditions in a 0.5 M NaCl solution. Afterward, the samples were taken out of the electrolyte, rinsed thoroughly with Barnstead Nanopure (>18 MΩ) water and transferred into another cell used for Cu assay using a lead underpotential deposition (Pb UPD) technique we previously developed.[15] Typically, following Cu assay by Pb UPD, the samples were examined using both scanning electron and optical microscopy.

RRDE studies.—RRDE studies were used to ascertain the operation of the Cu dissolution/back-plating mechanism. The same Pine device together with the same reference and counter electrode was used as described in the section on RDE studies. A silver collection ring (area 0.125 cm^2) maintained at −0.80 V (SCE) was used to capture copper cations during free corrosion of samples (Al 2024-T3, Al-1 wt % Cu matrix, or synthetic 2024) in 0.5 M NaCl solution. Silver was chosen as the ring material instead of platinum in order to avoid the complicated stripping of Cu from Pt owing to the UPD phenomena,[16] as well as to minimize the hydrogen evolution. Each experiment involved immersion of the sample disk at a prescribed rotation rate and time. After the corrosion treatment, the ring along with the holder were rinsed with Nanopure water and transferred into a new cell containing 0.01 M HClO$_4$, where a potential of −0.4 V (SCE) was immediately applied to the silver ring. In this cell the Ag ring served as the working electrode in a standard three-electrode configuration (SCE reference electrode, Pt counter electrode). After a steady-state current was attained, an anodic sweep was performed at a sweep rate of 20 mV s^{-1}. A positive anodic sweep limit of 0.2 V (SCE) was chosen in order to allow us to ascertain the onset of silver dissolution from the ring. The copper stripping wave typically appeared at potentials of 0.03-0.06 V (SCE). The advantage of introducing a second electrochemical cell was to avoid the formation of AgCl at potentials close to that of copper stripping.

All the solutions were made with high purity grade chemicals and Nanopure water. A BAS CV-27 model potentiostat was used for the analytical electrochemical experiments (Cu stripping from the Ag ring and Cu assay by Pb UPD) and a Nicolet 310 digital oscilloscope was used to store data. All glassware used for experimentation and the preparation of electrolytes was cleaned with concentrated HNO$_3$ and H$_2$SO$_4$ at 70°C, then rinsed using doubly distilled and Nanopure water.

Results and Discussion

Figure 7 shows results for the Cu content determined by Pb UPD assay on synthetic and real 2024 samples as a function of treatment time in 0.5 M NaCl at zero rotation rate. We note that the assay was accurate to within ±0.02 area fraction of surface coverage.[15] These results pose the major question addressed in this work, namely, what are the causes of the differences in the time-dependent surface coverage of Cu between the synthetic and the real alloy? The following is a list of the possible causes of this discrepancy.

Dissolution and back plating contribution: porous S-phase.—As discussed in the first part of this paper, a requirement of the dissolution and back-plating of copper redistribution is the mechanical/electrical detachment of copper particles. This allows the detached copper particle to adopt the corrosion potential of copper in the electrolyte leading to dissolution of copper and back-plating of Cu^{2+} ions from solution. There are many anodic processes available to support back-plating, including second-phase and/or matrix dealloying, matrix oxidation, and double-layer processes. One likely source of copper liberation from Al 2024-T3 that is unavailable to the synthetic alloy is dealloyed S-phase. In general, dealloying will not
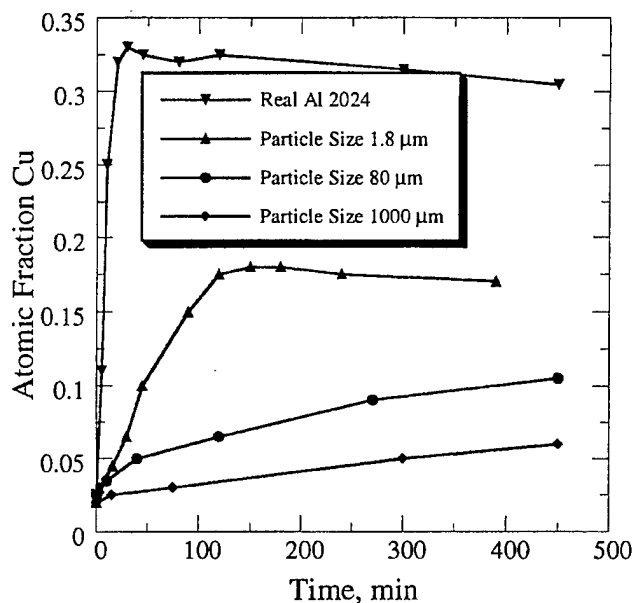

Figure 7. Cu surface coverage, determined by Pb UPD assay, on synthetic and real Al 2024 samples as a function of exposure time in 0.5 M NaCl.

always produce a mechanically stable bicontinuous structure. For example, consider the dealloying of a Ag$_{0.9}$Au$_{0.1}$ alloy. Since the Au atom fraction is below the 3-D site percolation threshold (corresponding to 20 atom % gold), the formation of a mechanically stable bicontinuous gold structure at this alloy composition is not possible. Instead, dealloying of silver produces 3-D gold clusters that become disconnected from the corroding substrate. The Al$_2$CuMg, S-phase, contains 25 atom % copper, and has an orthorhombic crystal structure. From a percolation point of view, this intermetallic is a borderline case in the sense of resulting in mechanically stable bicontinuous dealloyed structures. During S-phase dealloying, we cannot rule out the possibility that nanometer-scale ligaments of copper become disconnected from the Cu-rich porous sponge evolving during the dealloying process. As discussed below, another possible source of liberated copper for both the real and synthetic 2024 is matrix dealloying. In order to evaluate the relative contribution of these processes to copper redistribution, we performed RDE and RRDE studies.

Surface activation.—Figure 7 shows that as the particle spacing in the synthetic alloy gets smaller the amount of copper on the surface increases. As illustrated in Fig. 5, there are two length scales that determine the behavior of the synthetic alloys: one is the separation between the particles on the surface (at fixed area fraction this sets the particle diameter) and the other is the thickness of the diffusion boundary layer. The requirement for the entire surface to "activate" to oxygen reduction is that the Cu particles on the surface must behave collectively as a microelectrode array. This behavior occurs when the Cu dot separation in the synthetic alloy is much less than the diffusion boundary layer thickness. In this case, the oxygen diffusion-limited current density of the Cu microelectrode array is equal to that of a planar copper electrode. If the interparticle separation is too large, then the oxygen reduction current density is lowered, yielding corresponding reductions in the corrosion rate and subsequent copper accumulation on the surface of the synthetic alloy. We have examined these effects by RDE measurements of oxygen diffusion-limited current densities on all five of the samples described in the Experimental section. An obvious route to test the effects described above is to simply produce model alloys with smaller Cu dot separations, while maintaining a 0.03 area fraction of Cu on the surface. Unfortunately, the synthetic alloy with 1.8 μm Cu
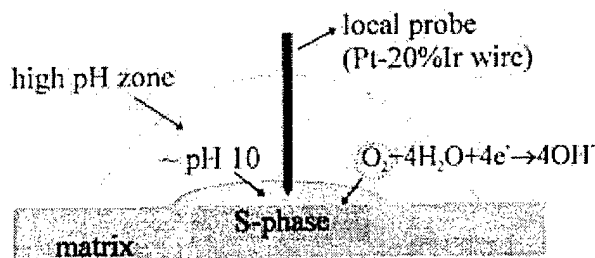
Figure 8. Schematic illustration of the local pH probe experiment.

dot diam already represents the order of magnitude limit of feature sizes and dimensions available via conventional lithography routes.

Copper in solid solution.—The synthetic alloy could contain less Cu in solid solution then the real Al 2024. In principle, the amount of Cu in solid solution can be examined via high resolution analytical transmission electron microscopy (TEM), however in practice these measurements are difficult. This hypothesis was examined in ancillary experiments, using synthetic alloys containing 4 wt % Cu in solid solution. These results are presented at the end of this paper.

Ancillary issues.—Prior to presenting the main body of our experimental results, it was necessary to consider three additional issues. The first issue concerned the behavior of the synthetic alloy vis-à-vis retention of the copper dots on the surface, during immersion in the chloride electrolyte.

Figure 6 shows a time sequence of scanning electron micrographs (SEMs) of the surface of the synthetic alloy following immersion under free corrosion in the chloride electrolyte. For immersion times of order a few hours, there is little damage to the surface and the array of Cu particles stays intact. While periphery grooving around the copper dots is apparent in samples that were immersed for times of order 7 h or more, close inspection reveals that each of the "pits" retains a copper dot at the bottom. We would expect the copper dots to be undercut eventually by corrosion. Figure 7 shows that the relevant time scale to achieve maximum copper surface coverage in a stagnant electrolyte is of the order of 100 min, and over these time scales, the synthetic alloys retain integrity.

Another issue relates to the steady-state pH that evolves within the diffusion boundary layer during corrosion of Al 2024-T3 in a nominally neutral electrolyte. In order for the matrix dealloying mechanism to operate, the pH in the diffusion boundary layer should be greater than ~8.0 for aluminum to dissolve via the soluble AlO_2^- species.[17] We measured the local pH in the vicinity of S-phase particles on the surface of Al alloy 2024-T3 by using the tip of a scanning tunneling microscope (STM) as an *in situ* local pH probe as illustrated in Fig. 8. A 99.5% pure Johnson-Matthey Pt-20% Ir wire (0.25 mm diam) was used as a working electrode and a Pt wire (1 mm diam) served as the counter electrode. In all the experiments, the potential was measured *vs.* SCE. Calibration solutions were made using 0.1 M NaCl + *x* M NaOH where *x* was chosen to provide us with pH 6.5, 7.5, 8.5, 9.0, 10.0, 10.5, 11.2, and 12.8. The pH of 0.1 M NaCl (*x* = 0) was 5.3. In these experiments, the potential was swept from 300 to 1500 mV (SCE) at a sweep rate of 20 mV s^{-1}.

Figure 9 represents the current-voltage (I-V) behavior of a Pt-20% Ir wire in 0.1 M NaCl + *x* M NaOH. The first curve where no NaOH was added (pH 5.3) demonstrates a flat double layer region with the onset and further development of an oxygen evolution process. All other curves reveal a current peak at potentials negative to the potential of the oxygen evolution process. Similar peaks obtained on polycrystalline and monocrystalline platinum electrodes in alkaline solution by others[18] have been related to oxygen adsorption that precedes the oxygen evolution. The peak current densities in Fig. 9 are plotted *vs.* pH in Fig. 10. A simple linear regression
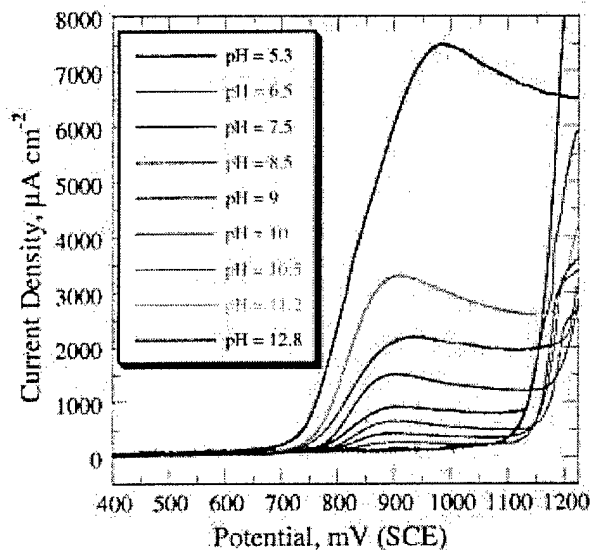

Figure 9. I-V behavior of a Pt-20% Ir microelectrode in 0.5 M NaCl + *x* M NaOH. Sweep rate, 20 mV s^{-1}.

analysis was used to fit the data that served as a standard for the *in situ* STM measurements.

In situ STM measurements over and immediately adjacent to S-phase particles in the surface of Al alloy 2024-T3 immersed in a neutral chloride electrolyte revealed that the pH tended toward a steady-state value of ~9.5 within 20 min of immersion.

The third issue is concerned with the role of second phase particles (*e.g.*, FeMnCuAl, Al$_2$Cu, etc.) other than the S-phase in serving as a source of redistributed copper in real 2024-T3. In ancillary studies, Ford *et al.*[19] used analytical TEM to characterize the 2024-T3 material used in this study following corrosion treatments in a neutral chloride solution in order to determine the reactivity (*i.e.*, the ability of the particle to serve as a source of redistributed Cu) of the S-phase and other constituent particles such as those
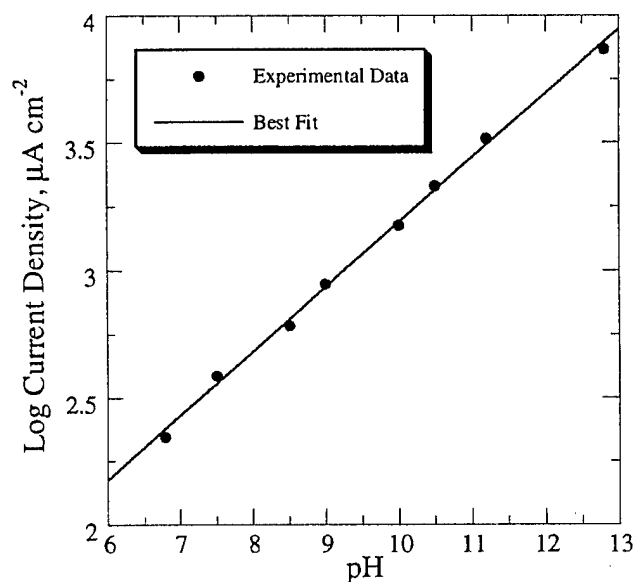

Figure 10. Peak current density of a Pt-20% Ir microelectrode in 0.5 M NaCl + *x* M MNaOH as a function of pH.
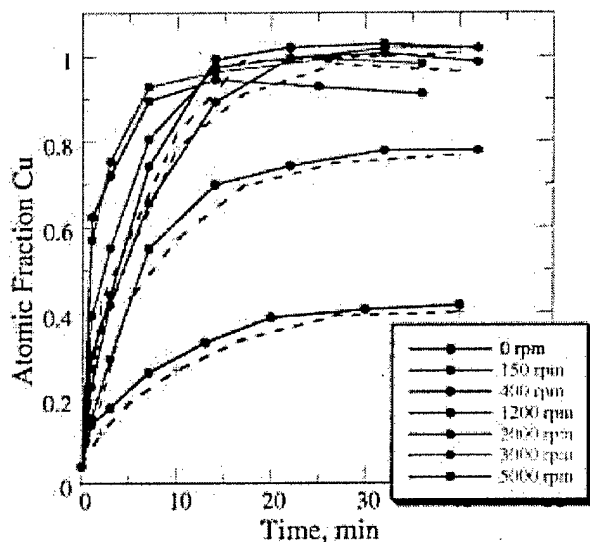
Figure 11. Cu surface coverage (Pb UPD assay) on real Al 2024-T3 after free corrosion in 0.5 M NaCl as a function of exposure time at the indicated rotation rates.

containing FeMnCuAl. They found that the S-phase dealloyed and that FeMnCuAl dispersoids were stable. Phases such as Al$_2$Cu, even if dealloyed will produce a copper-rich remnant that would remain mechanically intact since the copper content is well above the percolation threshold (see the Results and Discussion section on dissolution and back-plating contribution: porous S-phase). Mazurkiewicz and Piotrowski[20] examined the behavior of monolithic Al$_2$Cu in 0.5 M SO$_4^{2-}$ electrolyte in an RRDE configuration. By observing color change, they reported large quantities of Cu captured on the ring indicating the operation of a Cu back-plating mechanism. The implication is that the Al$_2$Cu phase may be an important source of redistributed copper in Al-Cu alloys. Our own RDE and RRDE results presented next in the sections on RDE studies, and RRDE studies: copper redistribution contradict this conclusion.[d] Therefore, we consider the S-phase as the only particle constituent phase that could serve as a significant source of redistributed copper.

RDE studies.—Figure 11 shows results for copper accumulation on the surface of Al 2024-T3 as a function of free corrosion immersion time (0.5 M NaCl) and rotation rate. The data joined by solid lines were obtained by using the same sample for a prescribed time and rotation rate. Following copper assay by Pb UPD, the sample was washed using procedures described in the Experimental section and was directly reimmersed at the same rotation rate. The time axis represents cumulative exposure times for this data set. The data set joined by dashed lines were obtained from samples that were immersed for a prescribed time and rotation rate, subjected to copper assay by Pb UPD and repolished using procedures described in the Experimental section. The time axis represents total exposure times for this data set. The results for copper accumulation are insensitive to the details of the methods used to obtain the data sets. The results indicate that for immersion times less than about 10 min the accumulated copper increases with rotation rate. For immersion times greater than about 10 min the accumulated copper increases with rotation rate in the range of zero to 400 rpm and then either saturates or shows a slight decrease. The coverage saturates at an equivalent monolayer of copper on the surface.

The general effect of rotation rate on copper coverage is easily understood. Since the thickness of the diffusion boundary layer decreases as the reciprocal of the square root of rotation rate, the oxygen diffusion-limited current density increases. Thus, the corrosion rate of the sample increases with rotation rate and we can expect the surface copper coverage to increase accordingly.

Figure 12 shows optical micrographs of the Al 2024-T3 surface following 60 min of free corrosion in the 0.5 M NaCl electrolyte at the indicated rotation rates. In the stagnant electrolyte, the vast majority of corrosion damage is localized in the vicinity of S-phase intermetallic particles imbedded in the alloy matrix. Since the corrosion rate increases with increasing rotation rate, the corrosion damage should increase accordingly. We observe this behavior up to rotation rates of about 400 rpm where qualitatively the corrosion damage is a maximum as accessed by the overall degree attack on the alloy matrix between the particles. At higher rotation rates, the corrosion damage begins to localize around the particles and at 5000 rpm the damage is mainly confined to the region immediately surrounding the particle. This behavior is a result of two competing effects associated with the increased rotation rate or decreasing diffusion boundary layer thickness. As the diffusion boundary layer decreases, the oxygen diffusion-limited current density increases, as does the corrosion rate. Eventually, as the rotation rate increases, the diffusion boundary layer thickness gets to be of order the size of the cathode (particle) separation on the surface of the alloy. The hemispherical regions of oxygen diffusion (which mirror the zones of increasing pH) are thus terminated. As a result, the cathodic current density is reduced below the mass-transport limited rate. Concurrently, the hemispheres of increasing pH, emanating from the particles (see Fig. 4), are cut off by convective flow and the matrix regions separating the particles never achieve the high pH required for matrix dissolution. Owing to these competing effects, beyond a certain rotation rate, the area fraction of the surface that shows significant dissolution or corrosion damage decreases with increasing rotation rate. Thus we expect to see the maximum corrosion damage in the matrix, between the particles active to oxygen reduction, at some intermediate rotation rate. The rotation rate corresponds to a diffusion boundary layer thickness defining an average separation between active particles in Al 2024-T3. Application of the Levich equation indicates that this length scale is of order 10-20 μm. In comparing conclusions based on the results presented in Fig. 11 and 12, there is an unresolved issue. Namely, why is it that the copper accumulation increases with increasing rotation rate, while the surface corrosion damage saturates in the vicinity of 400 revolutions per minute (rpm)? We return to this question in a later section of this paper.

Figure 13 shows results for copper accumulation on the surface of the synthetic 2024 alloy (9.5 μm Cu dot spacing) as a function of free corrosion immersion time and rotation rate. The time-dependent, accumulated copper is independent of rotation speed up to 200 rpm and then decreases with increasing rotation speed. This behavior is a direct consequence of our previous discussion regarding Fig. 12. At 1500 rpm, the diffusion boundary layer thickness is about 13 μm, which is close enough to the interdot distance so that the zones of increasing pH are cut off by convection. Under identical conditions, the area fraction of accumulated copper on the surface of the synthetic 2024 alloy is consistently lower than that observed on the real 2024. We note that if phases such as Al$_2$Cu (which likely exist in both the synthetic and real 2024) were important in the copper redistribution process, then the results presented in Fig. 11 and 13 would have been quantitatively similar. Figure 14 shows optical micrographs of the synthetic 2024 following 60 min of free corrosion in the 0.5 M NaCl electrolyte at the indicated rotation rates. In general, one observes that the corrosion becomes more localized with increasing rotation rate.

RRDE studies: copper redistribution.—The results presented above demonstrated an influence of the rotation rate on the copper redistribution process. RRDE experiments were performed in order
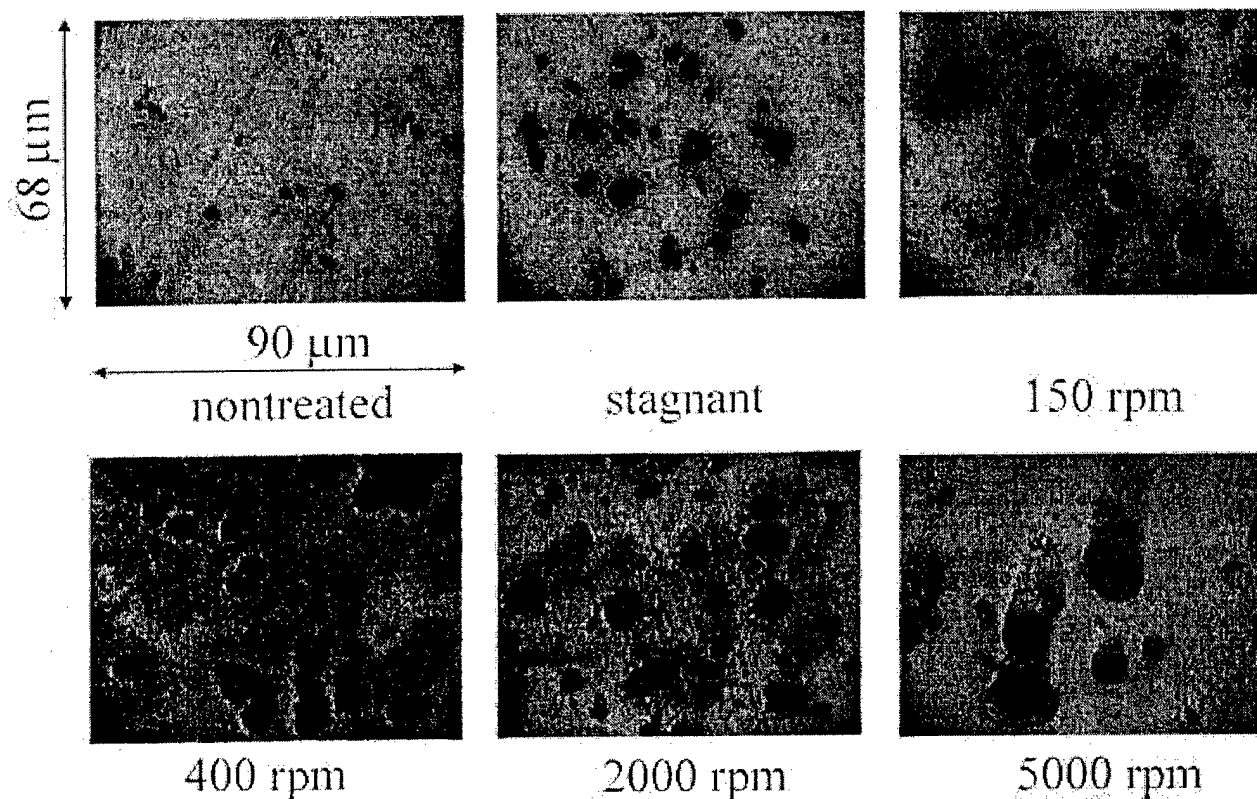
---

[d] We suspect that their results were affected significantly by the manner in which the Al$_2$Cu disk was embedded into an insulator resulting in large compressive radial stresses that caused the remnant porous Cu to break apart during dealloying of Al.

Figure 12. Optical micrographs of real Al 2024 samples after treatment in 0.5 M NaCl for 60 min at the indicated rotation rates.

to determine if the Cu dissolution and back-plating mechanism is operative in the Cu redistribution process. In order to ascertain this, a fixed potential was maintained on the silver ring that was more negative than the corrosion potential of the Al matrix. The applied potential allowed the silver ring to enter into competition with the Al matrix in the Cu back-plating process. A relatively long corrosion
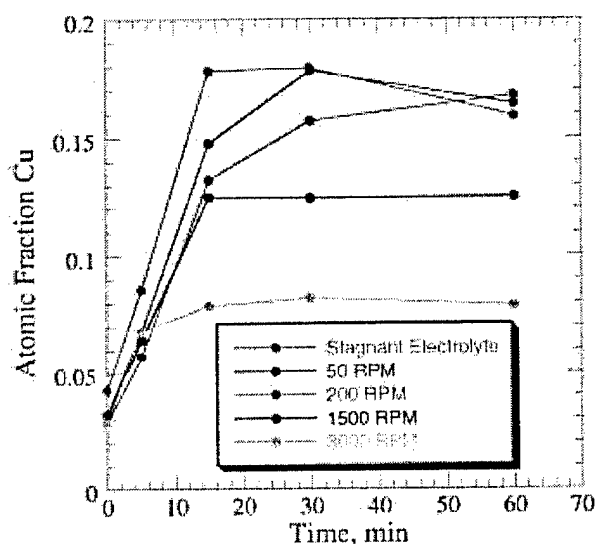
time (90 min) was chosen in order to insure that if there were any Cu^{2+} ions in solution a detectable amount would be deposited on the Ag ring. A back of the envelope estimate shows that at least 50 equivalent monolayers of Al should be dissolved from the synthetic 2024-T3 in order to register one Cu monolayer on the ring surface.

Figure 15 shows results of Ag-ring anodic stripping waves obtained in 0.01 M $HClO_4$ following open circuit exposure of a pure copper disk and Al alloy 2024-T3 disk in 0.5 M NaCl at 1000 rpm. The I-V behavior of a bulk polycrystalline copper electrode is also shown. A comparison of these curves allowed us to conclude that the stripping wave associated with corrosion of the Al 2024-T3 resulted from copper dissolution. The charge associated with the stripping wave of the Al 2024-T3 was about 2% of that obtained from the pure Cu disk. Figure 16 is a set of copper stripping curves from the Ag ring (obtained in 0.01 M $HClO_4$ electrolyte) after free corrosion of Al 2024-T3 and Al-1 wt % Cu (matrix) disks in 0.5 M NaCl for 90 min. The amount of copper captured on the silver ring during corrosion of both the Al 2024-T3 and Al-1 wt % Cu matrix samples in a stagnant 0.5 M NaCl electrolyte was within the detection limits of the technique. Similar results were obtained by Buchheit *et al.*[21] using a Pt ring. The amount of Cu captured by the Ag ring was found to be a strong function of rotation rate. Figure 17 obtained by integration of the stripping waves of Fig. 16 shows an almost linear increase of the captured copper in the range of 1000-2500 rpm region. Identical results to those obtained for the Al-1 wt % Cu matrix disks were also obtained for the synthetic alloys, reaffirming that the only source of Cu available for redistribution from the synthetic alloy is copper in solid solution. These results demonstrate that the S-phase on the surface of Al 2024-T3 is an important source of redistributed copper via the dissolution and back-plating mechanism. The Al-1 wt % Cu matrix disks emitted relatively modest amounts of copper into the chloride electrolyte. Figures 18 and 19 show the Cu stripping waves as a function of time at 1500 rpm and
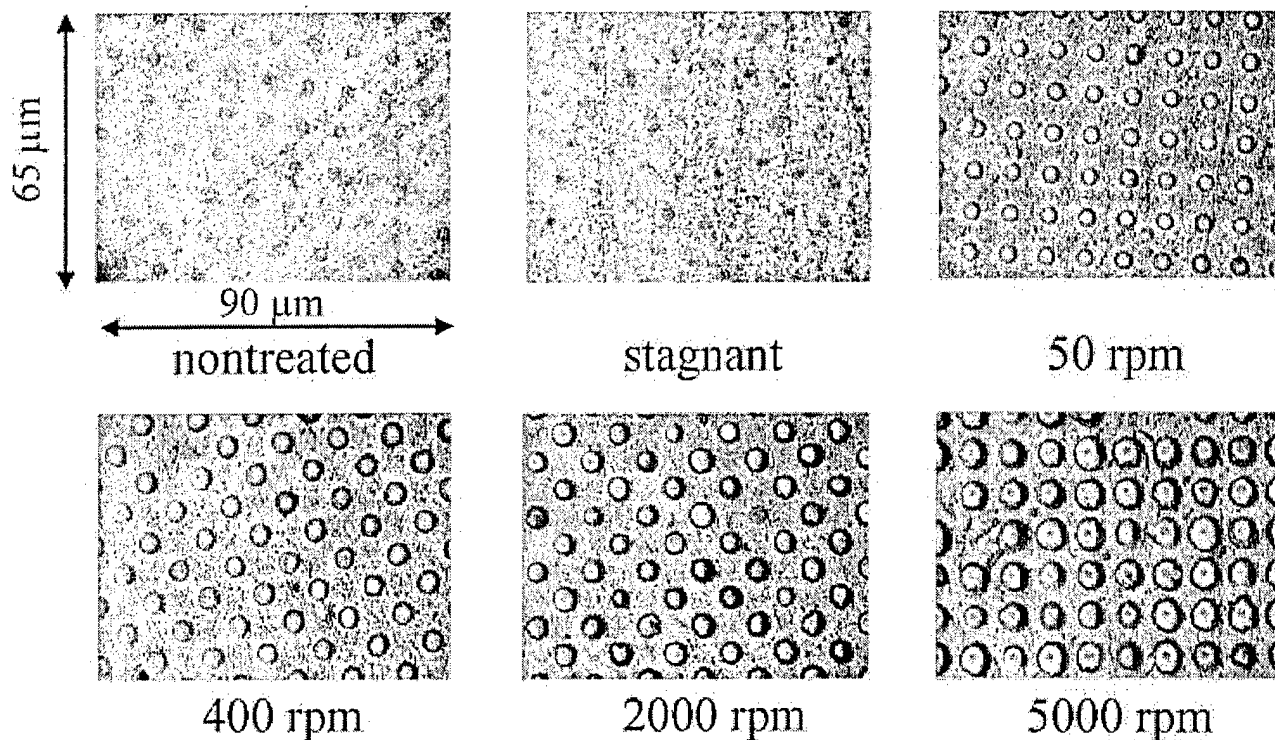

Figure 13. Cu surface coverage (Pb UPD assay) on synthetic Al 2024 samples following free corrosion in 0.5 M NaCl as a function of exposure time at the indicated rotation rates.

Figure 14. Optical micrographs of synthetic Al 2024 samples after free corrosion in 0.5 M NaCl for 60 min at indicated rotation rates.

Fig. 20 summarizes these results after integration of the stripping waves. Note, that for the real 2024, copper is present on the ring almost immediately, whereas it takes about 60 min for a detectable quantity to appear for the Al-1 wt % Cu-matrix samples or the synthetic alloy. The RRDE results (Fig. 16-20) are consistent with the RDE results in that if phases such as Al_2Cu were important to

the copper redistribution process, the results for the matrix alloy, the synthetic 2024, and the real 2024 would have been quantitatively similar.

RDE studies: oxygen diffusion limited current densities.—Regardless of the operative copper distribution mechanisms, intermetallic particles serve as the primary sites for oxygen
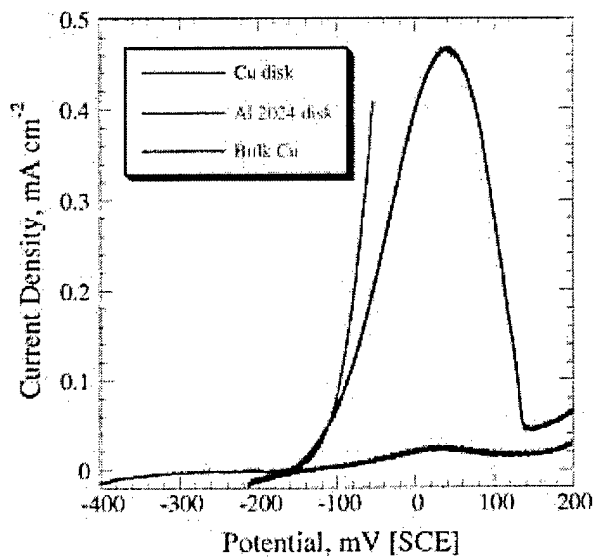
Figure 15. Copper stripping waves obtained from the Ag ring in a 0.01 M $HClO_4$ solution. Copper on the Ag ring accumulated from free corrosion of a pure copper disk and a real Al 2024 disk at 1000 rpm in 0.5 M NaCl. The I-V behavior of a bulk copper electrode in a 0.01 M $HClO_4$ solution is shown for comparison.
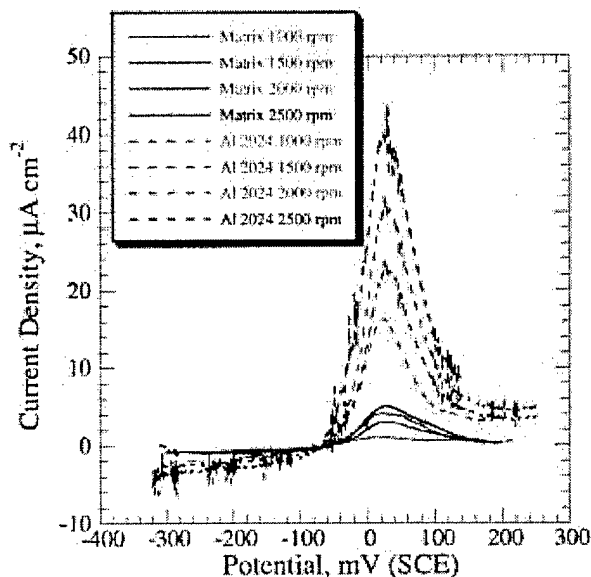

Figure 16. Copper stripping curves from a silver ring after free corrosion of real 2024 and matrix samples for 90 min in 0.5 M NaCl at the indicated rotation rates.
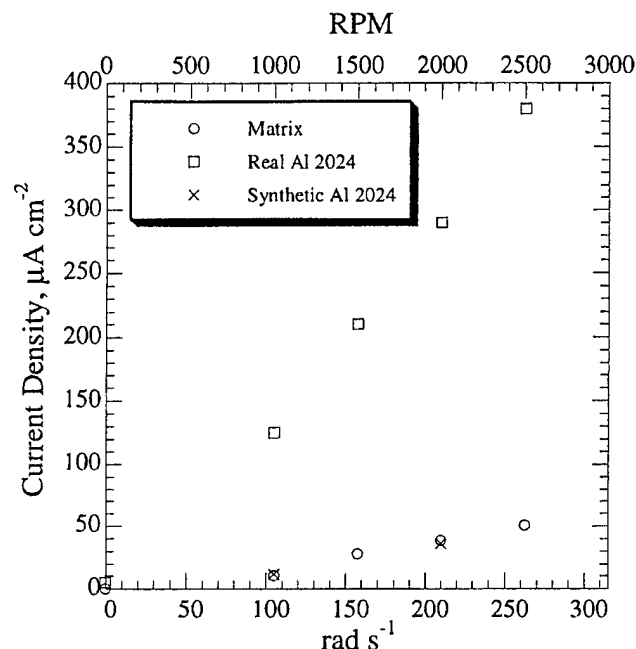
Figure 17. Current densities of copper stripped from the Ag ring in 0.01 M $HClO_4$ solution after 90 min of free corrosion in 0.5 M NaCl of matrix, synthetic, and real Al 2024 samples as a function of rotation rate.

Figure 19. Copper stripping curves from a silver ring after free corrosion of matrix samples in 0.5 M NaCl for different times at 1500 rpm.

reduction on a corroding Al 2024-T3 surface. In this regard, we assume that dealloyed S-phase particles are most important. However, our major conclusions are unaffected by contributions from other types of particles.[22,23] The oxygen reduction rate balances the rate at which any anodic process related to copper redistribution operates. Therefore, this parameter must be well characterized if one is to develop a quantitative model of corrosion and copper redistribution in Al-Cu-X alloys. Furthermore, RDE measurements of oxygen diffusion-limited current densities allow us to determine if the synthetic alloy geometry (1.8 μm diam Cu disks in a square array with 9.5 μm near-neighbor spacing) is behaving as an array of mi-

croelectrodes. For example, at low enough rotation rates, the oxygen diffusion limited current density of CEI samples should be identical to that of a planar Cu electrode. We note that since both anodic and cathodic processes are operative in the synthetic 2024, the net cathodic current density will be less than that of the CEI or planar Cu samples.

In a conventional four-electron reduction mechanism, under aerated conditions, the oxygen diffusion-limited current density in a stagnant electrolyte is a poorly defined quantity in the range of 20-100 μA cm^{-2}. Additionally, recent studies in our laboratory demonstrate that the magnitude of the oxygen diffusion-limited current density on planar copper electrodes is not a function of electrolyte pH.[24] We found that measurements in pH 1.5-14 electrolytes yielded values between 20 and 30 μA cm^{-2}. In these electrolytes, at a po-
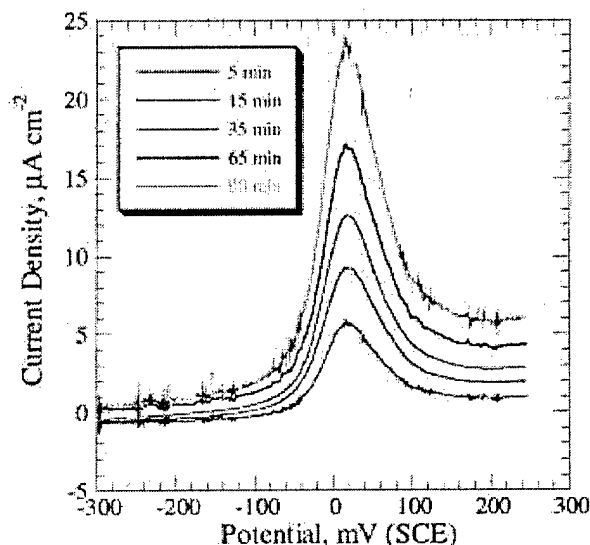

Figure 18. Copper stripping curves from a silver ring after free corrosion of real Al 2024 samples in 0.5 M NaCl for different times at 1500 rpm.
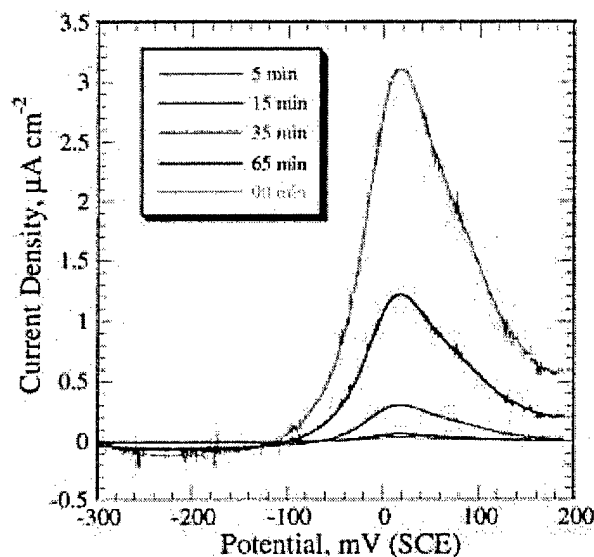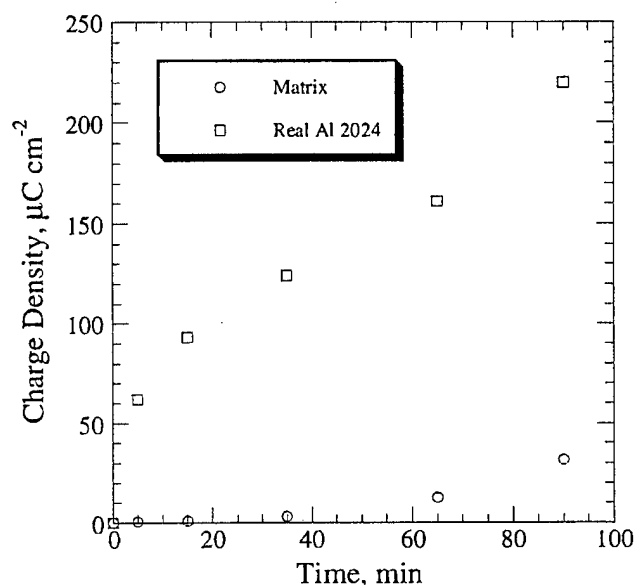

Figure 20. Charge densities as a function of time of stripped copper from the silver ring in 0.01 M $HClO_4$ solution after free corrosion of matrix and real Al 2024 samples in 0.5 M NaCl solution at 1500 rpm.
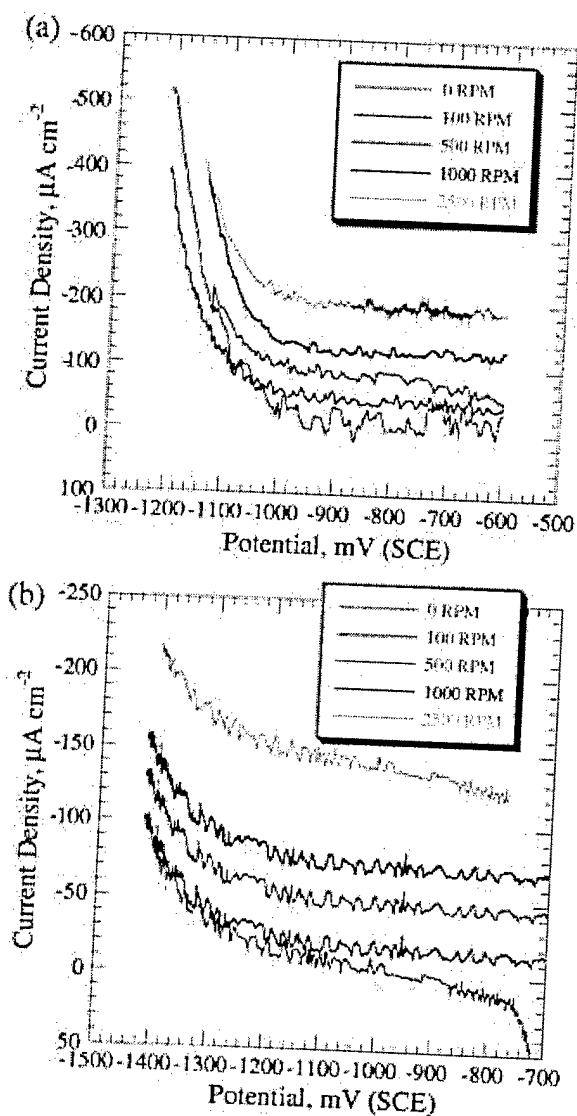
Figure 21. Polarization curves of (a) real and (b) synthetic Al 2024 in 0.1 M Na_2SO_4 at the indicated rotation rates. The approximately potential independent current densities correspond to oxygen reduction. The current density rises at larger negative potentials owing to hydrogen evolution.
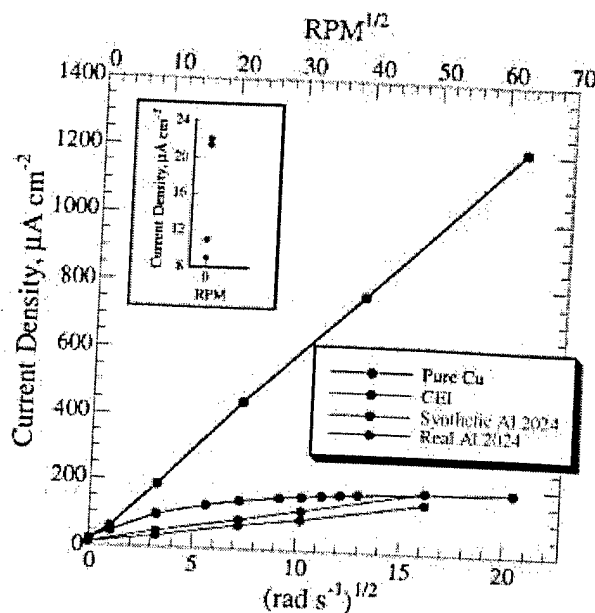

Figure 22. Oxygen diffusion-limited current densities of pure copper, CEI, real, and synthetic Al 2024 in 0.1 M Na_2SO_4 as a function of rotation rate. The inset shows the current densities in the stagnant electrolyte.

tential corresponding to the corrosion potential of Al 2024-T3, the copper surface is not film free (*e.g.*, there is an underpotentially deposited oxygen layer on Cu)[25] however, interestingly enough, the oxygen reduction kinetics are still purely mass-transport limited.[24]

Figure 21 shows representative polarization behavior demonstrating oxygen diffusion-limited current densities on real and synthetic 2024 in 0.1 M Na_2SO_4. Figure 22 shows that the oxygen diffusion-limited current densities scale linearly with the square root of the rotation rate. Each of the experimental points in Fig. 22 represent values averaged over four separate experiments. The general behavior fits the Levich equation, $i_L = 0.62nFD^{2/3}\nu^{-1/6}c_\infty\omega^{1/2}$, where i_L is the limiting current density, F is Faraday's constant, n is the number of electrons, D is the diffusion coefficient in the range of 0.5-1.7×10^{-5} cm^2 s^{-1}, ν is the kinematic viscosity equal to 10^{-2} cm^2 s^{-1}, ω is the disk rotation rate (rad s^{-1}), and c_∞ is the concentration of oxygen in the bulk solution, in the range of 1.7-2.7×10^{-7} mol cm^{-3}. The slopes of the lines marked real and synthetic are 10.5×10^{-6} and 8.6×10^{-6}

A s$^{1/2}$/rad$^{1/2}$ cm^2, respectively, which is about a factor of four to ten less than the predicted range in slope of 40-80 $\times 10^{-6}$ A s$^{1/2}$/rad$^{1/2}$ cm^2. The diffusion-limited current density measured on real 2024 alloys is higher than that obtained on the synthetic 2024 samples, which is in accord with the results of the section on RDE studies related to copper surface coverage.

Figure 22 also summarizes our results for the oxygen diffusion-limited current density in 0.1 M Na_2SO_4 as a function of rotation rate for all the samples examined. The inset shows that in a stagnant electrolyte, the CEI sample geometry (1.8 μm diam Cu disks in a square array with 9.5 μm near-neighbor spacing) and a planar Cu electrode gave similar results demonstrating that the CEI sample behaved as a microelectrode array for oxygen reduction. The slope of the line corresponding to the behavior of the planar copper electrode is in accord with the prediction of the Levich equation and the range of parameter values indicated above.

Note that all the samples except the CEI samples fit the general form, $i_L \propto \omega^{1/2}$. In the case of real and synthetic 2024 alloys this behavior is observed despite the fact that the limiting current is a sum of partial currents resulting from oxygen reduction and anodic dissolution/oxidation processes. We surmise that this overall behavior could result only if two conditions are met. The first is that there is mass transport control of the rate of the anodic process. The second is that the real and synthetic 2024 samples have cathodic particles on the surface at length scales much smaller than the nominal 9.5 μm microelectrode array length scale of the synthetic 2024. Otherwise, behavior of the synthetic alloy would be similar to that of the CEI sample. While the real 2024 may have variously sized particles distributed at many length scales, the only way for this to happen in the synthetic 2024 is via copper accumulation through matrix dealloying. Copper enriches on the surface by dealloying of Al from the matrix and then by surface diffusion; very small (*ca.* 100 nm) Cu atoms agglomerate into nanometer-size clusters.[26,27] These small Cu clusters are active for oxygen reduction. Similar processes occur on the surface of real 2024 during corrosion and this is responsible for the often-observed copper color on the surface of the corroded alloy.
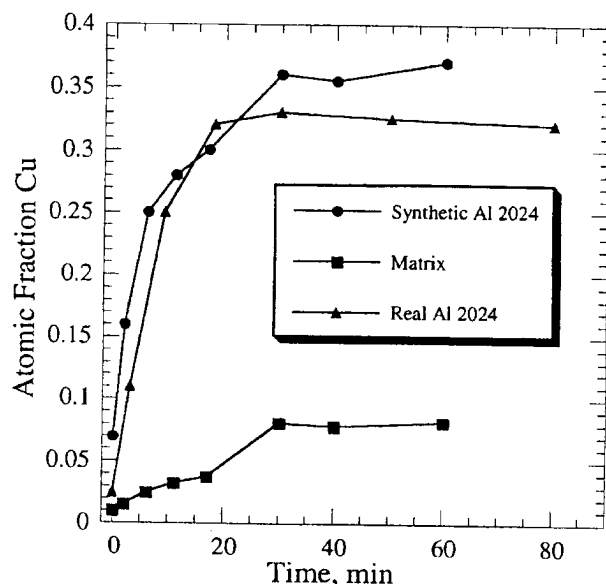
Figure 23. Cu surface coverage (Pb UPD assay) on real, synthetic Al 2024 (made using a 4 wt % Cu matrix), and a 4 wt % Cu matrix sample as a function of exposure time in 0.5 M NaCl.

The CEI sample shows distinctly different behavior. In general, for a microelectrode array, the limiting current will follow, $i_L = [f(\omega)] \cdot [i_{L,\text{planar electrode}}(\omega)]$, where $f(\omega)$ is a rotation rate-dependent shape function defining the volume fraction per unit time of the diffusion boundary layer supplying oxygen for the reduction process. The shape function equals 1.0 in the limit of low rotation rates and then decreases with increasing rotation rate. Shape function effects are apparent in the optical micrographs (Fig. 12 and 14) of the corroded real and synthetic alloys.

Conclusions

The first issue (of the questions and issues posed by the results presented in Fig. 6) that we address is that of "surface activation" of the synthetic alloy (Al-1 wt % Cu) composed of 1.8 μm diam Cu disks in a square array with 9.5 μm near-neighbor spacing. Our studies of the oxygen diffusion-limited current density demonstrate that this geometry behaves as a microelectrode array in the limit of a stagnant or very weakly stirred electrolyte. Under this constraint, the microelectrode array provides the same oxygen diffusion-limited current density as a planar Cu electrode. Thus, in a stagnant electrolyte, this synthetic 2024 alloy is as efficient as the real 2024 for oxygen reduction.

Our RRDE results and those of Buchheit *et al.*,[21] demonstrate the operation of a dissolution/back-plating copper redistribution mechanism during corrosion of Al 2024-T3. This process is triggered by very small copper particles of order tens of nanometers in size that become mechanically disconnected from dealloyed S-phase intermetallic particles. As long as the remnant dealloyed copper sponge stays mechanically and electrically connected to the substrate, no copper dissolution can take place. In this case, we can disregard particle size effects on dissolution since the corrosion potential is almost 1 V less than the reversible potential of copper.[10,27]

The RDE studies of the oxygen diffusion-limited current density demonstrate that the synthetic 2024 (1.8 μm diam Cu disks in a square array with 9.5 μm near-neighbor spacing) geometry behaves as a microelectrode array for oxygen reduction. Furthermore Fig. 22 shows that independent of rotation rate, oxygen reduction on the surface of the real and synthetic alloys is quantitatively similar. During immersion of these alloys in 0.5 M NaCl, the only physical process that we can identify taking place on the surface of the real

2024 that does not occur on the synthetic 2024 is the operation of the dissolution/back-plating mechanism of copper redistribution.

We address the final point relating to the amount of copper in solid solution in the real and synthetic 2024. Since Al 2024-T3 is naturally aged, no single well-defined number can characterize the level of copper in solid solution. A large fraction of the ~4 wt % Cu in this alloy eventually is taken up by coherent or incoherent second phases. As noted earlier, the literature indicates that a reasonable value for the copper in solid solution is 0.2-0.5 wt %.[5] Thus, we believe that our synthetic alloy is a reasonable model in this regard. However, it is easily demonstrated as shown in Fig. 23, that as the copper content in solid solution of a synthetic alloy increases to 4 wt % the redistributed copper on the surface of the synthetic alloy closely approximates the behavior of the real 2024. In this case, the matrix dealloying mechanism alone is sufficient to quantitatively account for the copper redistribution process. On-going work in our laboratory using quantitative analytical high resolution TEM is aimed at ascertaining the amount of copper in solid solution of the Al 2024-T3 alloys that we have been using. To date, we find that the amount of Cu in solid solution is spatially heterogeneous and ranges from just below 1 to 4 wt % and so presently we cannot make any definitive conclusions on this issue.[28]

Finally, the differences in behavior for the surface coverage of Cu between 2024-T3 and the synthetic 2024 alloy is attributed to the operation of a dissolution/back-plating mechanism triggered by mechanical disconnection of Cu particles from dealloyed porous S-phase. Comparisons of the behavior of these two alloys allow us to conclude that the matrix dealloying and dissolution/back-plating contribute about equally to the copper redistribution process during corrosion of aluminum alloy 2024-T3 in 0.5 M NaCl.

References

1. R. G. Buchheit, R. P. Grant, P. F. Hlava, B. Mckenzie, and G. L. Zender, *J. Electrochem. Soc.*, **144**, 2621 (1997).
2. T. J. Warner, M. P. Schmidt, F. Sommer, and D. Bellot, *Z. Metallkd.*, **86**, 494 (1995).
3. G. S. Chen, M. Gao, and R. P. Wei, *Corrosion (Houston)*, **52**, 8 (1996).
4. M. Gao, C. R. Feng, and R. P. Wei, *Metall. Mater. Trans. A*, **29**, 1145 (1998).
5. L. F. Mondolfo, *Aluminum Alloys: Structure and Properties*, p. 254, Butterworth Markham, Ontario, CN (1976).
6. P. L. Hagans and C. M. Haas, *Surf. Interface Anal.*, **21**, 65 (1994).
7. R. M. Rynders, C. Paik, R. Ke, and R. C. Alkire, *J. Electrochem. Soc.*, **141**, 1439 (1994).
8. M. A. Alodan and W. H. Smyrl, *J. Electrochem. Soc.*, **145**, 1571 (1998).
9. T. Suter and R. C. Alkire, *J. Electrochem. Soc.*, **148**, B36 (2001).
10. N. Dimitrov, J. A. Mann, M. B. Vukmirovic, and K. Sieradzki, *J. Electrochem. Soc.*, **147**, 3283 (2000).
11. Z. Szklarska-Smialowska, *Corros. Sci.*, **41**, 1743 (1999).
12. Multiuniversity Research Institute Report to the Air Force Office of Scientific Research, Arizona State University (Aug 1998).
13. J. O. Park, C. H. Paik, Y. H. Huang, and R. C. Alkire, *J. Electrochem. Soc.*, **146**, 517 (1999).
14. M. B. Vukmirovic, Ph.D. Dissertation, Arizona State University, Tempe, AZ, 2001, In preparation.
15. N. Dimitrov, J. A. Mann, and K. Sieradzki, *J. Electrochem. Soc.*, **146**, 98 (1999).
16. R. Gómez, H. S. Yee, G. M. Bommarito, J. M. Feliu, and H. D. Abruña, *Surf. Sci.*, **335**, 101 (1995).
17. M. Pourbaix, *Atlas of Electrochemical Equilibria in Aqueous Solutions*, NACE (1974).
18. N. Furuya and M. Shibata, *J. Electroanal. Chem.*, **467**, 85 (1999).
19. R. G. Ford, R. W. Carpenter, and K. Sieradzki, *Microsc. Microanal.*, **4**, Suppl. 2, 754 (1998).

20. B. Mazurkiewicz and A. Piotrowski, *Corros. Sci.*, **23**, 697 (1983).
21. R. G. Buchheit, M. A. Martinez, and L. P. Montes, *J. Electrochem. Soc.*, **147**, 119 (2000).
22. A. J. Aldykewicz, H. S. Isaacs, and A. J. Davenport, *J. Electrochem. Soc.*, **142**, 3342 (1995).
23. G. O. Ilevbare and J. R. Scully, *J. Electrochem. Soc.*, **148**, B196 (2001).
24. M. B. Vukmirovic, N. Dimitrov, and K. Sieradzki, Unpublished work.
25. V. Maurice, H.-H. Strehblow, and P. Marcus, *Surf. Sci.*, **458**, 185 (2000).
26. J. Erlebacher, M. J. Aziz, A. Karma, N. Dimitrov, and K. Sieradzki, *Nature (London)*, **410**, 450 (2001).
27. K. Sieradzki, *J. Electrochem. Soc.*, **140**, 2868 (1993).
28. R. W. Carpenter, Private communication.

The Diffusion – Limited Current Density of Oxygen Reduction on Copper

M. B.Vukmirovic[1], N. Vasiljevic[1], N. Dimitrov[2], and K. Sieradzki[1,2]

[1]Program in The Science and Engineering of Materials
[2]Department of Mechanical and Aerospace Engineering, and
Department of Chemical Engineering and Materials Science
Arizona State University, Tempe, AZ 85287-6106

Abstract

There are many important processes in corrosion for which the diffusion –limited current density of oxygen reduction, i_L, plays a dominant role in terms of kinetic control. The conventionally believed magnitude of i_L (for the four-electron reduction mechanism) which can be found in many corrosion textbooks is in the range of 50 – 100 μA cm^{-2}, but the origins of this range of values are a bit mysterious. Previous research in our group aimed at ascertaining i_L (under stagnant conditions) on a planar Cu electrode and a Cu microelectrode array in a naturally aerated 0.1M Na_2SO_4 electrolyte found that i_L was in the range of 20 – 30 μA cm^{-2}. Obvious reasons for this discrepancy may involve a two – electron mechanism in the reduction or the presence of a surface film (an oxide) that retards the kinetics of the diffusion – limited reduction process. The work reported on herein was aimed at sorting out these issues. In situ STM was used to characterize the Cu surface at relevant potentials. RDE studies were used to measure i_L in a naturally aerated 0.1M Na_2SO_4 electrolyte as a function pH for both Pt and Cu electrodes. By comparing results for Pt and Cu we conclude that oxygen reduction occurs on a Cu surface via the four - electron mechanism. We found that while there is an underpotentially deposited oxygen adlayer on the Cu surface for pH values of ~ 9.5, this had no effect on i_L. The

oxygen diffusion – limited current density was found to be independent of pH (in the range 1.5 – 14). Finally, we conclude that our previous determination of i_L in a stagnant electrolyte actually reflect an accurate range of values of the oxygen diffusion – limited current density.

Introduction

Oxygen reduction is important in corrosion since the kinetics of this process often determines general corrosion rates and damage evolution (e.g., pitting, crevice corrosion, stress –corrosion, corrosion fatigue) in a number of commercially important alloys. Nevertheless, as briefly discussed below, there have been relatively few well – conceived experiments aimed at measuring the rate of oxygen reduction under conditions directly relevant to corrosion phenomena. To date, most of the significant work in this arena was aimed at studying the catalytic activity of Pt(*hkl*) to the oxygen reduction process using a rotating ring – disk electrode (RRDE) configuration under oxygen saturated conditions [1].

A significant motivation for the study that we report on herein is the key role of oxygen reduction in the corrosion of Aluminum Alloy 2024-T3. In this alloy, the corrosion rate is controlled by oxygen reduction on spatially separated microscopic intermetallic particulate phases that are highly enriched in copper owing to de-alloying [2-7]. On immersion in a corrosive environment these intermetallic particles (e.g., S-phase Al_2CuMg [2,4]) support oxygen reduction, presumably according to the reaction $2H_2O + O_2 + 4e^- = 4(OH)^-$, which results in a pH increase in the neighborhood of the local micro - cathodes. As the pH increases to about 9-9.5 [8-10], the passive oxide on the surface of the alloy matrix chemically dissolves causing the aluminum matrix to dissolve via the soluble AlO_2^- anion. We note that the corrosion potential of Al alloy 2024-T3 in a 0.5 M chloride or sulfate electrolyte is –800 mV to -600 mV (SCE) [11].

The general corrosion rate of the alloy and the subsequent extent of damage will depend on kinetics of the oxygen reduction at the copper enriched particles. In a recent study [2], we compared the kinetics of oxygen reduction on Al 2024 T3, a synthetic model Al 2024 T3 alloy, a planar Cu electrode and a lattice of copper particles embedded in an insulator (CEI samples) in 0.1 M Na_2SO_4. Both the synthetic alloy and the CEI sample contained 1.8 μm diameter Cu disks arranged in a square lattice with 9.5 μm near-neighbor spacing. This particle size and density was chosen to simulate the surface coverage of the S-phase on Al Alloy 2024-T3 [2]. We found that this configuration of Cu particles behaved as a microelectrode array for oxygen reduction. The oxygen diffusion - limited current density i_L on the CEI microelectrode array and on a pure planar copper electrode in a stagnant, naturally aerated electrolyte was 20-30 μA cm^{-2} [2]. These numbers differ significantly (by a factor of 4-5) from the numbers commonly accepted and used in the corrosion literature (i.e., 50 - 100 μA cm^{-2} [12]) and the immediate question is why? One possibility is that in a pH ~ 9 electrolyte in the near electrode vicinity, resulting from the ongoing oxygen reduction, a Cu surface may be oxidized so oxygen reduction may be under combined mass-transport and surface reaction – limited control.

In a truly stagnant electrolyte the diffusion boundary layer thickness (δ) tends to infinity and i_L would asymptotically approach a negligible value. However, in a real system i_L is never zero because of naturally occurring convection and a finite δ (albeit poorly defined) results.

Existing results for oxygen reduction on copper were obtained in oxygen saturated solutions [13,14]. They suggest a four-electron pathway for the process as well as an influence of the surface oxidation state on the reaction kinetics [13]. An influence on the reaction kinetics on pH as well as anion was also reported [14].

The study reported on herein is aimed at investigating the oxygen reduction reaction, taking place on a pure copper surface in naturally aerated 0.1 M Na_2SO_4 solution as a function of pH. Separate experiments performed on platinum under identical experimental conditions allowed for a comparison of the two metals as substrates for the oxygen reduction reaction. The Rotation Disk Electrode (RDE) technique was used in this investigation. Additionally, electrochemical scanning tunneling microscopy (ECSTM) experiments were used to characterize the morphological changes on a Cu (111) surface at potentials corresponding to the corrosion potential of Al 2024-T3.

2. Experimental Methods

2.1 Samples

A Cu (111) single crystal 2 mm thick and 10 mm in diameter was used in our ECSTM study. The crystal was electrochemically polished in 5:4:1 H_3PO_4 : water : ethyl alcohol solution prior to each ECSTM experiment. Anodic DC current (0.1 – 0.15 A cm^{-2}) was applied for 20 – 30 seconds. After the electrochemical polishing, the crystal was thoroughly rinsed with Barnstead Nanopure® (>18 MΩ) water and covered with a

droplet of pH 2 sulfuric acid in order to protect it from oxidation. Polycrystalline Cu and Pt disks with diameters 0.615 cm and areas of 0.3 cm^2 were cut from sheets and served as working electrodes in the RDE experiments. The disks were mechanically polished down to 3 μm on BUEHLER Carbimet® grinding paper that was lubricated with ethylene glycol. An alumina slurry (suspension of BUEHLER MICROPOLISH II Deagglomerated alumina polishing powder 0.05 μm in ethylene glycol), was used as the final mechanical polish. Following polishing the sample disks were rinsed with ethanol. The platinum disk was hydrogen flame-annealed for 5 minutes.

2.2 Rotating Disk Electrode Studies

RDE studies were performed on polycrystalline Cu samples in order to measure oxygen diffusion-limited current densities as a function of rotation rate and pH. The pH employed was 1.5, 3, 5.5, 7.5, 10, 12, and 14. Solutions with pH values of 1.5 and 3 were made using 0.1 M Na_2SO_4 acidified with H_2SO_4 while solutions with pH values of 7.5; 10; 12 and 14 were made using 0.1 M Na_2SO_4 adjusted with NaOH. RDE experiments were performed also on a Pt polycrystalline electrode in 0.1 M Na_2SO_4 (pH 5.5) and in 0.1 M Na_2SO_4 adjusted to pH 10. Each of the experiments designed to measure oxygen diffusion-limited current densities were at constant pH under a prescribed rotation rate by performing separately a cathodic as well as an anodic sweep at a sweep rate of 2 mV s^{-1}. The cathodic sweeps were performed starting from open circuit potential while the anodic sweeps had an initial potential just above the onset of hydrogen evolution. A saturated calomel electrode (SCE) was used as a reference electrode and a Pt sheet as a counter

6

electrode. All the potentials in the text are reported vs SCE unless stated otherwise. A standard RDE device (Pine Instruments) together with a Pine Instruments bi-potentiostat (model AFRDE5) were used and a Nicolet 310 Digital Oscilloscope served to store data.

2.4 ECSTM Experiments.

The ECSTM experiments were carried out using a Molecular Imaging Pico STM with a 300S scanner and a Molecular Imaging model 300S Pico Bipotentiostat. The cell was made out of Teflon and had a volume of *ca.* 1.5 cm^3 exposed an area of *ca.* 0.3 cm^2. The tunnelling tips were made of a polycrystalline Pt-20%Ir wire electrochemically etched in a solution of 1:3 saturated $CaCl_2$: water at about 21 V (AC). The tips were coated with Apiezon wax, leaving only the very end of the tip exposed to the electrolyte, in order to reduce the background current to numbers lower then 20 pA.

The working electrode in the ECSTM study was a Cu (111) single crystal. Platinum wires served as a reference and counter electrodes. They were cleaned with hot sulphuric and nitric acids and hydrogen flame annealed prior to the experiment. The reference electrode had a relatively stable potential of 50±20 mV. The electrolyte used was 0.1 M Na_2SO_4 adjusted to pH 10. In the ECSTM experiments, a potential of –1250 mV was applied immediately after introducing the solution to the cell, thus preventing the surface from spontaneous oxidation. There were two kinds of experiments. The first one was an examination of the Cu surface by increasing the potential in step-wise increments from –

1100 mV to –750 mV. In the second one we kept the potential at –800 mV and followed the morphology evolution with time.

All the solutions were made with high purity grade chemicals and Barnstead Nanopure® water. All glassware and Teflon ECSTM electrochemical cell used for experimentation and the preparation of electrolytes were cleaned with preheated (70°C) concentrated HNO_3 and H_2SO_4 and then rinsed using doubly distilled and Barnstead Nanopure® water.

3. Results and Discussion

STM Results

Figure 1 shows a set of STM images of a Cu (111) surface in 0.1 M Na_2SO_4 adjusted to pH 10 solution recorded while increasing the potential stepwise from –1100 mV to – 750 mV. The first two images (1a and 1b) represent a bare copper surface that consists mostly of monoatomic steps separating atomically flat terraces. No changes could be detected on the surface while increasing the potential from –1100 mV to –1000 mV. The first hint of a change was detected at a potential of –900 mV (image 1c). There was a slight increase in size of the topmost cluster in the middle portion of the image. More pronounced differences were found on image 1d where at a potential of –800 mV all terraces have grown out in a lateral direction. The formation of an underpotentially deposited (UPD) oxide layer was observed at a potential of –750 mV (image 1e) where

8

the entire surface was covered by high density oxide clusters the height of which correlates with the size of the Cu-O dimmer. A picture of the reduced Cu (111) surface obtained by switching the potential to −1300 mV is included at the end of this set of images. Similar results were obtained by Maurice et al. [15] on Cu (111) surfaces in 0.1 M NaOH at potentials of −950 mV to -900 mV. In their work the authors explain the lateral growth of the terraces as a result of "accumulation, at the step edges, of Cu atoms ejected from the adlayer superstructure due to reconstruction of the outermost Cu plane of the substrate". It was also suggested that "the same mechanism is responsible at the end of the adsorption process for the formation of Cu adislands on terraces when the adlayer grows in adsorbate-free areas surrounded by the superstructure". A more gradual forming oxide layer on Cu (111) is presented in Figure 2 where one sees a set of images obtained at a constant potential for 10 minutes. The oxide free surface (−800 mV, t = 0), image 2a, undergoes a change involving lateral terrace growth and oxide island formation within the first two minutes (image 2b). The oxide layer during the next eight minutes (images 2c-2e) covered a larger portion of the surface where most of the terrace regions are covered by the UPD oxide. The pit-like structure is interpreted by Maurice et al. [15] as a "mixed layer containing metal and oxide species". According to these authors the "pits" are not true topographic features. They argue that islands of adsorbate with lower apparent height are due to the lower conductivity of the oxide. Almost complete surface recovery was observed in the last image (2f) where a potential of − 1300 mV was applied to sample.

Summarizing the results of the ECSTM experiments it was concluded that an UPD

oxide layer covers the Cu (111) surface in the potential range of (-800 mV to –750 mV)

in a pH 10 electrolyte. This layer is stable at potentials positive to –800 mV and is

completely reduces at –1300 mV. Furthermore, the electrical conductivity of the Cu

surface covered with the UPD oxygen adlayer is high enough as to allow high quality

STM imaging.

RDE results

Figure 3 shows sets of anodic polarization curves obtained on Cu and Pt

polycrystalline electrodes in 0.1 M Na_2SO_4 (pH = 5.5, Figure 3a) and in 0.1 M Na_2SO_4

adjusted to pH 10 (Figure 3b) solutions. It is obvious that under these conditions the

electrochemical behavior of Cu and Pt as substrates for the oxygen reduction reaction is

identical and independent of pH. The diffusion-limited current densities measured on Cu

and Pt are plotted as function of the square root of the disk rotation rate (ω) in Figure 4.

The slopes in Figure 4 are 78.1 x 10^{-6} A $s^{1/2}rad^{-1/2}$ cm^{-2} for Cu and 77.7 x 10^{-6} A $s^{1/2}rad^{-1/2}$

cm^{-2} for Pt. The linear dependence of the current density on $\omega^{1/2}$ is indicative of diffusion

limited process that is described by the Levich equation, $i_L = 0.62nFD^{2/3}v^{-1/6}c_\infty\omega^{1/2}$.

Here i_L is the diffusion limited current density, n is the number of transferred electrons, F

is Faraday's constant, D the diffusion coefficient, v the kinematic viscosity, ω the disc

rotation rate and c_∞ the concentration of oxygen in the bulk solution. The experimentally

obtained slopes on Cu and Pt are very close to the theoretically calculated slope (83.3 x

10^{-6} A $s^{1/2}rad^{-1/2}$ cm^{-2}) for a four electron (n = 4) reduction process for $D = 1.93$ x 10^{-5} cm^2

s^{-1} [16], $v = 1.01 \times 10^{-2}$ $cm^2 s^{-1}$ [17], and $c_\infty = 2.25 \times 10^{-7}$ mole cm^{-3} [18] in naturally aerated solutions. Markovic et al. used a rotating ring-disk electrode configuration to study of oxygen reduction on Pt (*hkl*) [19] in oxygen saturated 0.05 M H_2SO_4. They demonstrated that oxygen reduction on Pt occurred via the 4-electron mechanism and obtained a Levich slope of 463×10^{-6} A $s^{1/2}rad^{-1/2}cm^{-2}$ which agrees well with the theoretically calculated value (466×10^{-6} A $s^{1/2}rad^{-1/2}cm^{-2}$) for $n = 4$. This slope is larger then the one obtained in the work presented herein by a factor of 5.9. This difference correlates with the difference in the concentration of oxygen in the electrolyte, 12.6×10^{-7} mole cm^{-3} [17] for the oxygen – saturated solution and 2.25×10^{-7} mole cm^{-3} [18] for the naturally aerated solution. Similar comparisons exist with results of Vasquez et al. [13] who investigated oxygen reduction on a pure copper electrode in oxygen - saturated borate solution. In that work the authors determined $n = 3.8$ for the electron pathway of the reaction. This result was obtained under the assumption that $D = 1.9 \times 10^{-5}$ cm^2 s^{-1}, $v = 1 \times 10^{-2}$ $cm^2 s^{-1}$, and c_∞ is 12.6×10^{-7} mole cm^{-3}. We have estimated the slope of the Levich plots presented in [13] to be 440×10^{-6} A $s^{1/2}rad^{-1/2}cm^{-2}$. This slope is close to that obtained by Markovic et al. [19] on Pt in 0.05 M H_2SO_4 and differs from the one we obtained in the present study by a factor of 5.6. These results taken together lead us to conclude that a four-electron oxygen reduction mechanism takes place on copper in naturally aerated 0.1 M Na_2SO_4 solution. Interestingly enough, we found no evidence of an influence of either oxygen concentration or the existence of the UPD oxygen adlayer on the reduction mechanism or the magnitude of the diffusion limited current density.

Figure 5 shows four sets of polarization curves obtained in 0.1 M Na_2SO_4 solutions at different pH levels (3; 5.5; 7.5; 12). Each set contains polarization curves registered at prescribed disk rotation rate. The curves represented in each of the sets with solid lines were obtained while sweeping the potential from open circuit in cathodic direction. The dotted line curves were initiated at the onset of hydrogen evolution and the potential was swept in an anodic direction. When the experiment is performed in alkaline solution, there exists a wave within the potential range -600 mV to –400 mV. As seen in Figure 5, this wave does not exist in acidified or neutral solutions. According to the Pourbaix diagram [20], this wave can be attributed to the oxidation of Cu to Cu(I). The major difference in the anodic and cathodic sweeps is due to the initial chemical nature of the copper surface. In an anodic sweep the initial Cu surface is film-free regardless of the solution pH. In the cathodic sweep case at pH > 6 [20] the initial copper surface (i.e., at open circuit) is covered with a bulk oxide (Cu_2O). Comparison of the curves at different pH levels shows almost identical plateau-levels on the anodic and cathodic curves at pH 3 and pH 5.5. The plateau-levels are different at pH 7.5 and pH 12 in that the cathodic curves systematically exceed the anodic ones. The difference in i_L (the plateau-levels) is summarized in Figure 6 where all the limiting currents are plotted as a function of pH and sweep direction. There is no difference in i_L in the anodic and cathodic sweeps in acidified and neutral solutions (pH 1.5 to 5.5). In alkaline solution the current densities measured by a cathodic sweep exceed the ones obtained by anodic sweep by 50 to 150 $\mu A\ cm^{-2}$. This result is most likely due to a contribution of bulk oxide reduction to i_L. According to [15], the reduction of Cu_2O in 0.1 M NaOH takes place between –600 mV and –1000 mV; i.e., within the range of our measurement of i_L. Since bulk oxide

reduction is not under diffusion control its contribution is independent or only slightly dependent on the disk rotation rate. No influence of the UPD oxygen adlayer on the oxygen reduction reaction could be detected in any of our results.

Figure 7 shows Levich plots for i_L as a function of rotation rate and pH. Figure 8 summarizes the results for the slopes of the Levich plots shown in Figure 7. The average slopes of the lines obtained from the cathodic and anodic polarization curves are 83 ± 7 x 10^{-6} A-s$^{1/2}$rad$^{-1/2}$cm^{-2} and 79 ± 3 x 10^{-6} A-s$^{1/2}$rad$^{-1/2}$cm^{-2} respectively. This result is consistent with the theoretically predicted Levitch slope of 83.3 x 10^{-6} A-s$^{1/2}$rad$^{-1/2}$cm^{-2} for a four-electron reaction (n = 4) in naturally aerated solution. The results are entirely consistent with those obtained by Markovic et al. on Pt [19] and therefore indicate the operation of a four-electron mechanism for oxygen reduction on Cu over the entire pH range examined.

4. Summary and Conclusions

The reduction of oxygen on a polycrystalline copper electrode was investigated in 0.1 M Na_2SO_4 solutions at different pH levels. RDE and ECSTM techniques were used to examine the Cu surface morphology and the kinetics of the process.

The ECSTM study showed a formation of a UPD oxygen adlayer on Cu(111) at potentials far more negative (–800 mV) then the potential of Cu(I) oxidation in a pH 10 electrolyte. In agreement with the results of Maurice et al. [15] obtained in a pH 13

13

electrolyte, the evolution of that layer at a fixed potential was found to depend on the electrochemical potential and time. No influence of the adlayer on the oxygen reduction reaction kinetics was detected over the entire pH range examined. This indicates that the conductivity of this layer was high enough as to not impede the mass-transport limited rate of oxygen reduction.

Results of RDE experiments show that a four - electron mechanism for oxygen reduction on Cu is operative over the entire pH range investigated. The initial stage of the surface (film - free Cu or bulk Cu_2O) was found to slightly affect the diffusion-limited current densities measured at pH > 6.

It is probably worth mentioning that we performed a similar set of experiments measuring i_L in a thin – fluid layer cell under stagnant conditions and obtain the same value as those quoted above. These thin – layer cell experiments essentially maximize the electrolyte/vapor interfacial area with respect to the cell volume. All of the results taken together lead to the conclusion that the diffusion limited current density for oxygen reduction via a four – electron mechanism in a stagnant electrolyte is 20 – 30 μAcm^{-2}.

Acknowledgments

References

1. R. Adzic, *Electrocatalysis*, pp. 197-243, Eds. J.Lipkowski and P.N.Ross, WILEY-VCH, (1998)

2. M. B.Vukmirovic, N. Dimitrov, and K. Sieradzki, Submitted for publication in *J. Electrochem. Soc.*

3. R.G.Buchheit,   R.P.Grant,   P.F.Hlava,   B.Mckenzie   and   G.L.Zender, *J.Electrochem.Soc.*, **144**, 2621 (1997)

4. A.J.Aldykewicz, H.S.Isaacs and A.J.Davenport, *J.Electrochem.Soc.*, **142**, 3342 (1995)

5. G.S.Chen, M.Gao and R.P.Wei, *Corrosion*, **52**, 8 (1996)

6. T.J.Warner, M.P.Schmidt, F.Sommer and D.Bellot, *Z.Metallkd.*, **86**, 494 (1995)

7. G.L.Sheider,   N.N.Cherkasov,   V.I.Smolentsev,   B.E.Popov   and   A.P.Kovtun, *Mater.Sci.Heat Treat.*, **26**, 632 (1985)

8. M.A.Alodan and W.H.Smyrl, *J.Electrochem.Soc.*, **145**, 1571 (1998)

9. MURI Report to the AFSOR, ASU, August 1998

10. J. O. Park, C. H. Paik, Y. H. Huang, and R. C. Alkire, *J.Electrochem.Soc.*, **146**, 517 (1999)

11. M.B.Vukmirovic, PhD Dissertation, Arizona State University, 2001, in preparation

12. Corrosion engineering, M.G.Fontana and N.D.Greene, Publisher New York, McGraw-Hill [1967], p. 315

13. M. V. Vazquez, S. R. de Sanchez, E. J. Calvo, and D. J. Schiffrin, *J. Electroanal. Chem.*, **374**, 189 (1994)

14. K. Balakrishnan and V. K. Venkatesan, *Electrochim. Acta*, **24**, 131 (1979)

15. V. Maurice , H.-H. Strehblow , P. Marcus , *Surface Science*, **458**, 185 (2000); J. Kunze, V. Maurice, L. H. Klein, H.-H. Strehblow, and P. Marcus, *J. Phys. Chem. B*, **105**, 4263 (2001)

16. N. A. Anastasijevic, Z. M. Dimitrijevic, and R. R. Adzic, *Electrochim. Acta*, **31**, 1125 (1986)

17. CRC Handbook of Chemistry and Physics, 66th ed.; R. C. Weast Ed; CRC Press: Boca Raton, Florida, 1986

18. C.G. MacARTHUR, *J. Phys. Chem.*, **20**, 495 (1916)

19. N. M. Markovic, H. A. Gasteiger, and P. N. Ross, Jr., *J. Phys. Chem*, **99**, 3411 (1995)

20. Atlas of Electrochemical Equilibria in Aqueous Solutions, Marcel Pourbaix, NACE 1974

Figure Captions:

Figure 1. STM micrograph showing morphological changes on Cu (111) in 0.1 M Na$_2$SO$_4$ adjusted to pH 10 solution as a function of increasing potential; (a) -1100 mV, (b) -1000 mV, (c) -900 mV, (d) -800 mV, (e) -750 mV, (f) -1300 mV

Figure 2. STM micrograph showing morphological changes on Cu (111) at a constant potential of –800 mV in 0.1 M Na$_2$SO$_4$ adjusted to pH 10 solution as a function of time. (a) 0 minute, (b) 2 minute, (c) 5 minute, (d) 8 minute, (e) 10minute and (f) –1300 mV.

Figure 3. Anodic polarization curves obtained in: (A) and (B) 0.1 M Na$_2$SO$_4$ adjusted to pH 10 on Cu (solid lines) and Pt (dashed lines) polycrystalline disks at pre-described disk rotation rates.

Figure 4. Levich plots for oxygen diffusion-limited current densities measured in 0.1 M Na$_2$SO$_4$ and 0.1 M Na$_2$SO$_4$ adjusted to pH 10 on Cu and Pt polycrystalline disks at pre-described disk rotation rates.

Figure 5. Anodic (dashed lines) and cathodic (solid lines) polarization curves obtained in 0.1 M Na$_2$SO$_4$ as a function of pH (A, pH = 3; B, pH = 5.5; C, pH = 7.5; D, pH = 12) on copper polycrystalline disks at pre-described disk rotation rates.

Figure 6. Oxygen diffusion-limited current densities (anodic – dashed lines and cathodic – solid lines) measured in 0.1 M Na_2SO_4 as a function of pH on copper polycrystalline disks at pre-described disk rotation rates.

Figure 7. Levich plots for oxygen diffusion-limited current densities measured in 0.1 M Na_2SO_4 as a function of pH on copper polycrystalline disks at pre-described disk rotation rates; A, i_L measured during an anodic sweep; B, i_L measured during a cathodic sweep.

Figure 8. Summary of slopes of the Levich plots presented in Figure 7as a function of pH.

a

b

c

d

e

f
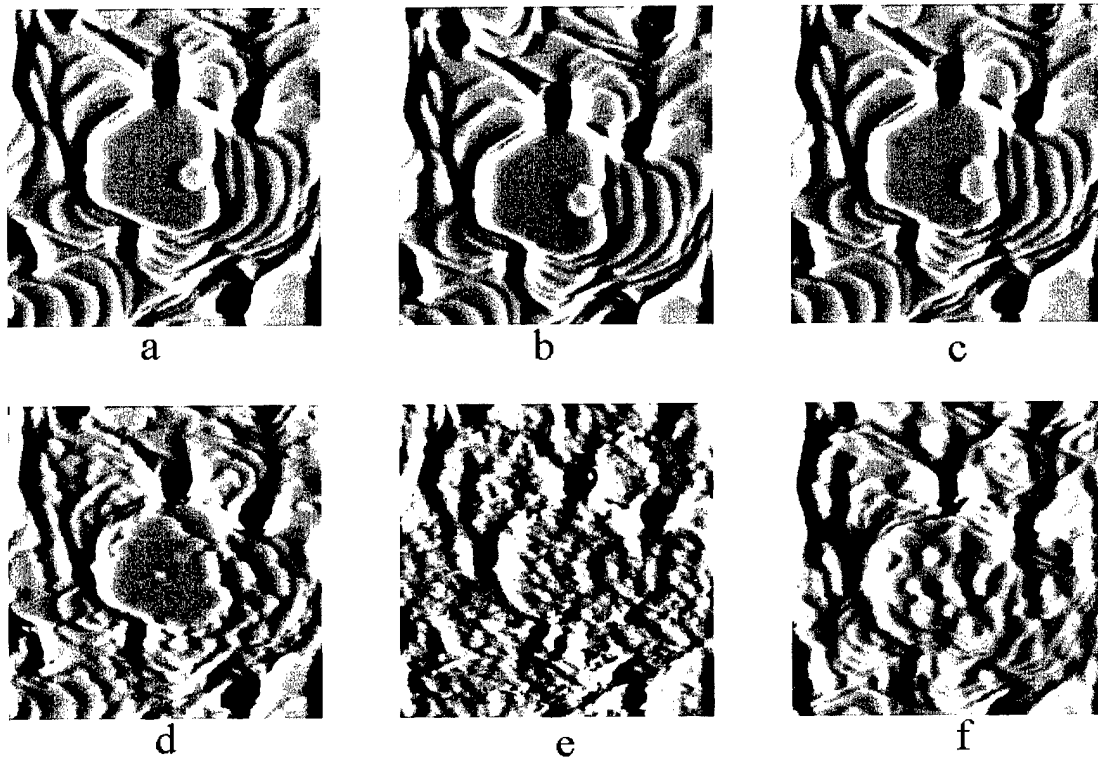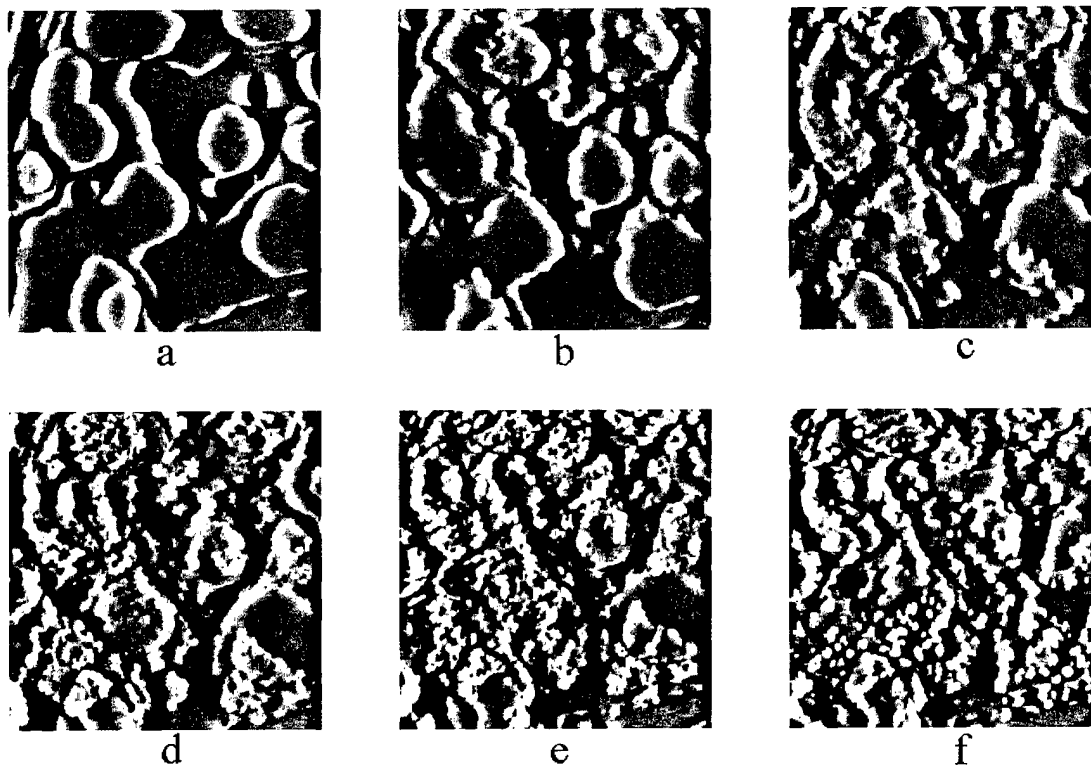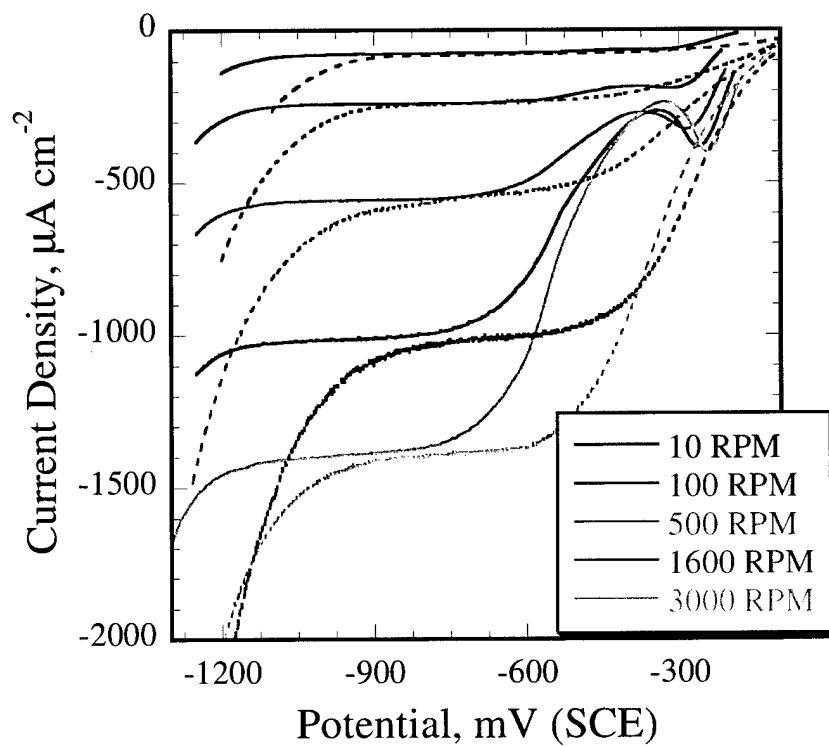
Figure 1

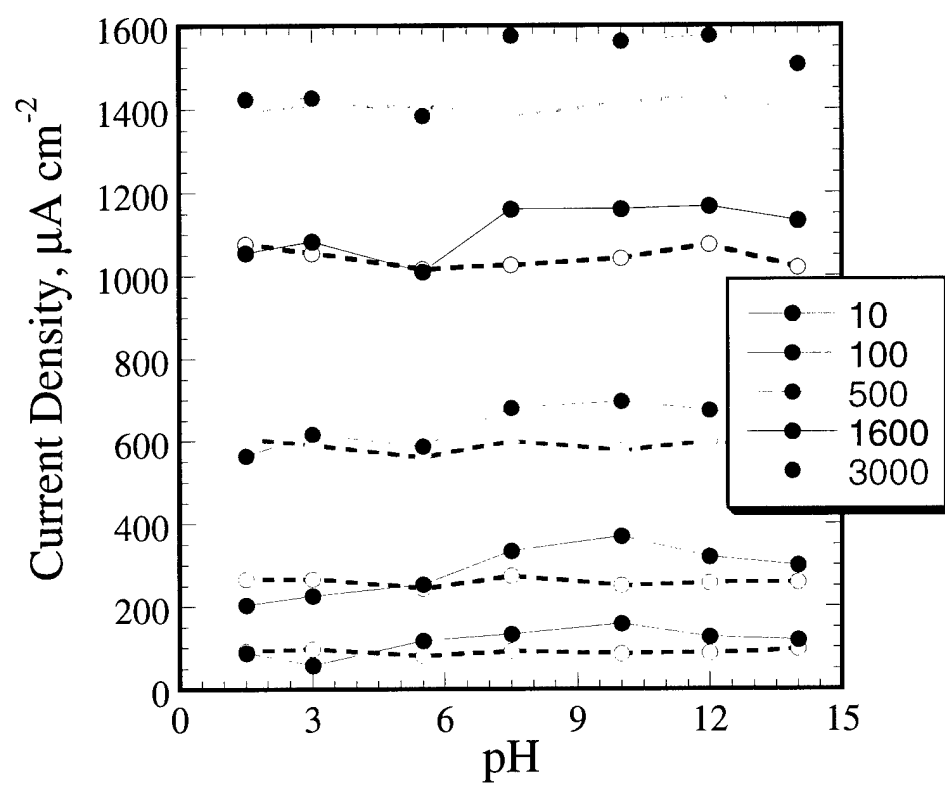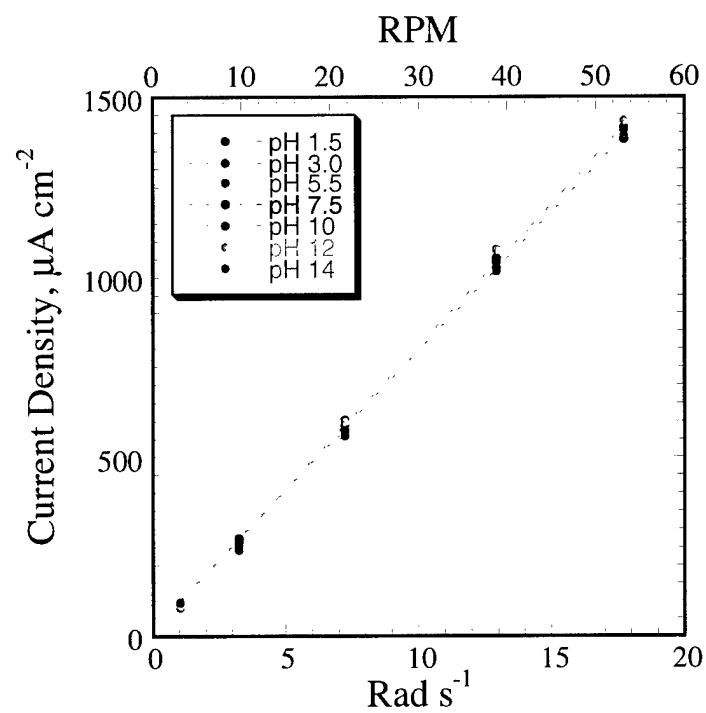Figure 2

Figure 3a
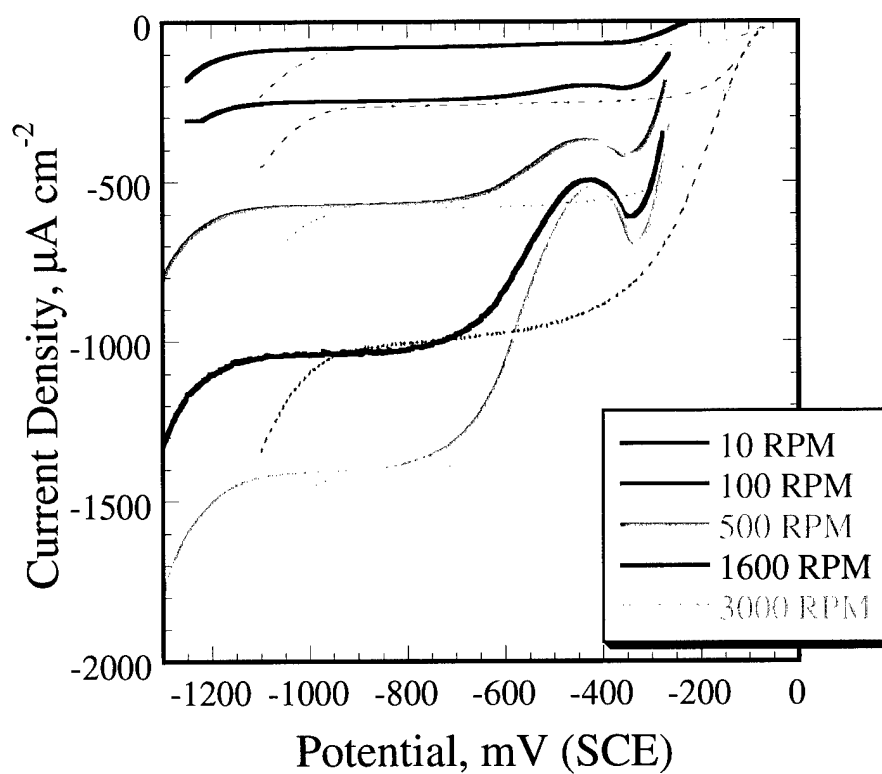
Figure 3b
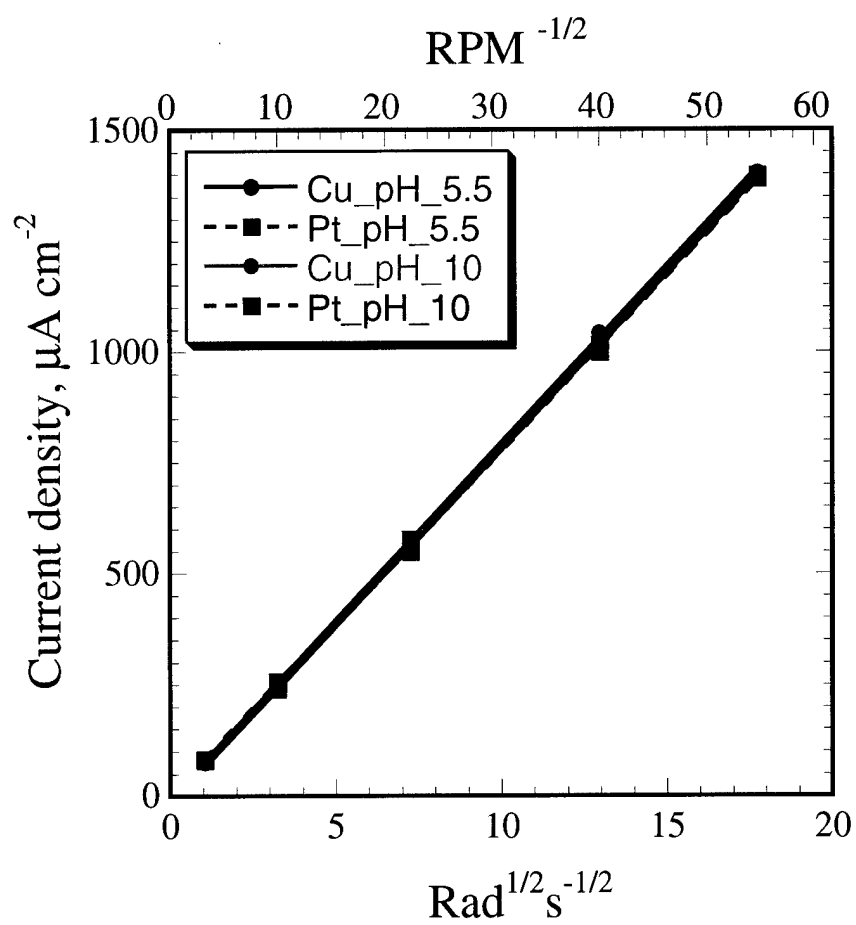
Figure 4
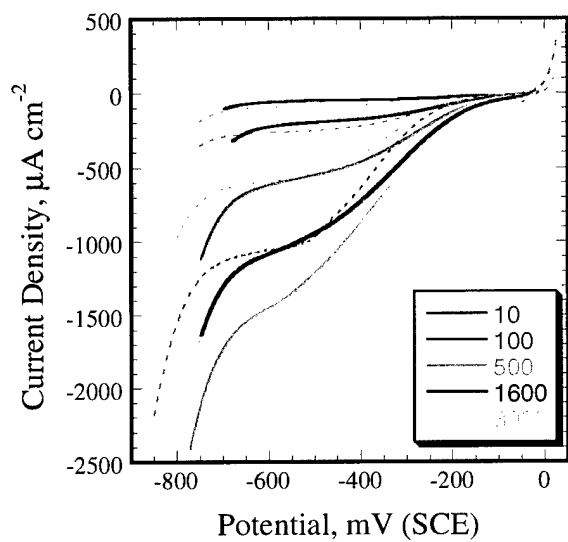
Figure 5a
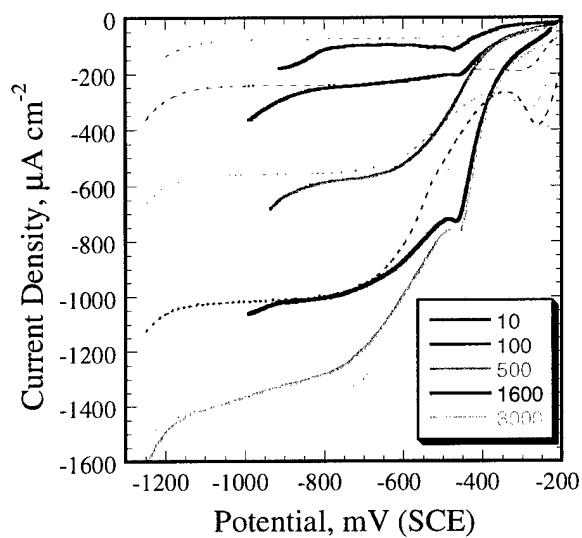
Figure 5b
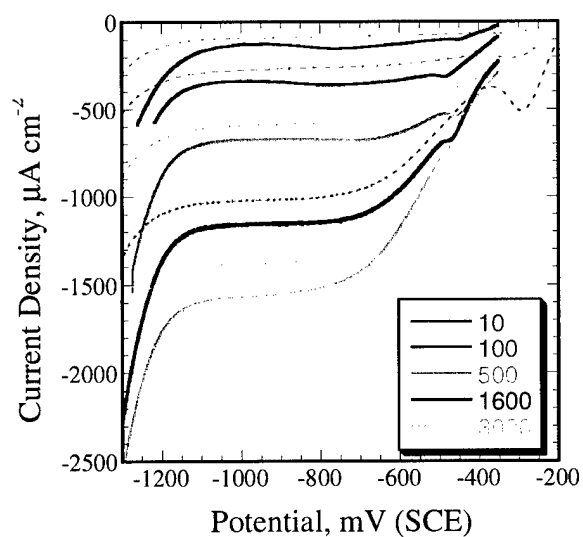
Figure 5c
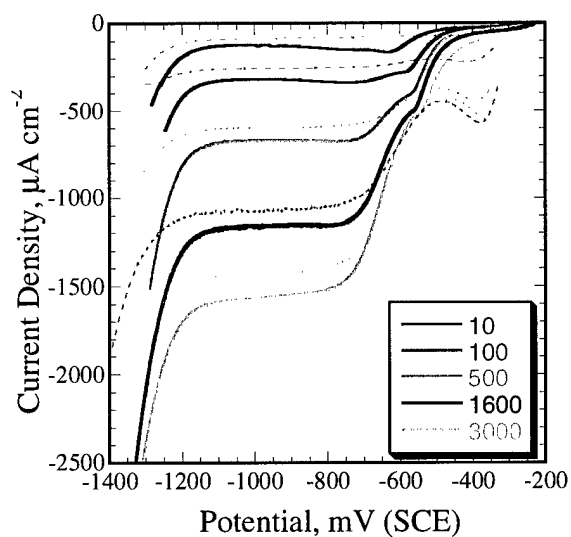
Figure 5d

Figure 6

Figure 7a

Figure 7b

Figure 8